ELECTROSTATIC FORCE MICROSCOPY STUDIES OF NANOSCALE SYSTEMS

A Thesis

Submitted to the Faculty

of

Purdue University

by

Stephen Wayne Howell

In Partial Fulfillment of the

Requirements for the Degree

of

Doctor of Philosophy

May 2001

This thesis is dedicated to my beloved wife Laura and to my parents.

ACKNOWLEDGMENTS

I would like to thank Professor Ronald Reifenberger for supporting my graduate research. In particular, I would like to thank him for all the many energetic discussions and insightful suggestions that helped to bring clarity to this work.

A special thanks also goes to Professor David Janes. His vast knowledge of semiconductor physics and technology greatly influenced the direction of my research.

I would also like to thank Professor Supriyo Datta, Titash Rakshit and Avik Ghosh. Their helpful comments and insight have made considerable advancements in the understanding of electrostatic potential produced by molecules adsorbed onto metal surfaces.

I cannot over look my colleagues: Dr. Debasish Kuila, Dr. Takhee Lee, Dr. Elton Graugnard and Scott Crittenden. They provided a great deal of assistance through numerous useful discussions.

I would also like to thank Dr. Donald Rimai at Nexpress for his helpful discussions and his interest in this work.

Finally, I would like to thank my family for their support during this academic endeavor. In particular, I would like to thank my wonderful wife Laura. I will always be indebted to her for the emotional support that she has given me over the past several years.

This work was partially funded by NexPress and in part by MURI Grant No. DAAD19-99-1-0198 from the Army Research Office and the National Science Foundation under contract 9708107-DMR.

TABLE OF CONTENTS

Page

Page

LIST OF TABLES

LIST OF FIGURES

Figure Page

Figure Page

Figure Page

Figure Page

Figure Page

Figure Page

ABSTRACT

Howell, Stephen W., Ph.D., Purdue University, May, 2001. Electrostatic Force Microscopy Studies of Nanoscale Systems. Major Professor: Ronald G. Reifenberger.

Electrostatic force microscopy has been used to study the electrostatic force on a nanometer length scale. The experimental techniques, implemented to measure electrostatic force, were based on established methods reported in the literature. These measurements were acquired using an electrostatic force microscope (EFM). The EFM consisted of a commercially available atomic force microscope (AFM) that was modified to measure the electrostatic interaction between an AFM tip and a sample substrate. In addition to modifying the commercial AFM, a homebuilt AFM/EFM was constructed at Purdue capable of making electrostatic measurements in an ultra high vacuum environment.

After performing several experiments designed to test both the operation and the sensitivity of the EFM, extensive studies of several nanoscale systems were conducted. In particular, the EFM was used to measure the electrostatic potentials of a single nanometer-sized gold cluster and self-assembled arrays of encapsulated gold clusters. The surface potential of the array was found to be at a higher positive potential than the underlying gold substrate, indicating that the encapsulated clusters have a lower work function than bulk gold.

In addition, the EFM was used to measure surface potential as a function of time for various LTG:GaAs substrates after the removal of the oxide layer. The behavior of the surface potential with respect to time was found to be dependent on the agent used for the oxide removal.

Finally, the EFM was used to measure the surface potential of self-assembled monolayers chemisorb onto Au(111). The monolayers' surface potentials were found to depend on the molecular structure of the molecules forming the monolayer.

1. INTRODUCTION

For the last several decades, miniaturization of electronic devices has made a major impact on modern life. With the discovery of the silicon base transistor in 1948, the doorway has been opened for the development of micrometer scale devices, making it possible to produce highly complex computational systems that require a fraction of the space needed by devices produced from older vacuum-tube technology. This concept of miniaturization has revolutionized many facets of our society, from the space program to medical technology.

However, the current technology used to produce submicrometer-sized devices is rapidly approaching its limits. Using machinery that has been based on current fabrication technology to construct devices below 0.1 microns has proven to be uneconomical.

If the drive to miniaturize electronic devices is to continue past the submicron length scale, new technology must be developed which is both economical and practical. This technology should be based on structures that have nanometer dimensions such as nanoclusters, molecules, and nanowires (carbon nanotubes). Such tiny systems might become the building blocks for a new class of electronic devices.

In recent years, major discoveries in mechanisms controlling nanoscale structures have shown that nanoelectronics can be a practical reality. The discovery of self-assembly of molecules on metal and semiconducting surfaces [1–4] provided new possibilities for practical solutions in the construction of nanoscale devices. Using self-assembly (chemical) processes to make nanoscale devices eliminates the need for complex machinery required to manipulate objects with nanometer resolution. Additional research has also shown there are possible uses of nanowires as inter-connects for interfacing nanoscale devices to the microelectronic systems.

However, even with these recent discoveries, nanotechnology is still very much in its infant stages. A more in-depth understanding of nanosystems is still required to proceed with the development of working devices. As development continues in the field of nanotechnology, a need has arisen for the characterization of these nanoscale systems. Not only is electronic characterization necessary, but knowledge of the interaction forces acting on these systems is also necessary.

One of the most important forces controlling the electronic properties of the nanostructures is the electrostatic interaction. Knowledge of electrostatic interaction present in a nanosystem can provide a powerful insight into the mechanisms controlling the electronic properties. [5] For example, in the case of molecular self-assembly, measuring the electrostatic potential of the monolayer can provide important information on the properties of a molecule's charge distribution. Interpreting the distribution of the charge is useful for understanding the mechanism behind molecular conduction and the molecule's adsorption on a surface.

Since molecules and other nanoscale systems have dimensions on the order of nanometers, a high lateral resolution is required for probing the electrostatic field near these objects. An instrument capable of probing such structures is known as atomic force microscope (AFM). Since the invention of Atomic Force Microscope in the late 1980's, the AFM has proven to be an extremely versatile tool for probing forces near a surface with incredible resolution. [6] This instrument is capable of measuring piconewton forces with nanometer lateral resolution. Using a multiple of techniques, the nature of different forces near the sample's surface can be determined.

The AFM measures forces by detecting the motion of a spring-like probe known as a cantilever. Cantilevers are long thin micro-machined beams of silicon with a base containing a tiny tip attached at its end. The tips are micro-machined to have an end radius of $\approx$ 10 nm. The high lateral resolution of force measurements is due to the small diameter of the tip's apex. Force interactions between the tip and sample cause the cantilever beam to deflect. By monitoring the deflection of the cantilever during an experiment, it is possible to measure a multitude of different forces(magnetic, van der Waals, electrostatic, adhesion) simultaneously. [7–9]

To measure the electrostatic interaction, a conducting tip is biased with a controlled voltage. The applied bias modifies the tip-sample potential difference, which produces a deflection of the cantilever. By controlling the tip-sample potential difference, the electrostatic force emanating from a sample's surface can be measured as a function of position. Utilizing the high-resolution capabilities of the AFM, maps of the electrostatic force with lateral resolution of ≈ 50 nm can be generated, providing a measure of the electrostatic surface potential of the sample under investigation.

The following chapters will discuss the fundamental principles for measuring the electrostatic force using an electrostatic force microscope (EFM). The EFM is simply a modified AFM, where the electrostatic interaction is controlled by an applied bias voltage. The initial discussions will focus on the techniques and instrumentation used for measuring the electrostatic interactions. After the initial review, the results of several experiments will be presented. These initial experiments built confidence and exposed problems with the experimental techniques used for this work. Finally, the results of several EFM studies that measured surface potentials produced by nanostructures will be presented. These studies demonstrate the utility of EFM in characterizing nanoscale systems.

2. THEORY OF ELECTROSTATIC FORCE MICROSCOPY

The Electrostatic Force Microscope (EFM) is a modified AFM, where the cantilever is connected to an independently controlled bias voltage. This bias voltage is used to eliminate the electrostatic field that exists between the tip and sample. The EFM can measure the morphology of the surface while simultaneously measuring the electrostatic force as a function of position (dual probe). The benefit of using a nanoscale proximal probe is the ability to measure both topographic and electrostatic information with nanometer lateral resolution. The high-resolution capability makes the EFM a powerful tool for characterizing nanosystems.

The next several sections will discuss concepts such as origin of the surface contact potential difference, operation of a macroscopic Kelvin Probe and operating theory of an EFM. These discussions are important for understanding Electrostatic Force Microscopy. Actual experimental methods for measuring the electrostatic interaction will be discussed in later chapters.

2.1 Origin of the Contact Potential Difference

The total electrostatic field near the surface of a sample originates from a combination of many different effects. One of the most significant contributions is from the contact potential difference (CPD). A CPD exists when crystalline objects are placed in intimate contact to form a junction. This potential difference results from the equilibrium of both the temperature and the chemical potential throughout the junction. [10]

Free electrons inside a solid will reside in a periodic potential energy distribution due to the crystalline ordering of the atoms. In a periodic potential, electrons can only exist in allowed energy states. [11] The highest occupied electron energy state

of the crystalline solid is known as the Fermi level E_F (in units of eV) and is often referred to as the chemical potential.

Defects near the surface of a neutral crystalline structure, such as metal or a semiconductor, will produce localized areas of net charge. [12] The net charge produces an electric potential V_{Vac} (in units of volts) just outside of the solid's surface. Therefore, the electron must acquire a certain amount of energy in order to escape the metal. The energy required to bring the electron from its highest occupied energy state (the Fermi level) to a position just outside of the metal's surface is the difference between the Fermi energy and electrostatic potential energy E_{Vac} (where $E_{Vac} = -eV_{Vac}$). This amount of energy is defined as the work function of the metal ϕ (in units of eV).

When crystalline solids are connected together by a path that allows the transfer of electrons, the electrons will reach thermal and diffusive equilibrium. Therefore, the temperature and Fermi level (chemical potential) of the solids will be uniform throughout the junction. [10] The Fermi levels are aligned by a transfer of charge from one object to the other. This net charge creates an electrostatic field between the surfaces of the junction. The potential difference that now exists across the junction is referred to as the CPD. Since the magnitude of the work function is constant and independent of the position of the Fermi level, the CPD can be described as a difference between the work functions of the two solids.

To better illustrate this point, consider the case of two different metal electrodes with different work functions (ϕ) and Fermi levels (E_F). The initial energy levels of the electrodes prior to the formation of the junction are (Fig. 2.1 a)

$$\phi_1 = E_{Vac1} - E_{F1} \tag{2.1}$$

and

$$\phi_2 = E_{Vac2} - E_{F2} \quad . \tag{2.2}$$

A contact potential difference (CPD) results when the two metals are connected together in such a way that allows the electrons in the metals to reach thermal equilibrium (Fig. 2.1 b). [11] To bring the electrons into equilibrium, some charge will

flow from one electrode into the other. As a result, each electrode has a net surface charge. This charge causes the Fermi levels in each metal to shift until they coincide:

$$E_{F1} = E_{F2} \quad . \tag{2.3}$$

This net transferred charge resides on the surface of the electrodes and creates an electrostatic potential difference $\triangle V_{CPD}$ between the electrodes.

If an electron is removed from the Fermi level of one electrode (with ϕ_1) and placed into the other electrode (with ϕ_2) at the same Fermi level, the work done W (in units of eV) is

$$W = \phi_1 - \phi_2 \quad . \tag{2.4}$$

But for the system to conserve energy, the work done by moving the electron across the potential difference ($-e \triangle V_{CPD}$) must equal the difference between the work functions:

$$-e \triangle V_{CPD} = -e(V_1 - V_2) = E_{Vac1} - E_{Vac2} = \phi_1 - \phi_2 \quad . \tag{2.5}$$

Equation 2.5 relates the V_{CPD} to the difference between the vacuum energies of the two electrodes, which are also determined by the differences of the electrodes' work functions. By measuring the CPD, it is possible to determine the difference in the work functions of the electrodes.

In addition to the electric field produced by thermodynamic equilibrium, regions of trapped charge could also exist on the surface of the electrodes. The trapped charge will create its own electrostatic fields. The overall net field between the electrodes would be a superposition of the electric fields produced by the different charge densities. However, the trapped charge can be treated as a modification of the electrode's work functions (ϕ_1'), allowing the CPD to be expressed as a difference in work functions.

A device used to measure the CPD is referred to as a Kelvin probe. [13] The Kelvin probe technique is based on measuring the potential difference between a sample with an unknown work function and a reference electrode that has a known work function.

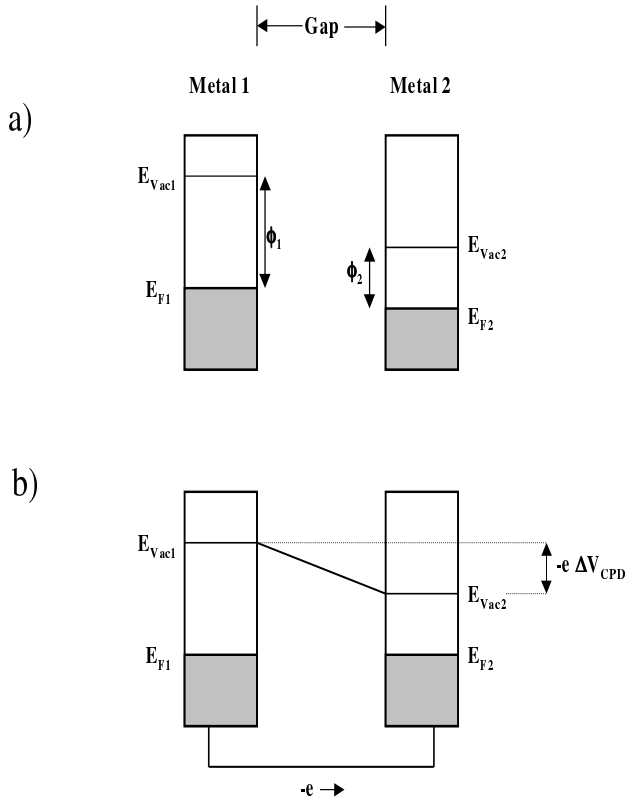

Figure 2.1. a) Energy band diagram of two metal electrodes before an electrical connection is established between them. b) When the metal electrodes are connected together, some charge will flow. This charge aligns the electrodes' Fermi levels. The net transferred charge produces a potential difference $\triangle V_{CPD}$ between the electrodes.

For the case of electrostatic force microscopy, the electric field that exists near the surface results from differences between the work functions of the tip and sample. The next several sections will discuss in more detail the process of measuring the CPD.

2.2 Operational Principles of a Macroscopic Kelvin Probe

A macroscopic Kelvin probe is a device that is used to measure the CPD that exists between a sample and reference electrode. Over the past hundred years, the Kelvin probe has proven to be a very valuable tool for probing the work functions of

metals and semiconductors. [14–17] Understanding the operation of a Kelvin probe provides significant insight into the operation of an electrostatic force microscope.

Figure 2.2 displays the typical experimental configuration of a Kelvin probe. The Kelvin probe consists of two electrodes composed of different metals arranged to form a macroscopic parallel plate capacitor system, where the electrodes' diameters are much larger than their separation. The electrodes are connected in series with a current meter and a voltage source.

When an electrical connection is established, the electrodes will reach thermal and chemical potential equilibrium (Eq. 2.3). At equilibrium, a contact potential difference ($\triangle V_{CPD}$) exists across the electrodes (Fig. 2.3 a). A current can be made to flow through the electrical connection by periodically modifying the separation of the electrodes (periodically changing the capacitance). The current due to the changing capacitance is given by [11]

$$i = \frac{\delta Q}{\delta t} = \frac{\delta}{\delta t}(C \triangle V_{CPD}) = \frac{\delta C}{\delta t} \triangle V_{CPD} \quad , \tag{2.6}$$

where $\triangle V_{CPD}$ is fixed and C the capacitance is

$$C = \frac{\epsilon_o A}{d} \quad . \tag{2.7}$$

The capacitance is periodically modified by connecting one electrode to a piezoelectric vibrator (Fig. 2.2). By vibrating the probe electrode at a frequency ω and an amplitude A_0, the electrode separation becomes

$$d = d_0 + A_0 \cos \omega t \quad . \tag{2.8}$$

The periodic variation of the electrodes' separation produces a current that is detected with a synchronous current meter referenced to the driving frequency ω and connected in series with the electrodes. [18]

For this arrangement, any modifications to the potential difference between the electrodes alters the current flowing through the circuit (Eq. 2.6). For the situation where the potential difference is zero, the current would cease to flow. Thus, the

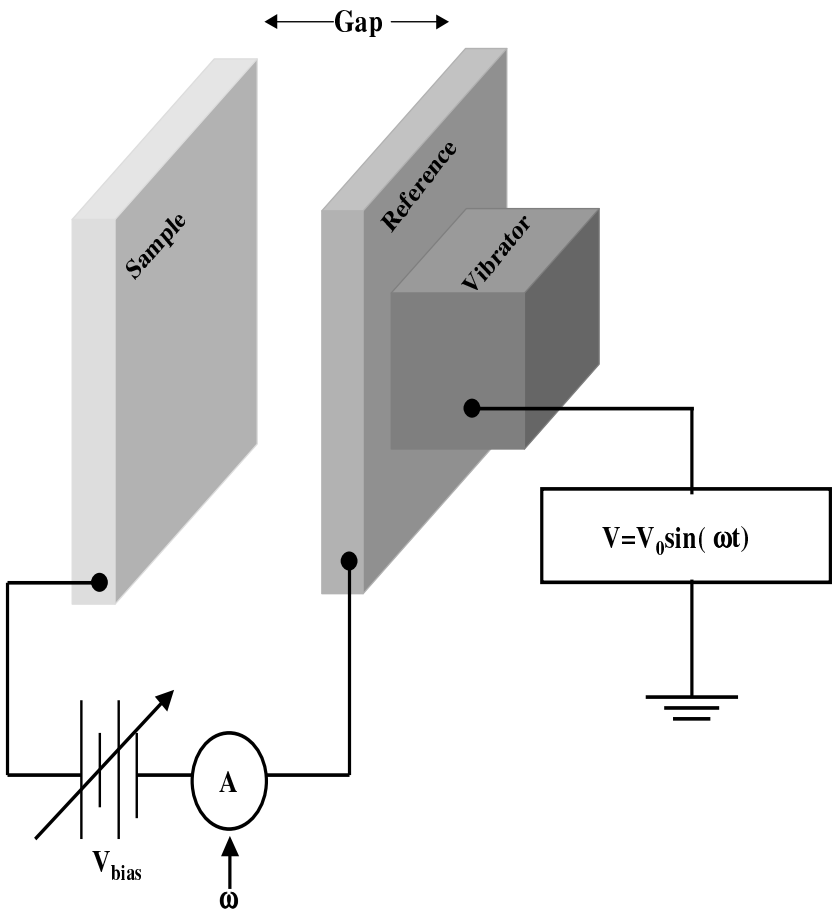

Figure 2.2. Experimental configuration of a macroscopic Kelvin probe. The sample and reference electrodes are connected together in series with a DC bias voltage and a synchronous current meter. The separation of the electrodes is periodically modulated by a piezo-vibrator. The modification of the electrode spacing produces a periodic current (since the capacitance of the system is changing), which is detected by the synchronous current meter.

dependence of the current on the potential difference between the plates can be used to determine the CPD.

The potential difference is modified by a variable voltage source placed in series with the electrodes. The potential drop across the electrodes becomes

$$\triangle V = \triangle V_{CPD} + V_{bias} \quad . \tag{2.9}$$

The bias voltage modifies the Fermi level in the reference electrode by adding or removing electrons. Since the work function is constant, the applied bias voltage also shifts the vacuum energy level. By applying the appropriate bias voltage, it is possible to shift the vacuum energy of the reference electrode until it coincides with the vacuum energy of the sample electrode (Fig. 2.3 b). This is referred to as the "flat band condition".

At the "flat band condition", the synchronous current will be eliminated, since the potential difference between electrodes was also eliminated. At this point, the contact potential is equal and opposite of the bias voltage:

$$\triangle V_{CPD} = -V_{bias} \quad when \quad \frac{dQ}{dt} = 0 \quad . \tag{2.10}$$

By knowing the work function of the probe electrode, one can infer the work function of the sample by measuring the contact potential difference using Eq. 2.5. [11]

Most macroscopic Kelvin probes use electrodes with the dimensions on the order of millimeters. Since these electrodes are large, small variations in the contact potential on the surface are averaged over the entire electrode. To increase the lateral resolution, the probing electrode must be made smaller. For this application, a conducting AFM tip with a radius of $\approx$ 10 nanometers will provide high lateral resolution for detecting contact potential variations.

2.3 Operational Principles of an Electrostatic Force Microscope

Electrostatic force microscopes have been used in recent years to answer fundament questions about the electrostatic interaction on the nanometer scale. Using a similar methodology of the macroscopic Kelvin probe, the EFM eliminates the potential difference that exists between a sample and a conducting AFM tip using an

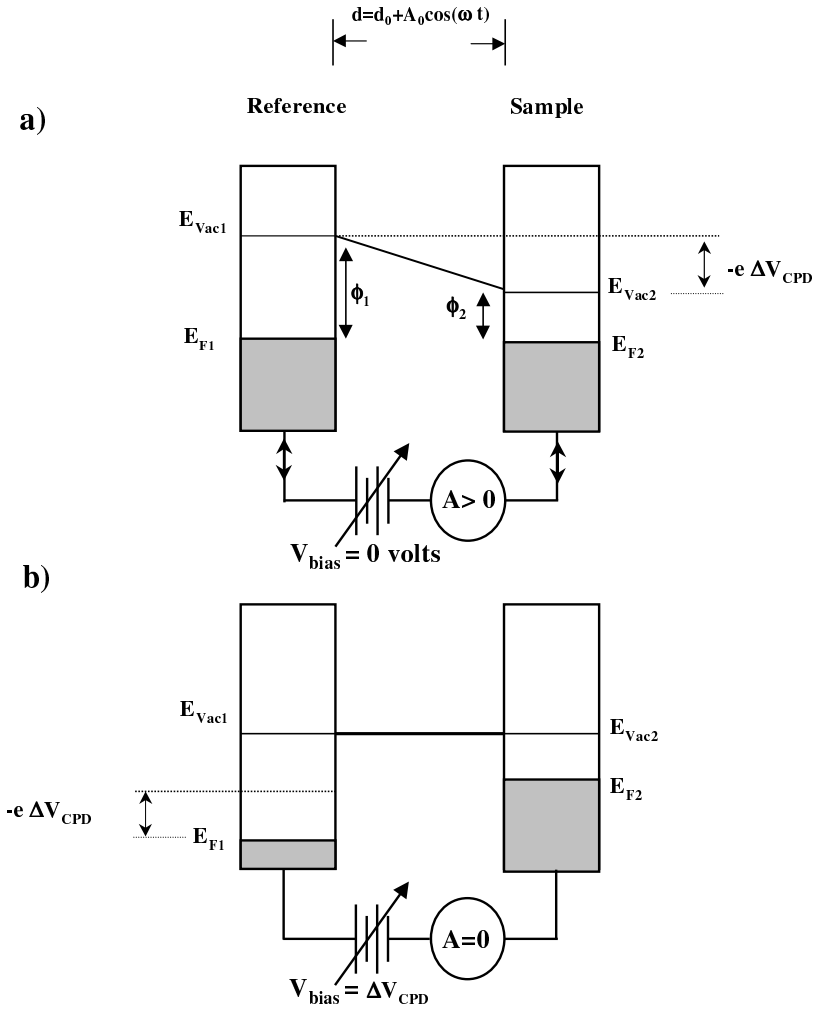

Figure 2.3. a) Initial energy configuration of macroscopic system (V_{Bias}=0) after an electrical connection is established. A modification of the electrode's separation changes the capacitance of the system. Since there is a potential difference between the electrodes ($\triangle V_{CPD}$), the varying capacitance causes an ac current to flow through the electrical connection. b) Energy configuration after the application of a dc bias voltage to the reference electrode. The bias shifts the Fermi level lower by removing electrons from the reference electrode. This also shifts the level of the vacuum energy. Using the appropriate bias, the vacuum level of the reference electrode is aligned with the vacuum level of the sample. At this point, the current flowing through the circuit is also eliminated (since $\triangle V_{CPD}$=0).

applied bias voltage. However, unlike the macroscopic Kelvin probe, the EFM measures the magnitude of the electrostatic force acting on an AFM tip. By using an AFM tip as the reference electrode for a Kelvin probe, the lateral resolution is greatly increased.

To better understand the operation of an EFM, consider a conducting cantilever tip (radius $\approx$ 20 nm) $\approx$ 10-100 nm from the sample's surface while being vibrated at a frequency of ω_r near its resonance frequency ω_0 (Fig. 2.4). For this situation, the tip-sample potential difference is modified by connecting the cantilever to a controlled bias voltage. The electrostatic force created by the modification of the tip-sample potential difference, as well as, additional surface forces are detected by a force detector located behind the cantilever.

As discussed earlier, a number of different forces act on the tip when it is close to the sample's surface. The total force acting on the tip is a combination of the electrostatic force, the van der Waals force and a mechanical force due to the piezovibrator (driven at a frequency ω_r). If a potential difference $\triangle V$ (in units of volts) exists between the tip and sample (in the case of a metallic or semiconducting substrate $\triangle V = \triangle V_{CPD}$), then the tip experiences a force as a result of the tip-sample capacitance gradient. There may also be a Coulomb force due to the interaction of the tip's trapped charge with its image. The total force acting on the tip-cantilever system is given by [19]

$$F_{tot}(z_o, t) = k(z - z_o)\sin\omega_r t - F_{vdW} - F_{image} - \frac{1}{2}\frac{dC}{dz}\triangle V^2 \ , \qquad (2.11)$$

where z_o is the equilibrium separation distance between the sample and substrate. The force due to the capacitance gradient of the tip-sample system ($-\frac{1}{2}\frac{dC}{dz}\triangle V^2$ part of Eq. 2.11) is the component of the electrostatic force that the EFM measures.

The methods used for measuring the electrostatic interaction (the $\frac{dC}{dz}$ term of Eq. 2.11) with current AFM technology is based on well-established techniques found in the literature. [20–25] Unlike the macroscopic Kelvin probe, where the current due to the changing capacitance is monitored, the electrostatic force probe monitors the component of the force due to the capacitance gradient of the tip-sample system. To

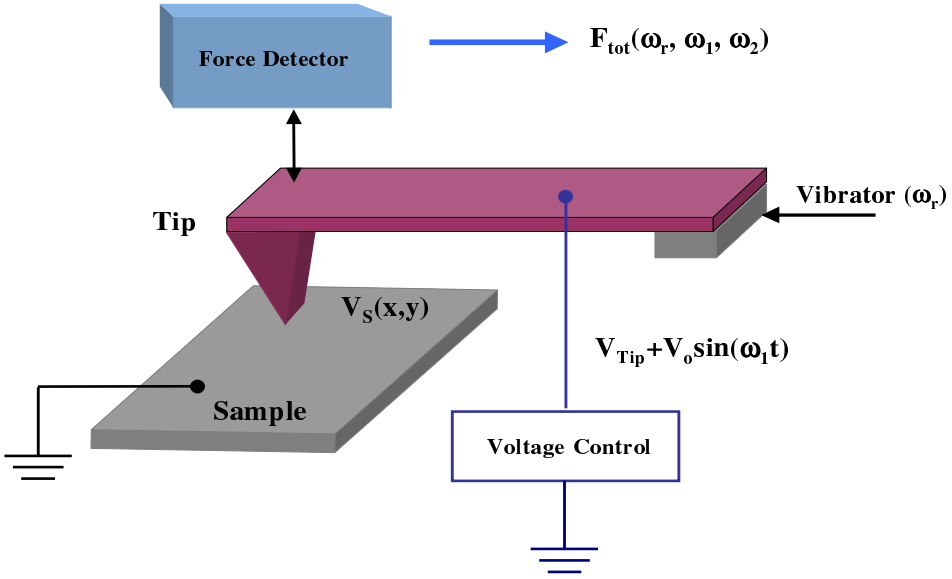

Figure 2.4. Basic experimental setup for a non-contact electrostatic force measurement. The AFM cantilever is vibrated a fixed distance above the sample's surface in non-contact mode. An applied bias voltage is used to modify the tip-sample potential difference and therefore, the electrostatic force acting on the tip. The force detector measures all components of the forces acting on the tip. By using phase sensitive detection, the electrostatic component of the force (ω_1) can be extracted from the detector's output.

eliminate the electrostatic force acting on the tip, a bias voltage is placed on the tip to modify the $\triangle V$ that exists between the tip and sample. This bias voltage is a combination of a dc offset voltage (V_{Tip}) and ac dither voltage driven at ω_1 (Fig. 2.4). The contact potential difference between the tip and sample becomes

$$\triangle V = V_S(x,y) - (V_{Tip} + V_o \sin \omega_1 t) \quad , \tag{2.12}$$

where $V_S(x,y)$ is the sample's surface potential and V_0 is the amplitude of the dither voltage. The force due to the capacitance gradient of the tip-sample system is given by

$$-\frac{1}{2}\frac{dC}{dz}\triangle V^2 = -\frac{1}{2}\frac{dC}{dz}[(V_S(x,y)-V_{Tip})^2+2(V_S(x,y)-V_{Tip})V_o \sin \omega_1 t+\frac{V_o^2}{2}[1-\cos 2\omega_1 t]] \ . \tag{2.13}$$

The same force-sensing scheme used for a normal AFM can also be used to measure electrostatic force caused by the capacitance gradient. However, the output from the force detector is a combination of static and periodic forces. Since this electrostatic force is varying periodically in time with frequency ω_1 (where $\omega_1 \neq \omega_r$), phase sensitive detection can now be used to lock-in on the ω_1 component of the force and extract it out of the force detector's output. The amplitude of the ω_1 component (A_{ω_1}) measured by a phase sensitive detector (PSD) is given by

$$A_{\omega_1} = -\frac{dC}{dz}V_o(V_S(x,y) - V_{Tip}) \quad . \tag{2.14}$$

The amplitude of the ω_1 force component is zero when $V_S(x,y) = V_{Tip}$. By adjusting V_{Tip} (modifying the tip's Fermi level) until the ω_1 component is eliminated, the surface potential of the sample $V_S(x,y)$ is measured. In the case of a metallic or semiconducting substrate, the V_{Tip} required to eliminate the ω_1 force component is $\triangle V_{CPD}$. This is similar to the "flat band condition" of the macroscopic Kelvin probe.

When making EFM measurements, it is necessary to maintain a fixed tip-sample separation. Therefore, variations in A_{ω_1} are only caused by the tip-sample potential difference ($V_S(x,y) - V_{Tip}$). The tip-sample separation can be controlled by using the ω_r component of Eq. 2.11.

When the tip is in close proximity to the sample ($\approx$ 5-10 nm), damping forces from the sample's surface will cause the resonance frequency ω_o of the cantilever to shift. [26] Shifts in the cantilever's resonance frequency cause changes in amplitude of oscillation at the fixed frequency ω_r. The dependence of the ω_r amplitude on tip-sample is used to maintain a fixed tip-sample separation. This is accomplished by adjusting the tip-sample separation in such a way as to maintain a constant ω_r amplitude. The process of using the ω_r amplitude to control the tip-sample separation will be discussed in Chapter 3.

There are several techniques for making electrostatic surface measurements. The simplest method is to keep V_{Tip} a constant while measuring the electrostatic force and topography as a function of position (x, y). These maps can show relative changes in the electrostatic force due to the varying surface potential of the sample.

The benefit of this method is the lack of controlled modifications to $\triangle V$ (no feedback control for the EFM signal). For this type of EFM imaging, the measured electrostatic force is a combination of interactions of the tip and cantilever with the substrate. Since the dimensions of the cantilever are several orders of magnitude larger than the actual tip, the electrostatic force acting on the cantilever results from the interaction with a large area of the substrate, masking any nanometer-sized variations in the surface potential. Therefore, any nanometer-size variations in the EFM image are due to the local interaction of the surface with the tip. By passively monitoring the electrostatic force, troublesome effects, due to the long-range electrostatic interaction of the cantilever beam with the surrounding substrate, are minimized.

By monitoring the phase of the ω_1 component, the relative polarity of the surface potential variations is determined; thereby providing information on the polarity of charge densities on the sample's surface. [5,24,27,28] However, the passive method of recording the electrostatic potential variation cannot provide an accurate measure of the surface potential. In order to make accurate surface potential measurements, a controlled modification of the electrostatic force acting on the tip is required (similar to the Kelvin probe).

To measure the surface potential as a function of position requires a feedback circuit that actively modifies the tip bias voltage (V_{Tip}). The feedback circuit measures the magnitude of the electrostatic force and then uses the bias voltage to hold the amplitude of the ω_1 component at zero. By recording V_{Tip} as a function of position (x, y), a map of the actual surface potential $V_S(x, y)$ is generated.

A major problem with this technique is due to the large area interaction of the cantilever with the substrate. In certain cases, the electrostatic force acting on the cantilever can dominate the forces experienced by the tip. When the feedback system eliminates the ω_1 component, the applied voltage will mostly be the measured potential of a large area of the sample's surface. This has the effect of decreasing the lateral resolution. Therefore, the measured surface potential, which occurs on the nanometer length scale, will not be an accurate representation of the actual surface potential at that particular location. This convolution of the electrostatic force between small objects relative to the tip will be discussed in more detail in later sections.

The experimental methods mentioned above can also simultaneously acquire measurements of both the surface topography and the electrostatic force. This proves to be a useful tool for correlating surface potential with surface topography. [21] However, both techniques have problems that make it difficult to determine the sample's surface potential accurately.

A simple way to make accurate measurements of the surface potential is to use samples with surfaces that are homogenous over dimensions much larger than the cantilever beam. For this situation, the tip and cantilever interact with a uniform equipotential surface. During the measurement, the tip is held in a fixed position. Since the samples are uniform, no information is required for the local variation of the sample's potential. While maintaining a fixed tip-sample separation, which is controlled by the non-contact feedback, the magnitude of the ω_1 force is measured as a function of tip bias voltage. When the tip obtains the voltage that is necessary to null the electric field between the tip and sample, there will be a minimum in the electrostatic force signal. By using this technique in conjunction with samples that

are homogenous at length scales larger than the cantilever beam, it is possible to make accurate measurements of the sample's surface potential.

In addition to the surface potential measurements (the ω_1 component), the relative changes in the tip-sample capacitance are also measured by monitoring the second harmonic of ω_1 ($2\omega_1$). From Eq. 2.13, the magnitude of the second harmonic of the EFM force signal $A_{2\omega_1}$ is given by

$$A_{2\omega_1} = -\frac{dC}{dz}\frac{V_o^2}{2} \quad . \tag{2.15}$$

There is no direct dependence of the magnitude of the $2\omega_1$ component on the potential difference between tip and sample. Since the topographic feedback is maintaining a fixed tip-sample separation and V_o is fixed, variations in the $2\omega_1$ component are due to variations of the capacitance (dC term). This component can be measured simultaneously with topography; thereby, producing a map of the variations of tip-surface capacitance.

This technique is referred to as scanning capacitance force microscopy (SCFM). In the last several years, SCFM has also emerged as a useful tool for electrical characterization of nanoscale electronic structures. [29, 30] However, the remaining discussion of the work presented will remain focused on surface potential measurements using the ω_1 component of the force. The next section will introduce the apparatuses used for the initial surface potential studies of nanoscale objects.

3. EXPERIMENTAL APPARATUS

3.1 Principles of AFM Operation

Since an EFM is a modified AFM, it is useful to understand how an AFM functions. [25] AFM measurements result from controlling the interaction forces between a tip (usually a nanometer-sized proximal probe) and a sample's surface as a function of position. The forces acting on the tip cause the cantilever to deflect. The amount of deflection is related to the strength of the surface forces acting on the tip. Controlling the tip's interaction with the surface requires both sensitive detection of the cantilever's deflection and high-resolution positioning of the sample.

The basic system design for an AFM is shown in Fig. 3.1. An AFM consists of three major components: the sample positioning system, the force detector and the feedback control system. Each of these crucial components will now be discussed in more detail.

High-resolution positioning of the sample is obtained by using devices constructed from piezoelectric ceramics. Piezoelectric ceramics have the capability of easily positioning a sample with a nanometer resolution along the x, y and z directions. Piezoelectric positioning devices consist of a machined piece of ceramic placed between two metal electrodes. When a potential difference is placed across the electrodes, the piezoelectric ceramic will expand or contract in a direction that is perpendicular to the applied electric field. The motion of the ceramic is controlled by the polarity and magnitude of the applied voltage.

The most widely used piezoelectric positioning device is the piezotube. A piezotube is a hollow cylindrical shaped piece of ceramic that has one electrode on the inner surface and four equally space electrodes on the outer surface. Biasing the outer electrodes moves the tube in $\pm x$ and $\pm y$ directions. Biasing the inner electrode

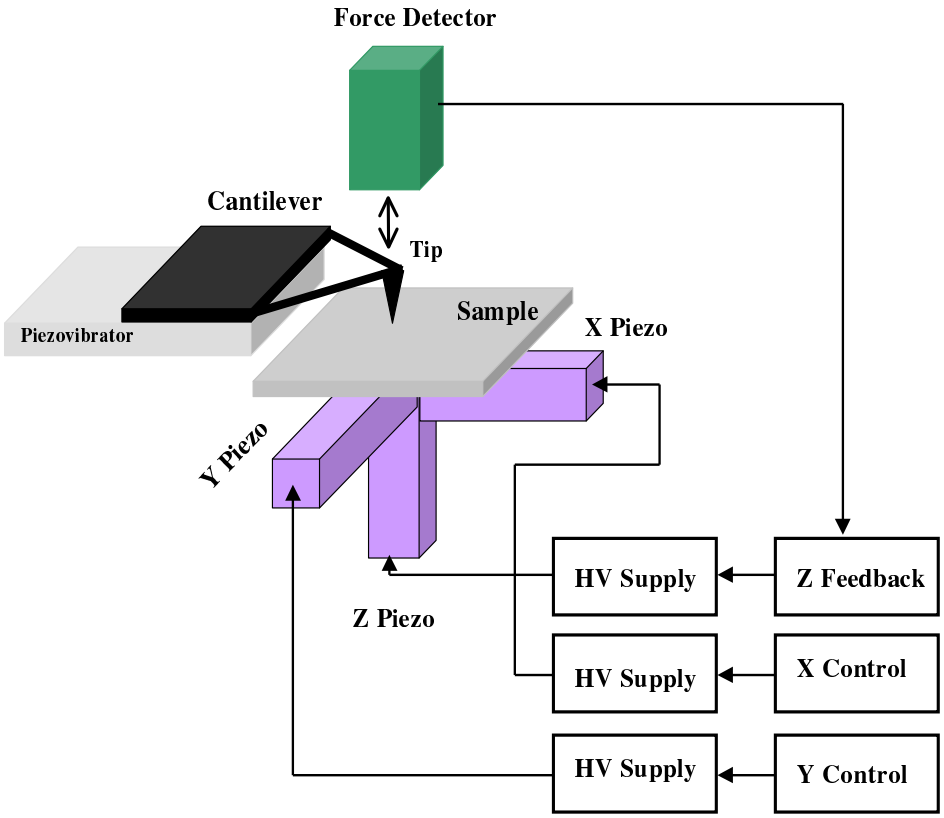

Figure 3.1. Basic AFM system design.

controls the tube's motion in the $\pm z$ direction. A control system provides the high voltage that is required for moving the sample (relative to the tip) to each position of the scan.

For a typical AFM scan, the forces are probed at many different positions within a square region of the sample's surface. During the scan, force measurements are made along incremental positions on the x-axis. After sweeping along the x-axis, the y position is incremented by one step along the y-axis. Once at the new y position, the forces acting on the tip are again incrementally measured along the entire length of the x-axis. This process continues until the tip has transversed along the length

of the y-axis. The resolution of the scan is controlled by both the scan size (size of square region) and the size of the x,y steps.

As the tip is moved over the sample's surface, forces interacting with the tip cause the cantilever to deflect. Since the cantilever behaves like a spring, the forces acting on the tip can be determined by measuring the amount of cantilever displacement. The deflection is detected by a position sensitive detector that is located behind the cantilever. The sensor generates an output voltage that is proportional to the cantilever's deflection.

During a typical AFM scan, the deflection of the cantilever is held constant (constant force) for each position (x, y). The static force is maintained by a feedback system that is monitoring the output of the deflection sensor. The feedback maintains the static deflection by adjusting the applied voltage to the z piezoelectric element. The bias voltage applied to the z piezoelectric element (V_z) is adjusted until the deflection of the cantilever is the same as the set-point value used by the feedback system. The applied V_z is recorded for every position of the scan, providing information in a Cartesian (x, y, z) coordinate system.

The topographic height at a particular position (x, y) is determined by recording the amount of V_z that was applied to the z piezoelectric element to maintain a constant deflection. V_z is converted into an actual height (in nanometers) by knowing the z expansion of the piezotube for a given applied bias voltage. The z expansion of the piezotube for a particular bias voltage is known as the tube's z calibration and is given in nm/V. Similarly, the x and y portions of the piezotube have their own separated calibrations.

Control and feedback systems can either be analog or digital. Analog systems are electronic circuits built to control both the positioning of the tip and the z-positioning feedback. Analog systems are easy and inexpensive to build, but are very hard to modify. Digital systems use computers and software to control the feedback and positioning systems. To modify a digital system, one has only to change the scanning algorithm in the software. This is a much easier process than removing and altering discrete electronic components.

The two dominant methods for measuring the surface topography as a function of position are contact and non-contact modes. In contact mode the tip is in actual physical contact with the surface. The cantilever deflection is dominated by the repulsive interactions between the electron densities of the tip and sample. [25, 26] Scanning in this mode can damage weakly bound objects of the sample's surface.

Non-contact mode offers a solution for probing weakly bounded objects on a sample surface. During a non-contact scan, the tip is vibrated near its resonance frequency approximately 5-15 nm above the sample. Since the cantilever is being driven mechanically at a frequency ω_r, damping forces from the sample's surface will cause the resonance frequency ω_o of the cantilever to shift. When the tip moves relative to the surface, the damping forces alter the resonance frequency of the cantilever. This also changes the amplitude of oscillation at the fixed frequency ω_r. The damping of the ω_r oscillation can be used to maintain a fixed tip-sample separation. This is accomplished by measuring the amplitude of the ω_r force using a phase sensitive detector (PSD). The output of the PSD is used by the feedback system to maintain a constant amplitude of ω_r. By recording the adjustment of the z piezoelectric element required to maintain a constant ω_r amplitude, a topographic profile of the surface is generated.

One of the major drawbacks of using non-contact mode is the loss of lateral resolution. This occurs, because the tip is not in physical contact with the sample surface. Since the tip is positioned above the surface, it experiences long-range forces from a larger area of the sample's surface than in contact mode. Therefore, the lateral measurement of the force interaction is convoluted. However, recent advances in AFM technology have minimized the effects of tip convolution. [31]

The two scanning modes mentioned above are not the only modes possible. Using a flexible control system allows the AFM to probe a multiple of different surface forces such as adhesion, friction, magnetic and electrostatic using different scanning modes. [7–9] For this work, the dominate scanning modes were electrostatic force and non-contact. The following sections will discuss in detail the instrumentation used to measure the electrostatic force near a sample's surface.

3.2 EFM Instrumentation

The EFM measurements reported in this work were conducted on two AFMs that had the capability of making measurements in a variety of different environments. Initial EFM experiments were conducted on a commercial air AFM manufactured by Nanotec^{TM}. [32] Later electrostatic experiments were conducted in a high vacuum environment with a homebuilt AFM base on a fiberoptic force sensor. The same basic experimental configuration was used to make electrostatic measurements on both instruments.

Figure 3.2 is a general schematic of the experimental setup used to make electrostatic measurements. This experimental setup is capable of simultaneously measuring both surface morphology (red loop) and the electrostatic force (blue loop) as a function of position. These measurements are based on the techniques discussed in the last Chapter 2.

The red loop in Fig. 3.2 represents the control system used to measure the surface topography. Topographic information is gathered by vibrating a cantilever above the sample with a frequency ω_r (close to the resonance frequency ω_o). Surface forces will dampen the oscillation as the tip-sample spacing changes. The damping is detected by a phase sensitive amplifier referenced to the frequency driving the piezo-vibrator (topo lock-in in Fig. 3.2). The output of the lock-in is used by the Nanotec control system to maintain a fixed tip-sample spacing.

The blue loop in Fig. 3.2 indicates the components used to measure the electrostatic force acting on the cantilever's tip. An independently controlled dc tip bias voltage (V_{Tip}) is combined with a dither voltage driven at ω_1 using a summing amplifier (see Appendix A). This combination of voltages is applied to the cantilever. Based on theory described in the last chapter, the bias voltage modifies the electrostatic potential difference ($\triangle V$) between the tip and sample, creating an electrostatic force with a frequency of ω_1. Using the same type of phase sensitive detection as for the topographic loop, a separate lock-in amplifier detects the ω_1 component of the electrostatic signal from the output of the force detector (EFM lock-in in Fig. 3.2).

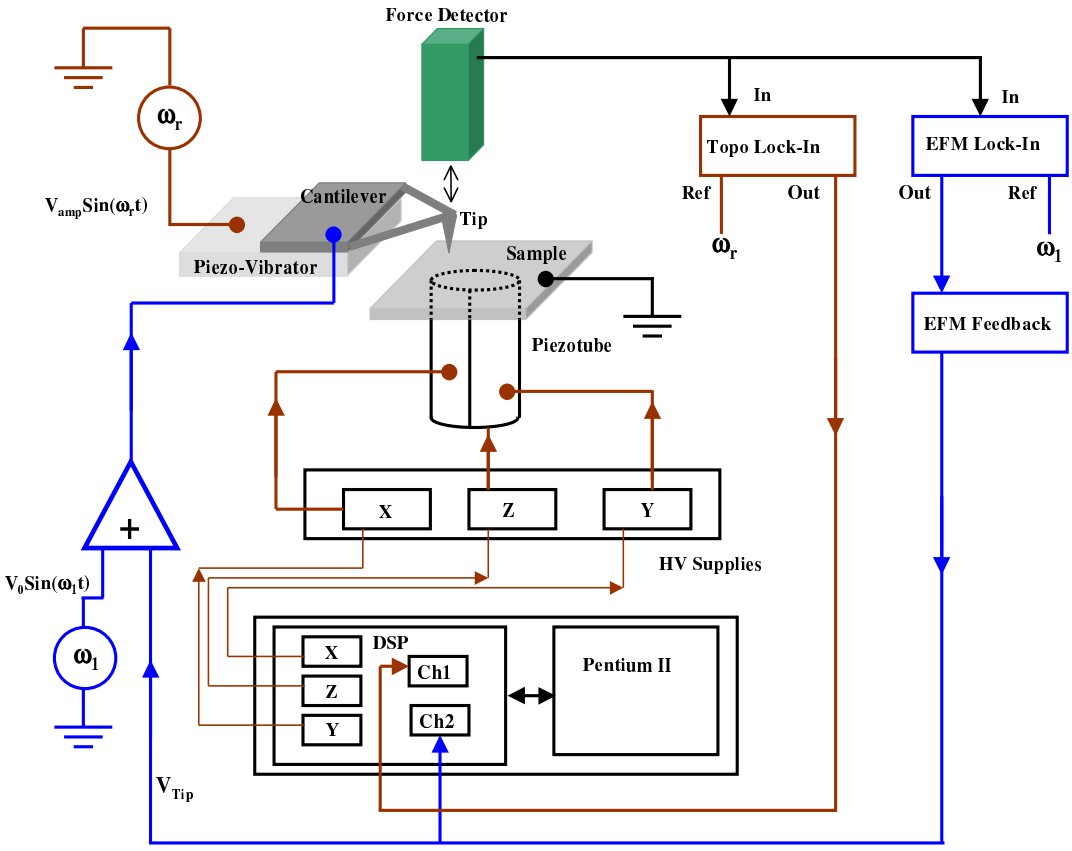

Figure 3.2. Experimental setup used to measure surface topography and electrostatic forces simultaneously.

The force detected by the EFM lock-in is used to determine the surface potential variations on the sample's surface (V_S). The next several sections will discuss various mechanical components of each instrument in detail.

3.3 Control Electronics and Feedback System

Experiments conducted on both AFMs were controlled using a digital feedback system developed by Nanotec^{TM}. Nanotech's controller is based on a Digital Signal Processing (DSP)architecture. In our system we use a Spectrum^{TM} model PC/C31 DSP board. The DSP board is interfaced to an ISA slot on the motherboard of a 233 MHz Pentium personal computer.

The DSP board acts as a stand-alone computer, capable of running small C programs. Programs running in the DSP's memory control the various vital components of the AFM such as the force feedback and positioning (x, y). The PC shares common memory locations with the DSP board, allowing for fast data transfer between the PC and DSP. Software running on the PC, provides a graphical user interface that communicates with the DSP board using the shared memory location.

The piezotube (used for sample positioning) is controlled by several high voltage power supplies. The outputs from the amplifiers are applied to the $\pm x$, $\pm y$ and $\pm z$ elements of the piezotube (Fig. 3.2). High voltages ($\pm$ 150 Volts) originate as low voltage control signals from outputs on the DSP board. The DSP contains four digital-to-analog converter (DAC) outputs. Three are used to supply the control voltages used by piezotube's power supplies (DAC 1-3) and the fourth DAC is used as a stand-alone bias voltage source (DAC 4).

A constant deflection of the cantilever is maintained by the Nanotec feedback electronics. Output from the force sensor is sent to a conditioning amplifier. After conditioning, the output is then sent to one of four analog-to-digital converters (ADC) located on the DSP board. The DSP's software algorithms control the deflection by monitoring the digitized voltage from the deflection sensor.

The software controlling the force feedback uses a Proportional-Integral-Derivative (PID) algorithm. [33–35] The relative influence of each feedback parameter (such as P, I, D) can be altered from the software's PC interface. By controlling the feedback parameters, the feedback can be precisely tuned for any scanning situation. This adds a high degree of flexibility to any AFM that uses this control system.

The control software also has the ability to record additional input channels simultaneously during the scan (using the free ADCs). This feature is very useful when making EFM images where the electrostatic force is recorded as a function of position while the feedback is maintaining a constant tip-sample separation.

3.4 The Air AFM

Due to its convenient design, the Nanotec^{TM} air AFM was found to be a useful instrument for conducting the initial electrostatic studies. The AFM's design allows for a rapid change of samples and tips; thereby, making the task of studying several samples within a short time period relatively easy.

The Nanotec^{TM} AFM detects surface forces using a standard laser beam bounce detection scheme. [36, 37] Figure 3.3 displays a mechanical configuration of the air AFM system. The head of the AFM supports the laser diode [38], cantilever holder and photodiode detector [39]. The beam emitted from the laser diode enters a series of prisms [40] that are used to position the laser beam onto the back of a reflecting cantilever. When cantilevers are mounted in their holder, they are tilted at a slight angle. The tilt of the holder causes the cantilever's reflected laser beam to be directed into a photodiode detector. The photodiode is located on an alignment stage, which is used to easily position the photodiode in the path of the reflected laser beam reflected.

The force detector used for this AFM design is a quadrant photodiode [39] (a photodiode that has been divided into four individual segments). As the cantilever is deflected, the reflected beam's position shifts relative to the individual sensing elements of the photodiode. The relative change in the intensities of each sensing element is used to determine the physical deflection of the cantilever. [36]

The advantage of using a quadrant photodiode is the simultaneous measurements of forces acting in the z direction (normal force) and x, y directions (lateral force). The normal force detector is used to measure such quantities as the z-dependence of the forces and z topographic heights. While the lateral force detector is useful for measuring frictional surface forces.

Making EFM measurements requires an electrical connection to the cantilever vibrated near its resonance frequency. Vibration of the cantilever is accomplished by a piezo-vibrator that is glued to a conducting tip holder. The cantilevers are attached to the tip holder using conducting epoxy [41], allowing application of electrical signals to the tip (via the conducting tip holder) while the cantilever is vibrated for non-contact measurements.

The entire AFM head rests on a tripod formed by two micrometers located in the front of the instrument, and a DC motor controlled micrometer located in the rear. The front two adjustment micrometers are used for i) orientating the tip relative to the sample's surface and ii) coarse approach. Fine-approach is executed by the rear micrometer under DC motor control. As the rear micrometer is lowered, the head pivots about the front micrometers, lowering the tip closer to the sample's surface.

The samples are magnetically mounted to a 2-inch PZT-A piezotube located on the base of the instrument. This allows for the convenient exchange of samples. The magnet used to hold the sample during the scan is coated with a conducting metal. The conducting coating is used to conveniently connect the sample to ground.

A low humidity environment is achieved by placing a bell jar over the entire AFM head and filling the bell jar with dry nitrogen gas. A humidity sensor mounted next to the AFM head monitors the bell jar's environment.

3.5 The Ultra High Vacuum AFM

There are several important reasons why careful EFM measurements should be conducted in a vacuum environment. The primary reason is to eliminate the amount of contamination on the sample's surface. Surface contamination can have the undesired effect of uncontrollably altering the sample's surface potential. Another major benefit of conducting measurements in a vacuum environment is the improvement of the sensitivity and stability of EFM measurements. These reasons were the primary motivations behind the design and construction of an ultra high vacuum (UHV) AFM/EFM. The design of this instrument offers a versatile scanning environment where both small and large samples can be studied under a varity of different atmospheric conditions.

The AFM portion of this instrument uses the same feedback control electronics and software as the air AFM system. The use of this flexible control system, allows the UHV AFM/EFM to measure forces using all the various scanning modes except lateral force.

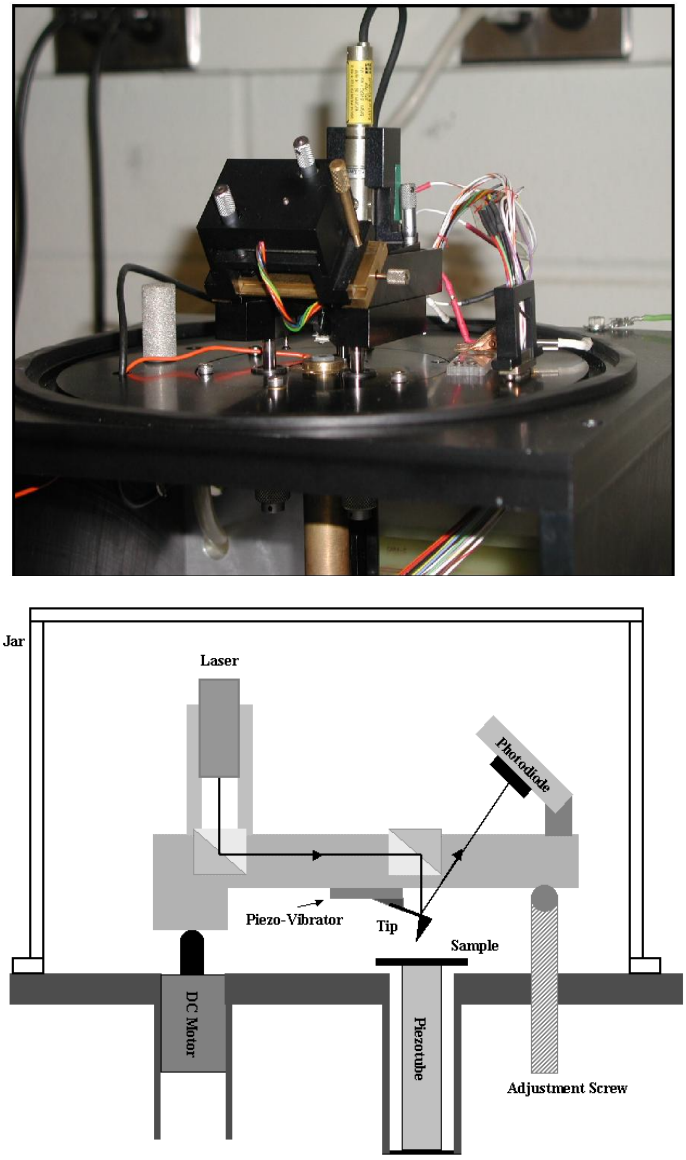

Figure 3.3. The air AFM used for EFM measurements. The AFM was designed and built by Nanotec.

The UHV AFM/EFM can use both ThermoMicroscopes Ultralevers [42] and Piezolevers [43]. Ultralevers are used with optical force detection and Piezolevers are solid-state detectors where the sensing element is integrated into the cantilever.

Piezolevers have an integrated piezoresistive layer built into the cantilever beam. As the Piezolever deflects, the resistivity of the cantilever changes. [44] The surface forces acting on the cantilever can be detected by using an electronic circuit to measure the change in resistivity. Piezolevers offer a non-optical force detection scheme, eg. if the sample is light sensitive. A description for measuring small forces with a Piezolever can be found in Appendix B.

However, Piezolevers are not suited for making EFM measurements due to the nature of their design. Because of techniques that are used for EFM measurements (requiring an application of an ac dither voltage to the cantilever), integrated electronic force detectors are susceptible to stray voltage signals, which manifest themselves as false tip deflections. Therefore, force detection based on an optical sensor is much better for conducting EFM measurements than an integrated electronic force sensor such as the Piezolever. For the reasons mentioned above, Ultralevers are used for conducting EFM measurements. Observations based on initial EFM studies using the air AFM have shown that the Ultralevers work very well for EFM measurements.

The primary optical force detection method used for this system is based on a fiberoptic interferometer. Output of the interferometer, which represents tiny deflections of the cantilever, is used by the feedback system to maintain the constant force on the cantilever. Unlike beam bounce force detection, the fiberoptic interferometer does not require a complex *in-situ* alignment system. This makes the design of the UHV AFM head considerably less complicated.

Figure 3.4 is a schematic of a mechanical design for the UHV AFM/EFM system. The fiberoptic AFM head sits on a support tripod located on the base plate. With this arrangement, large samples with a broad range of thickness (1 mm to 1.5 cm) can be investigated.

In the front of the instrument are located two adjustment screws that form the front two legs of the base tripod. These screws are used to adjust the angle of the fiber head relative to the sample's surface. The adjustment screws are also used to change the spacing between the fiber head and the sample holder.

The back leg of the tripod is formed by the coarse approach system using a Burleigh^{TM} inchworm motor. [45] The inchworm motor is capable of moving loads with a minimum step size of 4 nm. This high resolution makes the inchworm a perfect choice for a coarse approach motor.

The inchworm has a rod mounted along its axis of motion and the whole assembly is attached to the base plate of the system. The rod forms the third leg of the tripod support. When the motor moves the rod to a lower z position, the fiber head pivots about the front two legs of the tripod; lowering the cantilever closer to the sample. Increasing the z position of the rod raises the cantilever farther way from the sample's surface.

The sample is magnetically held on a PZT-5A piezotube that is mounted to the base plate. The design of piezotube holder allows for the convenient exchange of piezotubes that have different maximum scanning ranges.

The entire AFM assembly is attached to a 6-inch conflat flange that connects to the top flange of the vacuum chamber. Mounting the head on the top flange allows for the easy removal UHV AFM/EFM from the main chamber. Figure 3.5 is a photograph of the UHV AFM/EFM head residing inside the vacuum system. The fiberoptic cable exits the vacuum chamber via a small hole in the mounting flange. The hole is sealed with UHV epoxy to prevent leaks.

Figure 3.6 displays the overall layout of the vacuum system. The AFM head is mounted in the main 6-inch chamber, which is attached to both a cryogenic sorption pump and an ion pump. The ion pump is attached to a vibration isolated air table used to reduce the effects of ambient vibrations. Attached to the left side of the main chamber is a small sample storage chamber. A gate value separates the two chambers. This allows for the insertion of samples without removing the head from

the main chamber. The sample storage chamber is capable of storing up to three samples under vacuum conditions. A sample transfer arm moves samples from the storage chamber to the piezotube on the AFM base in the main chamber using a homebuilt manipulator. The sample transfer system provides the ability to change samples without altering the environment of the AFM. This is critical for conducting EFM measurements when it is necessary to probe several samples with the same tip.

The AFM can be exposed to different environments by using this vacuum configuration. Measurements can be made in air, low vacuum (mTorr) and in UHV (10^{-9} Torr) environments. The chamber also possesses a bleed valve that allows various gasses to be back filled into the chamber during EFM measurements.

3.5.1 Optical Interference Force Detection

The AFM measures the sample-tip interaction forces by detecting the tip deflection. There are various ways to detect the deflection, but the UHV system was designed to use a deflection sensor based on a fiberoptical interferometer. Using a fiber interferometer eliminates the need for expensive and complex *in-situ* alignment systems that are required for optical beam bounce detection.

Fiberoptic interferometers have been used for many years to detect the small deflections of cantilevers. Interferometers that are capable of measuring displacements with a sensitivity of 0.08 nm have been reported in the literature. [46, 47] The high sensitivity for measuring displacements make the fiberoptic interferometer an ideal choice for an AFM force detector.

The Purdue fiberoptic interferometer is based on a design found in the literature. [46–50] Figure 3.7 is a schematic of the fiberoptic interferometer. This design consists of a 1310 nm ($\lambda = 1310$ nm) fiberoptic laser diode [51], a 2X2 fiberoptic coupler [52] and a photodiode sensitive to light at the 1310 nm wavelength [53]. The optical fiber used for this interferometer is Corning SMF-28 optical fiber [54].

The interferometer functions by directing the output from a laser diode into a 2X2 fiberoptic coupler ($leg\,1$ in Fig. 3.7). The coupler acts like a beam splitter, sending 50% of the input radiation from $leg\,1$ into $leg\,2$ and $leg\,3$. After passing through the

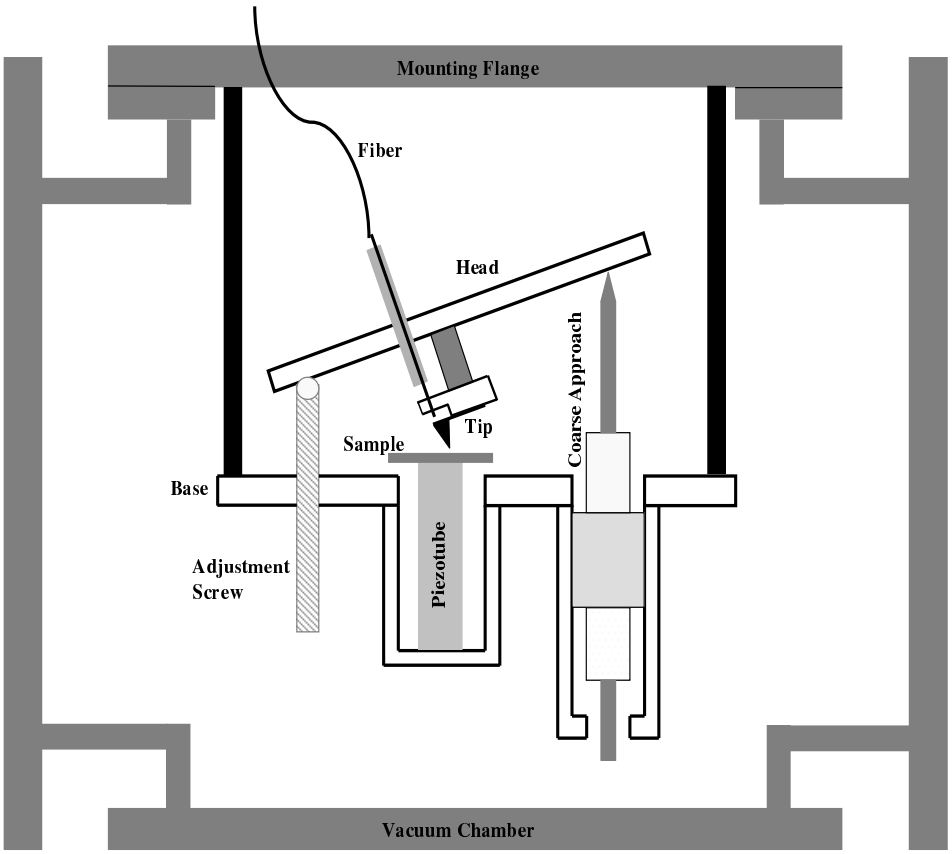

Figure 3.4. Mechanical design for the Purdue AFM/EFM.

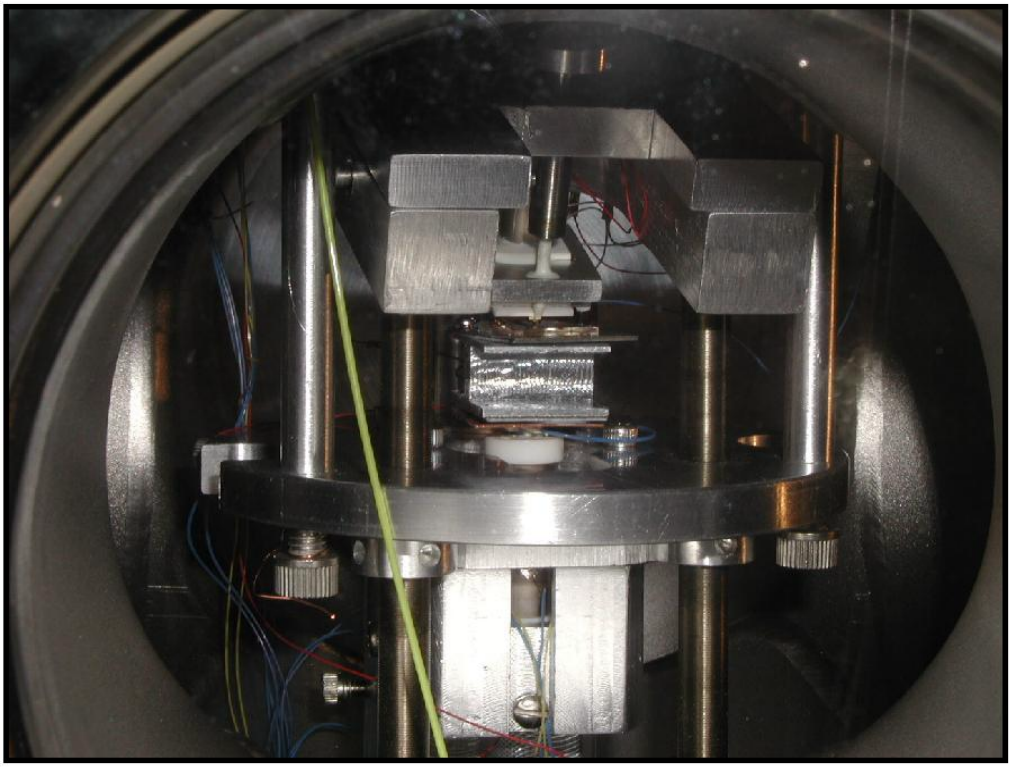

Figure 3.5. The UHV AFM head inside the main chamber.

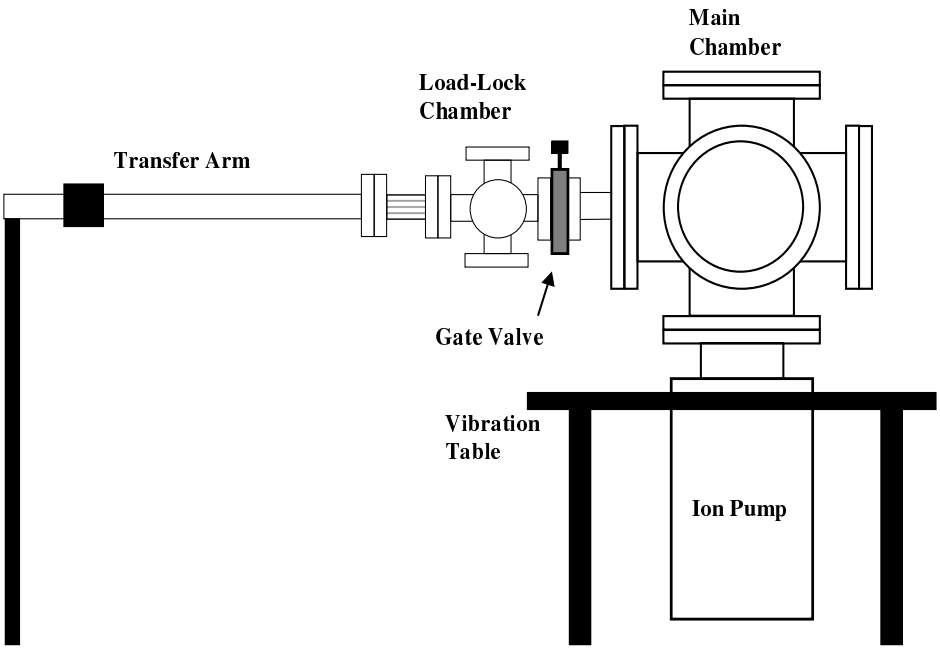

Figure 3.6. Configuration of the vacuum system used for the AFM/EFM system.

coupler, the output radiation travels to the fiber-vacuum interface at the end of *leg* 2. At the end of *leg* 2 the fiber is cleaved at an angle of 0^o, allowing for some internal reflection at the fiber-vacuum interface. The internally reflected beam travels back towards the coupler (one leg of the interferometer). While transmitted light leaving the end of the *leg* 2 fiber is reflected off the cantilever and back into the fiber, this is the second leg of the interferometer (Fig. 3.8). The reflected beams travel back into the 2X2 coupler and 50% of their intensities are directed to the photodiode on *leg* 4. As the distance, $\triangle z$, between the end of the fiber and the cantilever changes, the intensity at the photodiode will change (Fig. 3.9).

The intensity variations from the photodiode can be used to maintain the z piezotube feedback of an AFM. Unlike beam bounce detection, the output of the fiberoptic interferometer has a periodic nature. For the most sensitive force detection, the fiber-cantilever distance should be an odd multiple of $\frac{\lambda}{8}$ (Fig. 3.9). At this particular spacing, the output from the interferometer is approximately linear.

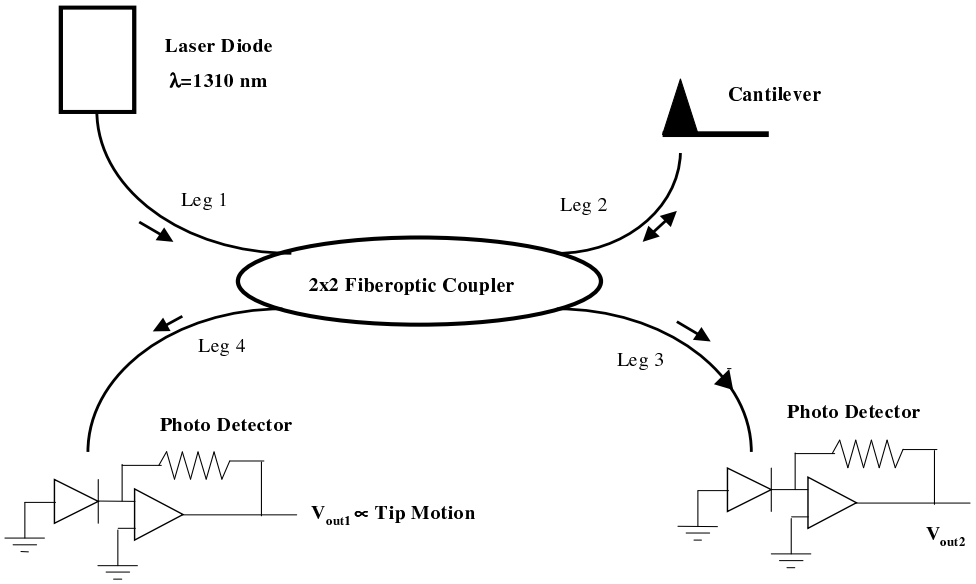

Figure 3.7. Schematic design of the fiberoptic interferometer.

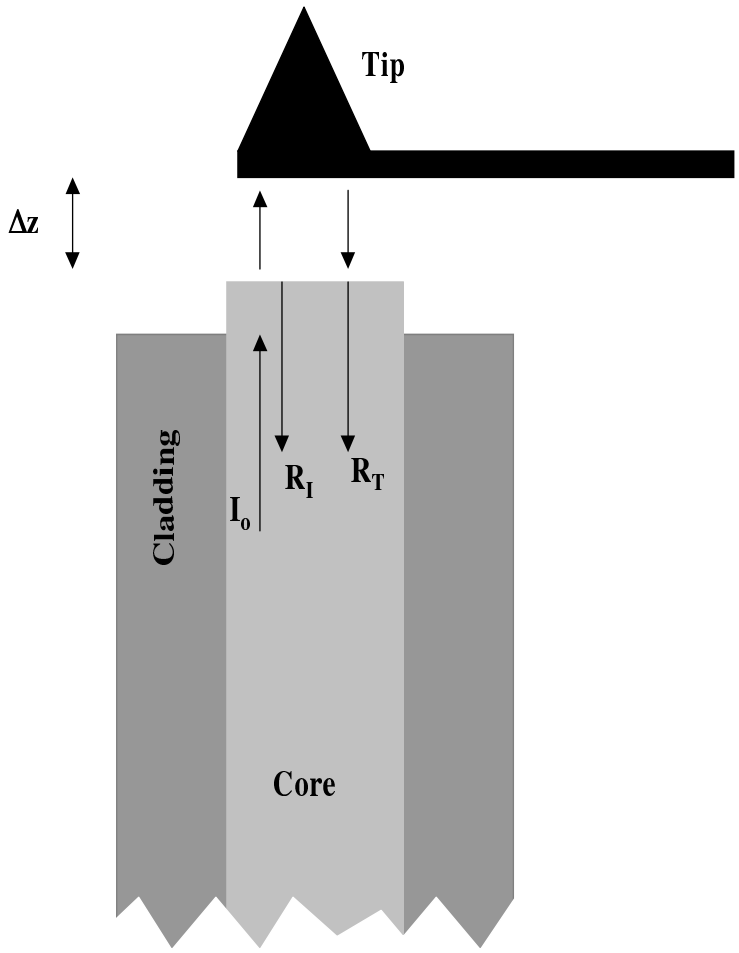

Figure 3.8. Optical cavity formed between the fiber and cantilever.

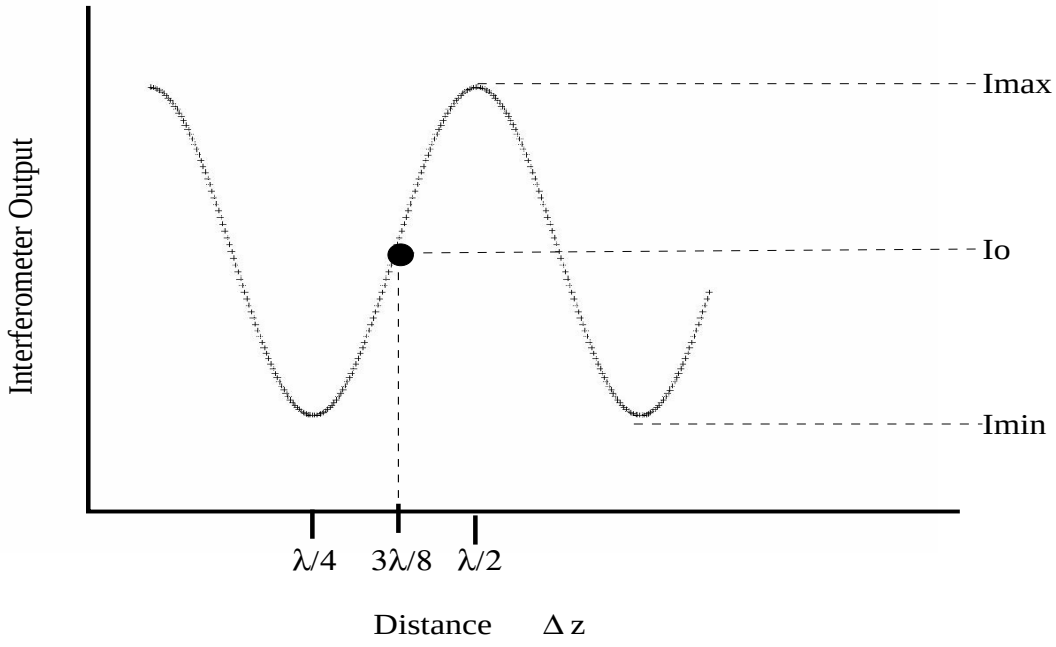

Figure 3.9. The change in the fiberoptic interferometer's output intensity as a function of cantilever displacement $\triangle z$.

3.5.2 Fiberoptic AFM Head

The schematic for the Purdue fiberoptic AFM head is displayed in Fig. 3.10. Cantilevers are glued, using a conducting epoxy, to an Au contact pad that has been evaporated onto a 1 cm $\times$ 1 cm ceramic chip. The ceramic chip is clamped to the tip holder using a spring clip. Electrical signals can be applied to the tip through the spring clip and gold contact pad.

An optical fiber is guided directly behind the cantilever by inserting it through a tiny ceramic wire-bonder capillary that is mounted beneath the chip holder. The fiber is fed through the rear of the capillary where the inner diameter is approximately 1 mm and passes through the capillary' tip. The tip of the capillary tapers down to an inner diameter of 0.2 mm, which makes it ideal for holding the optical fiber (with a diameter of 150 μm) laterally fixed, while allowing the fiber to move freely in a z direction. The chip holder is glued to the top of a 0.5" long PZA-5 piezotube, while the bottom of the piezotube is glued in the head's base, forming a rigid structure.

Cantilever-fiber spacing is controlled by 100 thread per inch coarse approach screw. The coarse approach screw is threaded through a tap hole in the head's base. The screw's rotational axis is aligned with the axis of the capillary. This allows the optical fiber to be threaded through a hole drilled along the screw's rotational axis and then through the capillary. The fiber is glued to the coarse approach screw, holding it stationary with respect to the cantilever. The cantilever-fiber spacing is adjusted by threading the coarse approach screw through the head's base. Typical cantilever-fiber spacing is $\approx$ 10 - 15 μm.

Fine manipulation of the tip-fiber separation can be obtained by adjusting the expansion of the piezotube on which the tip holder is mounted. To achieve maximum sensitivity, the piezotube is used to set the fiber-cantilever spacing to a multiple of $\frac{\lambda}{8}$. Over time, the cantilever-fiber spacing may change due to thermal expansion. The piezotube allows for the adjustment in order to compensate for the thermal drift and maintain the maximum sensitivity.

The piezotube is also used to vibrate the cantilever near its resonance frequency. The cantilever is vibrated by combining a small oscillating driving voltage with the static voltage used for fine control of the cantilever-fiber spacing. Since the oscillation of most cantilevers requires minute amounts of energy, the driving voltage is much smaller than the static control voltage. This reduces the effects of erroneous deflection signals caused by oscillating the actual cantilever fiber spacing.

To change and align new cantilevers, the AFM/EFM head is removed from the tripod support and placed into an alignment jig. Figure 3.11 a shows the head resting on the alignment jig. The alignment jig is a flat piece of metal on which the head's base rests while the coarse approach screw mates with a notch cut into the jig's base. When the head is mated with the alignment jig (Fig. 3.12), the notch on the jig prevents the head of the coarse approach screw from rotating when the entire head is rotated. This is necessary to hold the fiber fixed in space, preventing it from being broken by the rotation of the head. Rotation of the head's base about the coarse adjustment screw modifies the cantilever-fiber spacing. Once the cantilever has been glued to the ceramic chip and clamped to the tip holder, a stereomicroscope is used to laterally align the apex of the cantilever over the core of the optical fiber. After the lateral alignment is made, the fiber-cantilever spacing can be decreased until a strong interference signal is detected.

3.5.3 Testing and Calibrating the UHV AFM/EFM

After the construction of the UHV-AFM, several steps were taken to calibrate the piezotube and to test the AFM's imaging quality. All images were made using Ultralevers.

In order to perform proper AFM experiments, the piezotube's expansion needs to be related to the applied voltage (nm/V). Once the piezotube is calibrated, the voltages applied to the tube can be used to calculate the actual dimensions of features present in AFM images.

The piezotube of the UHV AFM was calibrated by using a calibration grating. The structures on the grating are constructed with well-defined dimensions. A comparison

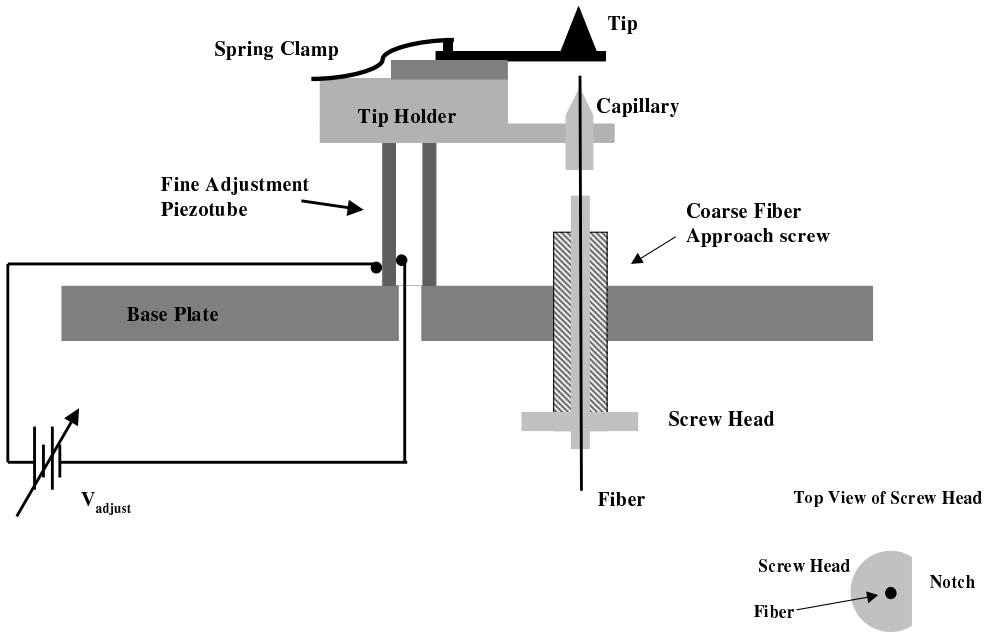

Figure 3.10. Fiberoptic AFM head design.

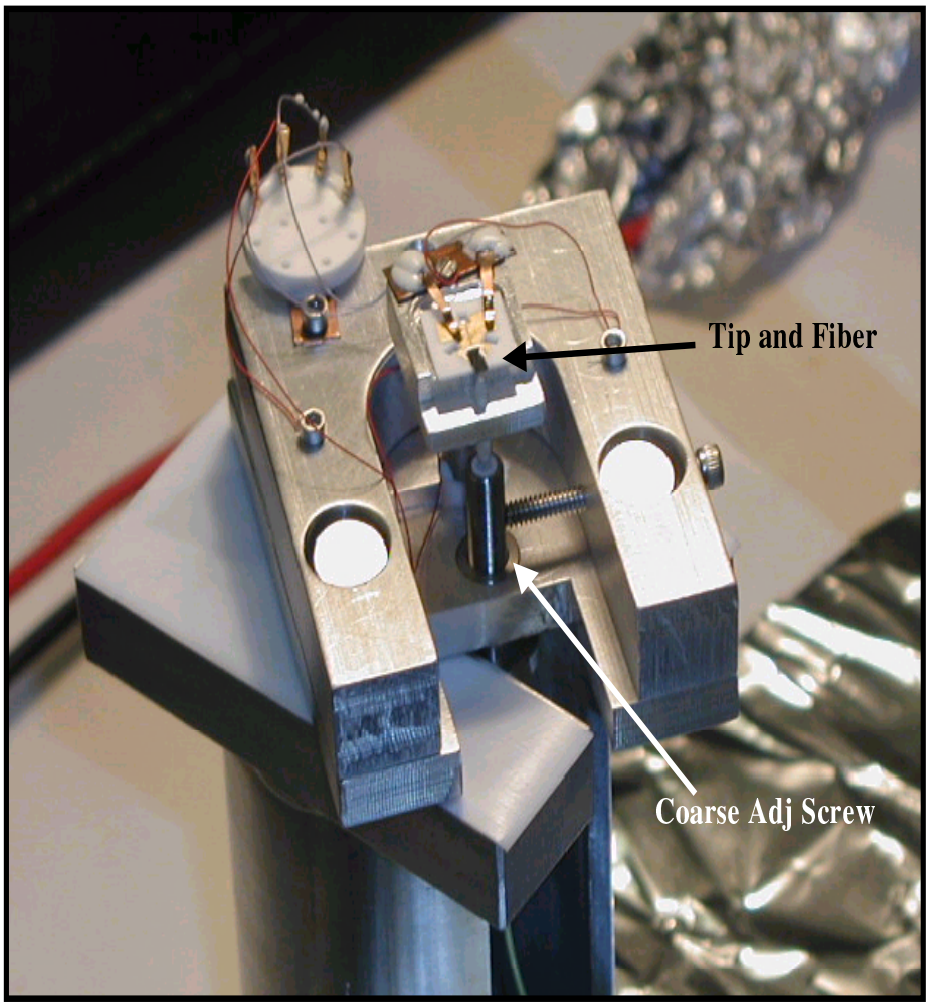

Figure 3.11. A close up picture of the AFM/EFM head resting in the alignment jig.

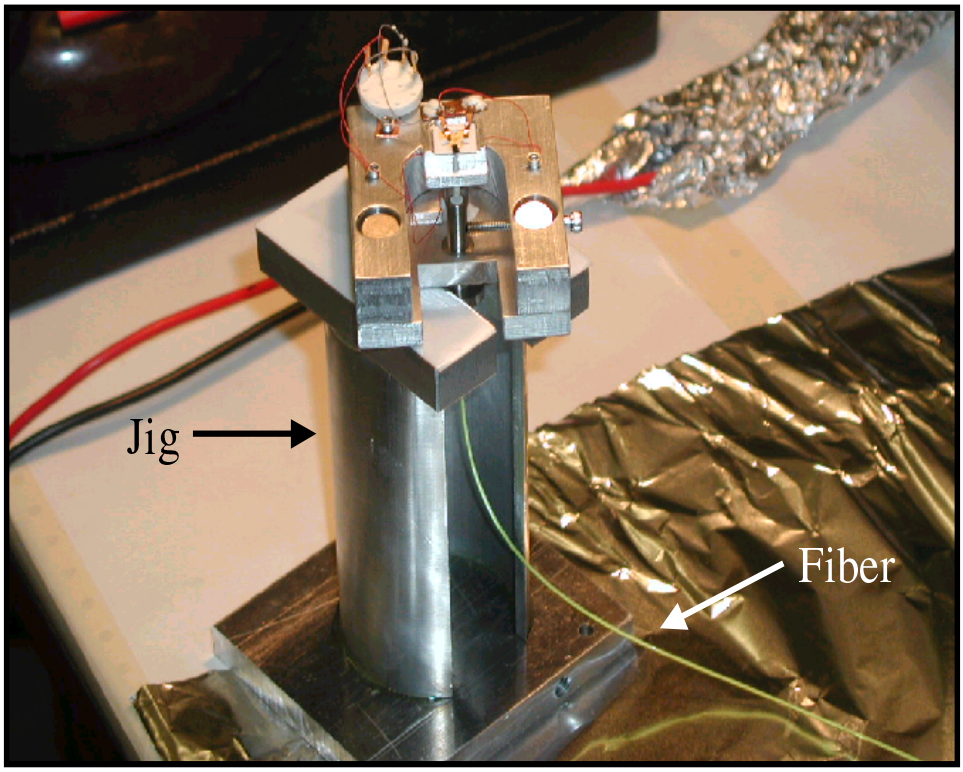

Figure 3.12. The entire AFM/EFM alignment jig.

of the features measured from an image of grating (taken with the AFM) to the actual dimensions of the grating's features, provides a calibration for the tube. Once the tube is calibrated, the dimensions of features present in the image of the grating will coincide with the actual dimensions of the grating's features. The grating used for these calibration experiments has a width of 1.5 μm and a height of 25.5 nm. Figure 3.13 shows a contact scan image of a grating used to calibrate the piezotube.

After calibrating the piezotube, the instrument was configured to make several initial non-contact images. A flamed annealed gold substrate was used to test the stability of the instrument's non-contact imaging. Figure 3.14 displays one of the initial non-contact images produced using the fiberoptic AFM/EFM head design. The image is comparable to images obtained using the air AFM system. Non-contact images were also obtained of 20 nm gold clusters resting on an low temperature grown GaAs (LTG:GaAs) surface (Fig. 3.15).

After verifying the imaging capabilities of the UHV instrument, measurements were conducted to determine the minimum force detected by the interferometer. Several measurements of the normal force as a function of position ($F(z)$) were made using a cantilever with a spring constant of 0.06 N/m. All measurements were made under high vacuum conditions (5×10^{-7} Torr).

Figure 3.16 shows several $F(z)$ curves acquired as the tip was brought into contact with a gold sample. For large separations, the cantilever remains unperturbed, because the surface forces are weak at these distances (section A in Fig. 3.16). As the sample approaches the tip, surface forces become stronger and overwhelm the restoring force of the cantilever. At this point, the tip jumps into contact with the surface (point B in Fig. 3.16). [55,56] The sample continues to move forward loading the cantilever (section c of the Fig. 3.16) until the end of the tube's expansion.

The loading portion of the $F(z)$ curve (section C) is used to calibrate the force sensor. This requires knowing the piezotube calibration and the spring constant of the cantilever. The slope of the loading curve correlates the output of the detector with the actual physical deflection of the cantilever (nm/V). Multiplying the sensors

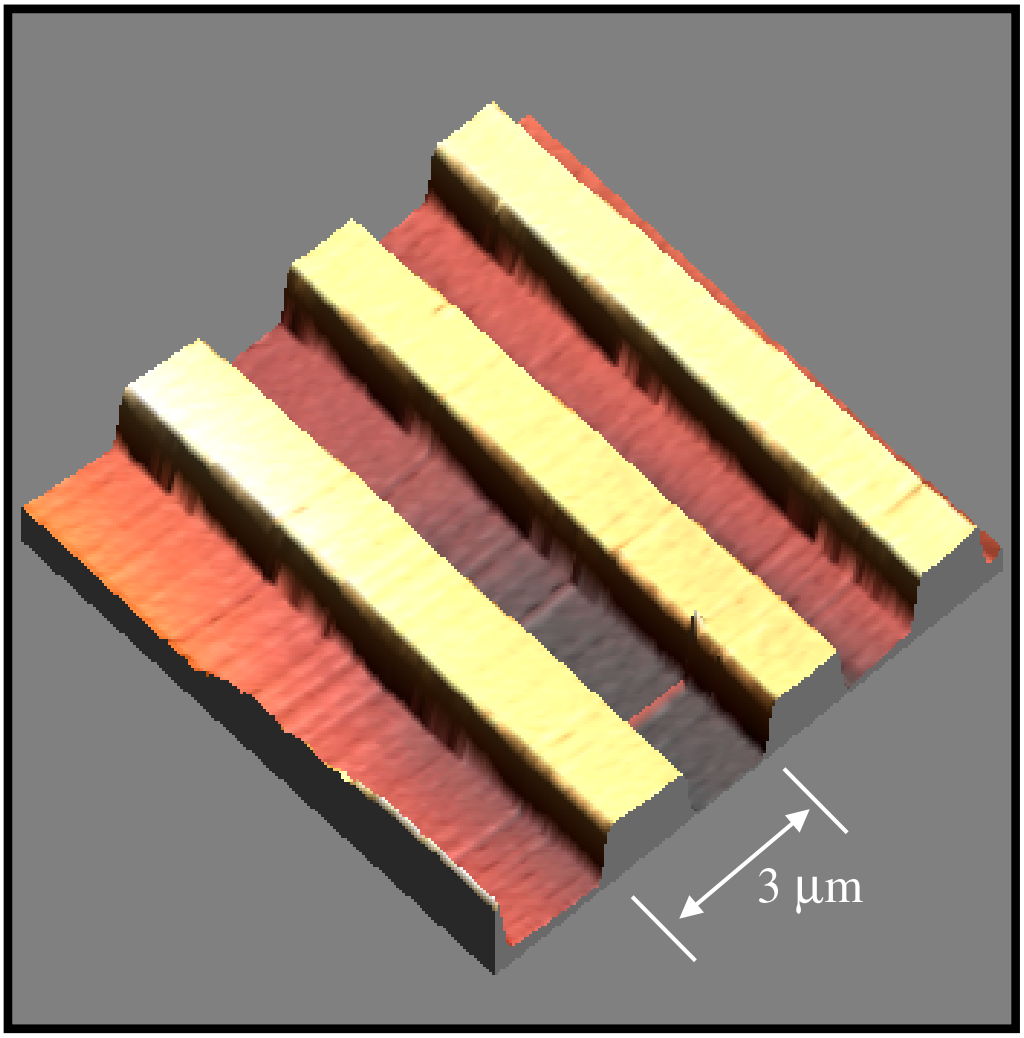

Figure 3.13. Contact image of a calibration grating using the UHV AFM/EFM. The height of the grating is 25.5 nm and the pitch of the grating lines are 1.5 μm.

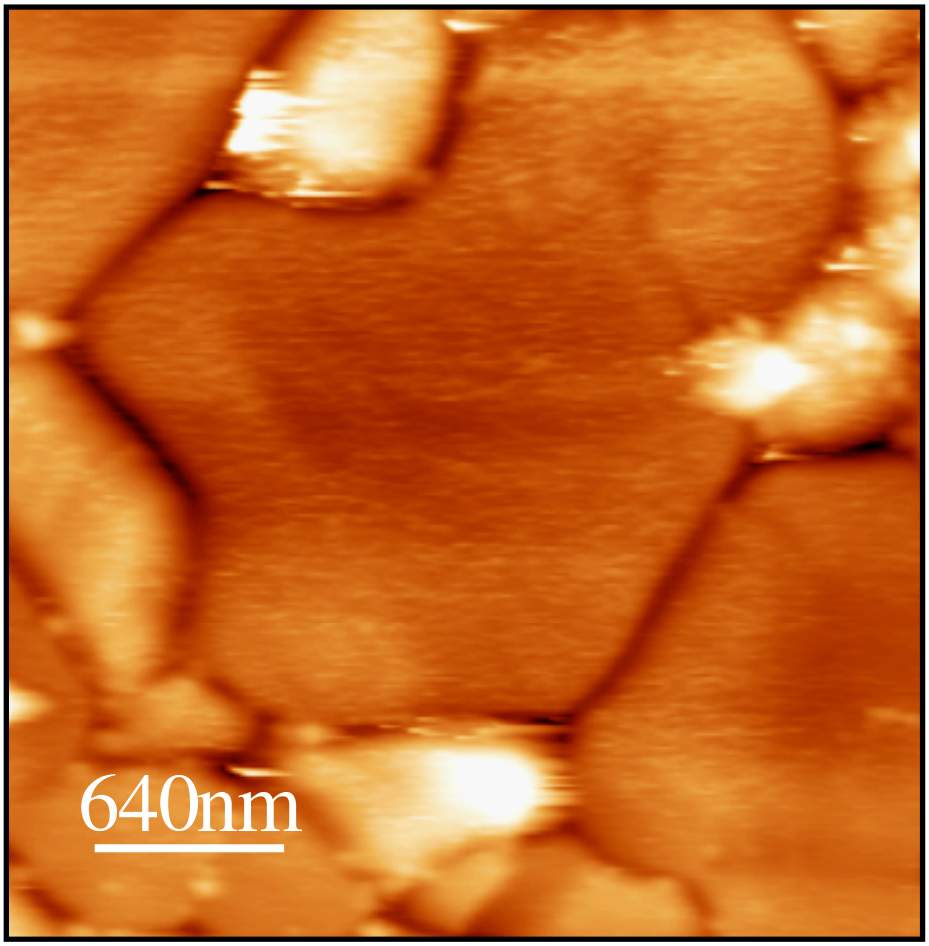

Figure 3.14. Non-contact image produced by the UHV AFM/EFM.

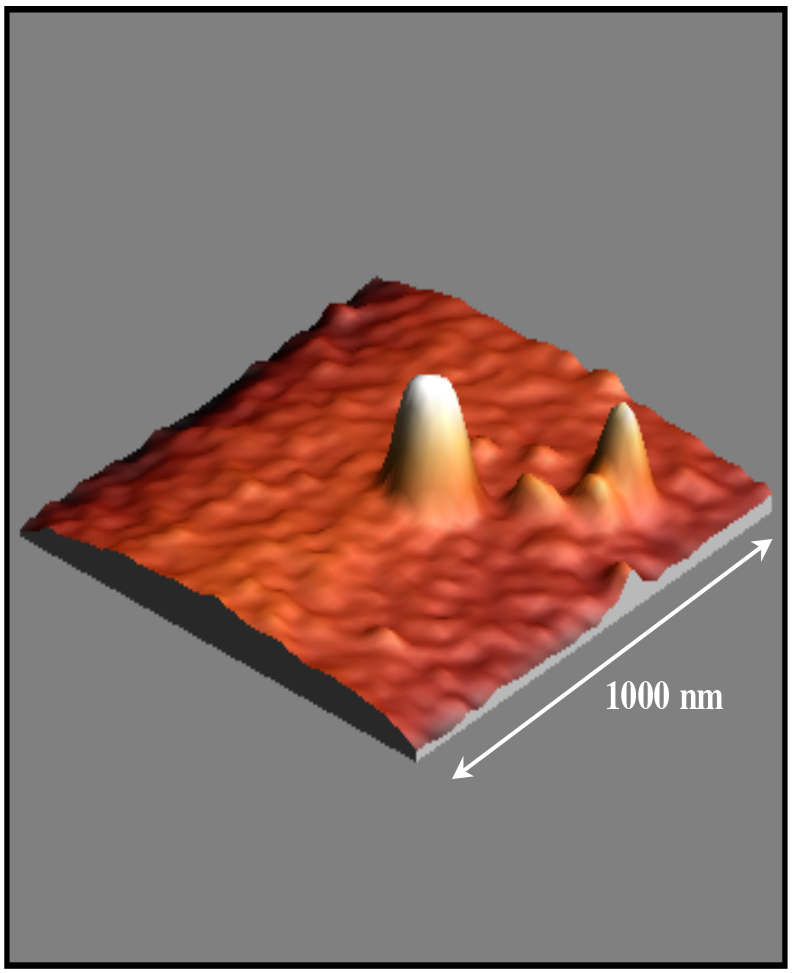

Figure 3.15. Non-contact image of a 20 nm cluster resting on an LTG:GaAs substrate.

calibration (nm/V) by the spring constant of the cantilever (k in units of nN/nm), relates the sensor's voltage output to a force (nN/V).

The $F(z)$ curves in Fig. 3.16 are used to determine the noise limit of the interferometer force detector. From Fig. 3.16 the minimum detectable force using the interferometer is $\pm$ 20 pN. The curves appear reproducible, for several different positions on the sample's surface. These initial calibration studies showed that the instrument was capable of performing at the level required for non-contact electrostatic measurements.

3.6 The Cantilever

The heart of the AFM's force detection system is the cantilever. Cantilevers provide the means for converting the forces acting on the their tips into detectable deflections. Cantilevers are modeled as springs, where the forces can be determined by the cantilever's deflection using Hook's law:

$$F = -k \triangle z \quad . \tag{3.1}$$

To gain accurate measurements of forces acting on the tip, the cantilever's spring constant (k) needs to be accurately determined. Knowing the spring constant and the calibration of the z piezotube, the force sensor's output voltage can be calibrated ($\frac{nN}{Volts}$). With the calibration, the deflection sensor's output voltage can be converted into a force.

There are two main techniques for measuring the spring constant of a cantilever. [57] One method consists of structural analysis using the physical dimensions of the cantilever and the mechanical properties of the material used for the cantilever's construction. The spring constant for a V-shaped cantilever can be calculated by [56]

$$k = \frac{Ewt^3}{2l^3} \quad . \tag{3.2}$$

where E is the elastic modulus, l is length, w the beam width and t is beam thickness. The difficulty with this technique is obtaining the thickness of the cantilever. Typical thickness of cantilevers range from 0.6 μm to 2 μm, making it very difficult to accurately measure the thickness with an optical microscope.

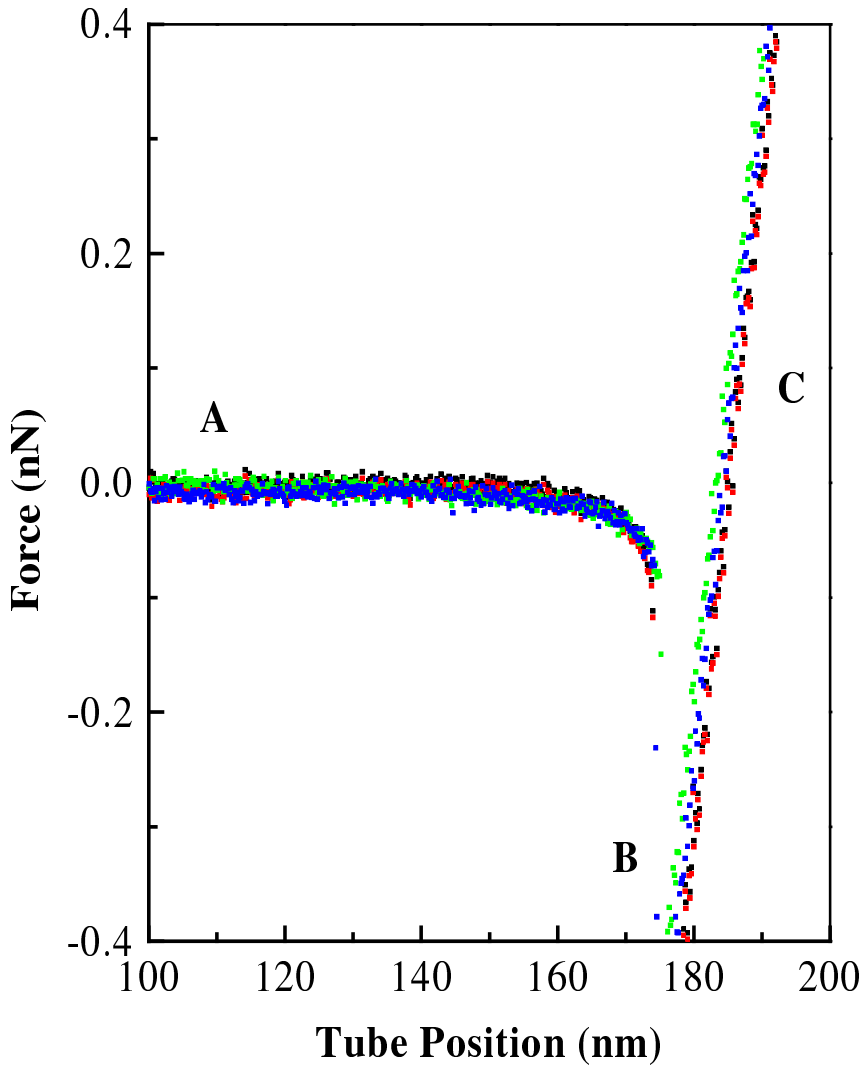

Figure 3.16. Several force vs distance curves measured with the UHV AFM head. Measurements were made at different locations on the sample's surface.

Cantilever Thickness	$0.8\mu m$	$1.8\mu m$
Force constant	0.24 N/m	2.8 N/m
Resonant Frequency	30 kHz	64 kHz

Table 3.1
Typical parameters of the Ultralevers.

A second method has been developed, which excludes the need to measure the cantilever's thickness. This technique relies on measuring the cantilever's length, width and resonance frequency (ω_o). The resonance frequency of the cantilever can be measured more accurately that it's thickness. The spring constant for a V-shape cantilever using this technique can be calculated by [57]

$$k = 2\pi^3 l^3 w \sqrt{\frac{\rho^3}{E}} (\omega_o)^3 \quad . \tag{3.3}$$

The Purdue AFMs use a variety of different manufactured cantilevers. However, ThermoMicroscopes Ultralevers^{TM} have been found perform well for EFM measurements. [42] Ultralevers are constructed from doped Si, making them highly conductive. However, their tips have a thin oxide layer that prevents current from flowing through the tip. A typical Ultralever is shown in Fig. 3.17. Typical parameters for the Ultralevers are displayed in Table 3.1. Using Ultralevers eliminates the difficult process of making conducting tips by evaporations of conducting materials onto the cantilever.

3.7 Electrostatic Feedback Control System

The EFM system developed at Purdue University uses two separate feedback systems. As discussed earlier, the feedback controlling the surface topography is maintained using the Nanotec software and electronics. The electrostatic portion of the control system is an analog feedback circuit.

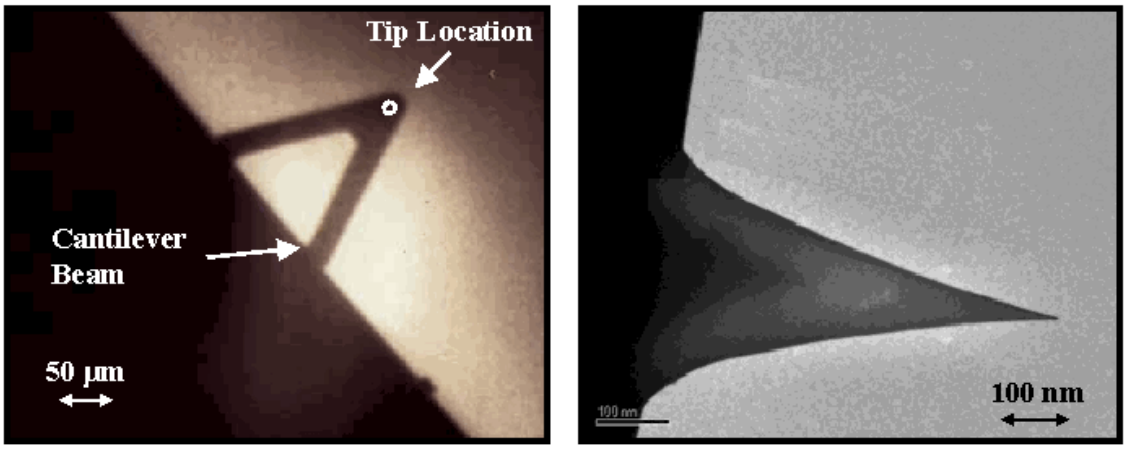

Figure 3.17. a) The cantilever as seen through an optical microscope . b) Transmission electron microscope (TEM) image of cantilever's tip. TEM images courtesy of Elton Graugnard.

Since there are two different feedback systems working during a measurement, the topographic feedback needs to stabilize (settle to the set point value) before the EFM feedback. This ensures a constant tip-sample separation, which is necessary for the EFM measurements. The timing parameters are controlled by both the data acquisition software and configuration of the analog circuit.

Figure 3.18 is a schematic of the analog feedback circuit used to make surface potential measurements. The circuit is based on a proportional integral (PI) control system. [33, 58] An error signal ϵ, the difference between the set point voltage and the output from the EFM lock-in amplifier (the amplitude of ω_1 force component), is generated in the first stage of the circuit. The next stage consists of the P and I components. The P and I elements of the feedback circuit uses the error signal to compute a correction voltage required to eliminate the error signal. The relative effects of the feedback parameters (P and I) on the correction voltage are controlled by the potentiometers α and β. The output for the P and I portions of the circuit are summed together by a summing amplifier. Thus, the output voltage (V_{Tip}) is influenced by a combination of P and I. The analog circuit applies the output voltage

(V_{Tip}) to the cantilever's tip to eliminate the ω_1 component of the force. Under perfect conditions, the correction voltage will have just the right polarity and magnitude to eliminate the error signal.

The Nanotec control system can conduct topographic measurements using digital z-feedback while simultaneously recording an additional signal from another input channel. By sending the V_{Tip} to ADC2 (CH2) of the Nanotec system (Fig. 3.2), the local surface potential is simultaneously recorded while the topographic feedback is engaged.

3.8 Piezotube Hysteresis

The expansion of the piezotube plays an important role in determining quantities such as the force calibration and tip-sample separation. [26] Therefore, it is extremely important to know the z motion of the piezotube accurately.

As discussed earlier, piezotubes expand when a voltage difference is applied to the electrodes. By knowing the coefficient of expansion for a given applied voltage, the distance a piezotube moves can be estimated. Often, the piezotube's expansion coefficient is assumed to be linear.

However, piezotubes do exhibit non-linear behavior known as hysteresis. This behavior is due to coupled capacitance between the electrodes, material properties of the tube and thermal drift. Hysteresis can have a large effect on a piezotube's estimated distance of travel.

To conduct highly accurate AFM work, the hysteresis must be taken into account. By not taking into account the piezotube's non-linear behavior, the tip-sample separation distance and the force calibration can be influenced by uncertainties resulting from inaccurate position measurements. It is therefore advantageous to monitor the piezotube's motion during a measurement.

The hysteresis monitoring technique developed at Purdue is based on a fiberoptic interferometer similar to the one described in an earlier section. This system consists of a mirror, with a gold coating, mounted to the back of the piezotube. The fiber is placed a few hundred microns away using an alignment jig, which is attached to the

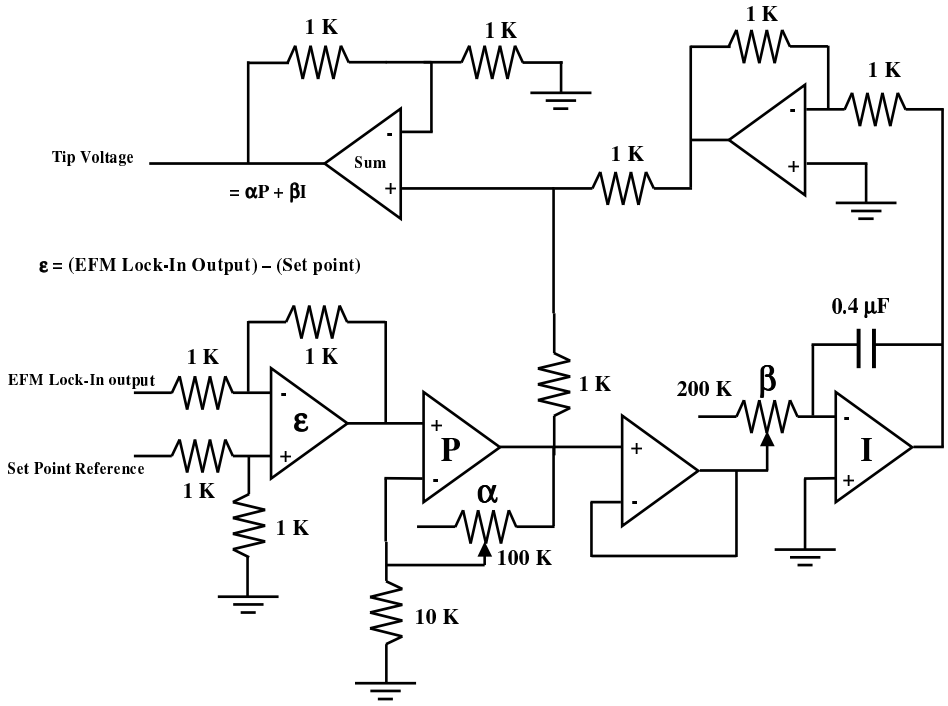

Figure 3.18. Analog feedback circuited used to null the ω_1 component of the electrostatic force. To null the electrostatic signal, the set point is referenced to ground. When the output EFM lock-in $\neq$ ground, the error signal will propagate throughout the circuit and produces a correction voltage that is applied to the tip. This correction voltage will have the necessary magnitude and polarity required to null the electrostatic force acting on the tip; thereby, eliminating the amplitude of the ω_1 force. All of the operational amplifiers are OP-27.

base of the piezotube's holder. The alignment is used to set the fiber-mirror spacing close to an odd multiple of $\frac{\lambda}{8}$.

During peizotube calibration, a voltage ramp is applied to the z element of the piezotube, causing the tube's length to change. The fiber-reflector spacing also changes and causes the intensity to vary at the interferometer's photodetector. The interferometer's intensity (I) is measured as a function of applied piezotube bias voltage. Using a simple model for the interferometer's output intensity, the intensity data ($I(V_{tube})$) is converted to a distance ($D(V_{tube})$).

The observed optical interference is due to multiple reflections between the fiber's end and the reflector. This system is modeled by [47]

$$I = I_o \left(\frac{r_1^2 + \beta^2 - 2r_1\beta\cos\delta}{1 + r_1^2 - 2r_1\beta\cos\delta} \right) \quad . \tag{3.4}$$

r_1 is the reflection coefficient for the fiber's end, (β) is the effective reflection coefficient for the reflector and D is the fiber-reflector separation distance. The phase angle δ is given by

$$\delta = 4\pi D/\lambda \quad . \tag{3.5}$$

Here λ is the wavelength of the light (in this system λ is 1310 nm).

When the fiber is positioned far from the reflector, beam spreading occurs. The beam spreading reduces the amount of light reflected from the gold reflector. This can be treated as an effective reflection coefficient β, which is modeled by

$$\beta = r_2 F(D/a) \quad , \tag{3.6}$$

where

$$F(D/a) = 1/\sqrt{1 + 4\theta D/a + 4\theta^2(D/a)^2} \quad . \tag{3.7}$$

$F(\frac{D}{a})$ is beam spreading function, r_2 is the reflection coefficient of the reflector, a is the fiber's core diameter and θ is the cone angle for the fiber.

Under the right circumstances ($D \gg a$), the interferometer's intensity output can be modeled by

$$I = A\cos\delta + B \quad , \tag{3.8}$$

where

$$A = \frac{I_{max} - I_{min}}{2} \tag{3.9}$$

and

$$B = I_{min} + A \quad . \tag{3.10}$$

A and B can be determined by fitting Eq. 3.8 to the actual intensity data. Figure 3.19 displays the interferometer's intensity output as a function of distance and the fit to the intensity data using Eq. 3.8.

After determining A and B, the distance traversed by the piezotube is calculated using the inverted form of Eq. 3.8:

$$D = \frac{\lambda}{4\pi} \arccos\left(\frac{I - B}{A}\right) \quad . \tag{3.11}$$

Due to the arccos function, $D(V_{tube})$ has a periodicity. This periodicity is removed with the use of an algorithm that adjusted the phase angle in order to make $D(V_{tube})$ linear. (see Appendix C)

The linearized data is used to calibrate the expansion of the piezotube with the applied voltage. A typical calibration plot can be seen in Fig. 3.20. The piezotube is calibrated by fitting $D(V_{tube})$ data with a second ordered polynomial:

$$D = A_0 + A_1 V_{tube} + A_2 V_{tube}^2 \quad . \tag{3.12}$$

From a polynomial fit of the data displayed in Fig. 3.20, A_1 was found to be 14.8 nm/V and A_2 was 0.03 nm/V^2. A_1 is the linear calibration of the piezotube and A_2 is the non-linear correction.

The values of these calibration coefficients are used to relate the voltage applied to the piezotube's expansion. This information can be used to correct the piezo's non-linear behavior. The Nanotec software contains algorithms, based on the parameters calculated above (A_1 and A_2), can correct the piezotube's motion for the hysteresis; thereby, reducing the hysteresis effects in force measurements.

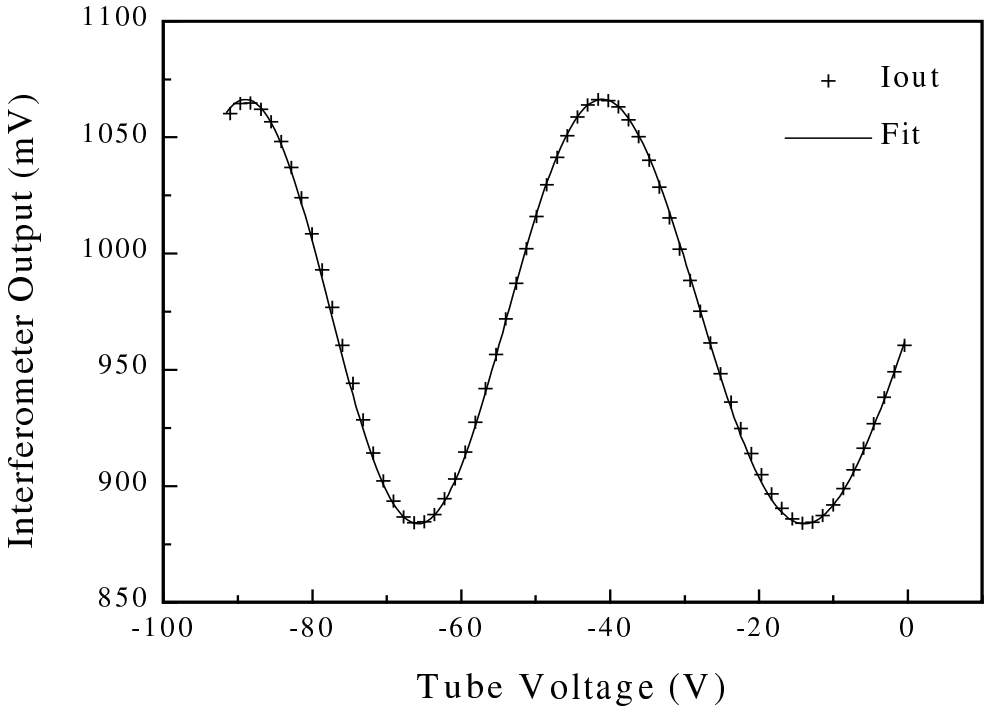

Figure 3.19. Interferometer output recorded as a function of position with a fit from the interference model.

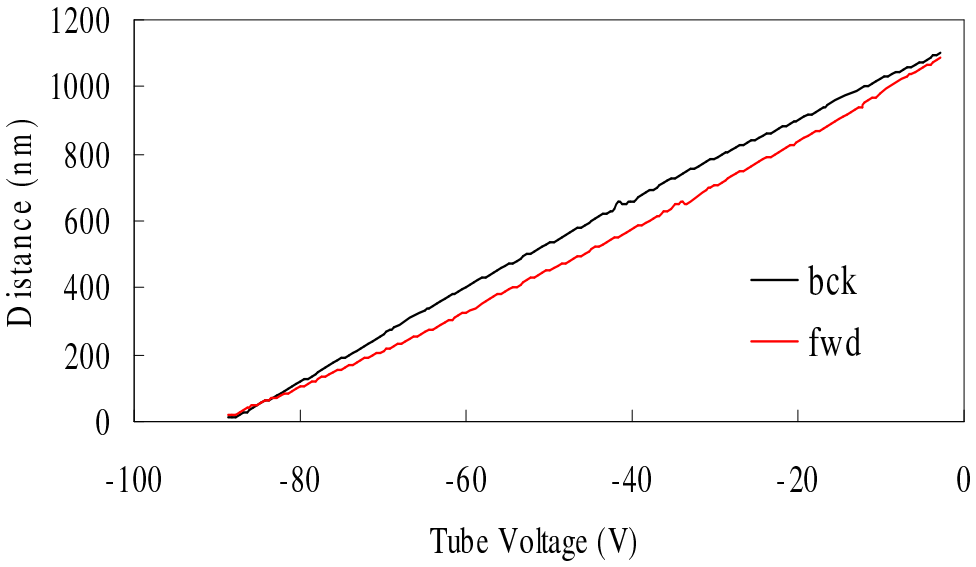

Figure 3.20. Hysteresis curve generated from interferometer intensity data.

4. UNDERSTANDING EFM MEASUREMENTS

After the construction and integration of the UHV AFM into the EFM feedback systems, several studies were conducted to gain a better insight into performing electrostatic measurements using AFM technology. These simple sets of experiments were designed to test the operation of the experiment apparatus and to gain a basic understanding of measuring the electrostatic force on nanometer length scale. The results of these experiments, used to test the EFM principles, are also presented in this Chapter.

4.1 Forces Acting on the AFM Cantilever

As mentioned earlier, the AFM tip can experience a multitude of different forces emanating from the sample's surface. To understand electrostatic measurements,

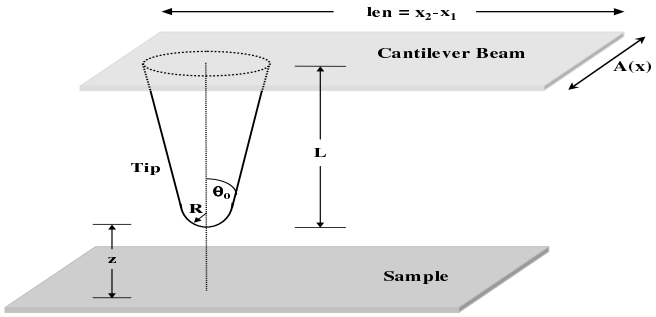

Figure 4.1. Schematic layout of a typical AFM cantilever. AFM Cantilevers can be modeled as cone with a spherical apex attached to a rectangular or triangular beam. The figure displays the parameters used in the calculation of tip-surface interaction forces. z is tip-sample separation. L is the length of the tip. R is the radius of the tip's spherical apex. θ_0 is the cone's half angle. $A(x)$ is a function relating the width of the cantilever to the beam's length.

there needs to be a fundamental familiarity with the forces acting on both the tip and cantilever. An understanding of how the physical parameters of the tip-cantilever system influence the detection of surface forces must also be obtained. In this section several simple models of the dominant surface forces will be discussed. This discussion will help to build a fundamental understanding of the interaction forces measured by the EFM.

Figure 4.1 shows the schematic of a typical AFM cantilever displaying the parameters used for force calculations: R is the tip radius; L is the tip length; θ_0 is the half angle of the tip; z is the separation distance; and $A(x)$ is a function that relates the dependence of the cantilever's width on x. Cantilevers consist of a thin beam of silicon with a conical tip built on its underside. The conical tip has an apex with a diameter on the nanometer length scale (typically $\approx$ 10 nm). The small diameter of the tip's apex allows the tip to measure variation of the surface forces with nanometer lateral resolution.

Forces acting on the conical tip cause the cantilever beam to flex like a spring. By measuring the deflection of the cantilever, it is possible to determine the nature of the forces acting on the tip.

When in close proximity to the sample's surface, several attractive forces act on the tip. However, only two of the forces play a critical role in EFM experiments. Close to the sample's surface ($z \leq 200$ nm) the dominant attractive forces are the van der Waals and the electrostatic forces.

4.1.1 The van der Waals Interaction

The van der Waals interaction originates from dipolar interactions between atoms located in the tip and sample. [26,59] For an AFM tip, this interaction dominates for an extremely short range. [56] The force experienced by the tip, due to the van der Waals interaction, is calculated by a method developed by Hamamker. [60] The van der Waals force can be expressed as [8]

$$F_{vdw} = -\frac{H\pi^2\rho_{tip}\rho_{samp}}{30}\{\frac{(1+\tan^2\theta_0)}{(z+R(1-sin\theta_0))}+\frac{(2R-z)}{z^3}\} \quad , \tag{4.1}$$

where H is the Hamaker constant, ρ_{Tip} and ρ_{samp} are the respective densities of atoms in the tip and sample.

When the tip is oscillating close to the sample' surface ($z \leq 5$ nm), the oscillation will be dampened by the van der Waal's interaction. The AFM can take advantage of the damping force to gather topographic information (non-contact mode).

4.1.2 The Electrostatic Interaction

The electrostatic force has a significantly longer range than the van der Waals interaction. [8,56] This factor is important when considering how to model the total force acting on the tip-cantilever system. There are several different models describing the electrostatic force acting on a conical conducting tip terminated with a spherical apex. [61] However the uniformly charge line model has been found to be a useful model for describing the electrostatic interaction between the tip and sample.

The uniformly charge line model uses the method of image charges to calculate the electrostatic force of a cone over a planar substrate. [61,62] This model replaces the equal-potential surface of the cone by a uniformly charged line with a line density λ located on the z-axis. The linear charge density necessary to generate the equal potential surface of a cone is given by

$$\lambda(\triangle V) = \frac{2\pi\epsilon_0 \triangle V}{Argsh(\tan^{-1}\theta_0)} \quad , \tag{4.2}$$

where θ_0 is the half angle of the cone and $\triangle V$ is the potential difference between the tip and sample.

The interaction of the cone with the substrate can now be approximated by the interaction of a linear charge density positioned over the substrate. The linear charge, λ, experiences a force from its image charge located in the opposite side of substrate's mirror plane. Therefore, the force acting on a cone (approximated by a linear charge density) over a plane is given by

$$F = \frac{\lambda(\triangle V)^2}{4\pi\epsilon_0} \ln(\frac{L}{4z}) \quad . \tag{4.3}$$

where L is the length of the cone and z is the tip-sample separation.

Since the electrostatic force is a long-range interaction (micrometer length scale), both the tip and cantilever beam can interact with the surface. The electrostatic force acting on the cantilever beam can be modeled as a simple parallel plate capacitor system:

$$F_{cap} = -\frac{1}{2}\frac{dC}{dz} \triangle V^2 \quad . \tag{4.4}$$

The capacitance of a cantilever positioned above a conducting substrate is determined by the area of the cantilever's beam (Fig. 4.1) [61]:

$$C_{beam} = \epsilon_0 \int_{x_1}^{x_2} \frac{A(x)dx}{z(x)} \quad , \tag{4.5}$$

where $A(x)$ is a function that describes the width of the cantilever (parallel to the sample) as a function of x, x_1 and x_2 are the coordinates defining the length of the cantilever and $z(x)$ describes x dependence of the cantilever-sample separation. Putting Eq. 4.5 into Eq. 4.4, the force acting on the cantilever beam is

$$F_{Beam} = -\epsilon_0 \frac{1}{2} \int_{x_1}^{x_2} \frac{A(x)dx}{z(x)^2} \triangle V^2 \quad . \tag{4.6}$$

The simple models presented here are useful for understanding the operation of an EFM. In addition, they also help to also explain some of the problems with the current EFM techniques. These shortcomings will be discussed in more detail in later sections.

4.2 Initial Electrostatic Force Detection Based on Force Gradient Measurements

The technique used for measuring both surface topography and electrostatic potential is based on measuring two different time depended forces occurring at distinctly different frequencies (ω_r and ω_1). To gather information on surface morphology, the topographic feedback monitors and regulates the dampening of the ω_r signal (where ω_r is close to the resonance frequency of the cantilever).

However, during an EFM experiment, the electrostatic force acting on the tip is modified by combination of bias voltages applied to the tip. The modified electrostatic force can also dampen the ω_r component of the force. If the damping caused by

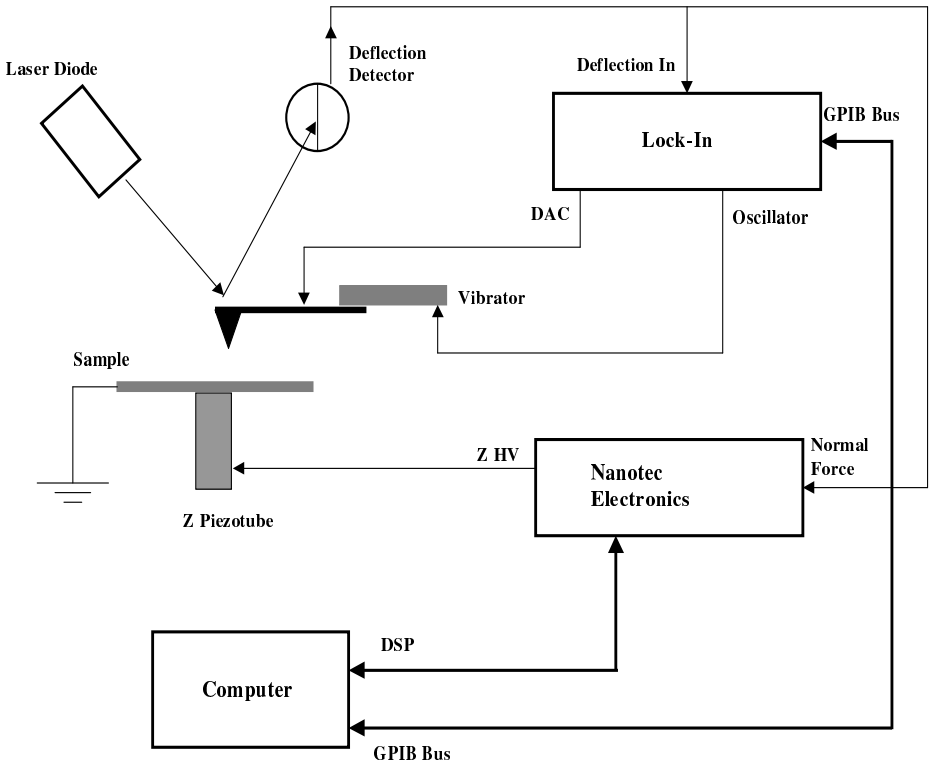

Figure 4.2. Experimental setup used to measure the cantilever's mechanical resonance as a function of tip bias voltage.

the electrostatic force is significant, artifacts will appear in the topographic image. Therefore, it is important to understand how the application of a tip bias voltage will effect the topographic measurements.

To determine the influence of the modified electrostatic force on the damping of the cantilever's resonance frequency, a simple experiment was conducted to measure the cantilever's resonance frequency as a function of tip voltage (V_{Tip}). This information was valuable for determining the influence of electrostatic force on the non-contact topographic images.

Initial attempts to measure the electrostatic interaction were based on a well-established technique for measuring the gradient of the interaction forces acting on the tip. [63] When an oscillating AFM tip is brought in close proximity to the sample's surface, surface forces (such as van der Waals and electrostatic forces) will dampen the cantilever's oscillation; thus, decreasing the resonance frequency of the cantilever. The gradient of the forces acting on the tip is determined by measuring the cantilever's resonance frequency as a function of tip-sample separation.

A variant of this technique was used to probe the electrostatic interaction. Unlike the force gradient method mentioned above where $\frac{dF}{dz}$ is measured as a function of z, this technique measures $\frac{dF}{dz}$ as a function of applied tip bias voltage (V_{Tip}) at a fixed tip-sample separation.

By treating the cantilever as a simple harmonic oscillator, perturbations of the cantilever's resonance frequency can be related to a voltage dependent interaction force $F(\triangle V)_{inter}$ (where $\triangle V$ is the tip-sample potential difference: $\triangle V = V_{Tip} - V_s$).

The equation of motion for an oscillating cantilever can be expressed as [63]

$$m\left(\frac{d^2z}{dt^2}\right) + \gamma\left(\frac{dz}{dt}\right) - k(z - z_0) + F(\triangle V)_{inter} = F_d \cos\omega t \quad . \tag{4.7}$$

Here, $F_d cos\omega t$ is the driving force produced by a piezoelectric vibrator. Approximating the interaction force by a linear expansion about z_0 gives

$$F_{inter} = F(\triangle V)_{inter}(z_0) + \left(\frac{\partial F(\triangle V)_{inter}}{\partial z}\right)_{z_0}(z - z_0) + .. \quad . \tag{4.8}$$

Using the expansion of the interaction force, Eq. 4.7 becomes

$$m\left(\frac{d^2z}{dt^2}\right) + \gamma\left(\frac{dz}{dt}\right) - k_{eff}(z - z_0) = F_d \cos\omega t + Const \quad , \tag{4.9}$$

where

$$k_{eff} = k - \left(\frac{\partial F(\triangle V)_{inter}}{\partial z}\right)_{z_0} \quad . \tag{4.10}$$

Eq. 4.9 is solved with a solution of the form:

$$z(t) = Ae^{-i\omega t} \quad . \tag{4.11}$$

From this solution, the amplitude of the cantilever's oscillation is given by

$$A(\omega) = \frac{A_0}{[\sqrt{(\omega^2 - \omega(z_0)^2)^2 + (\gamma\omega/m)^2}]} \quad , \tag{4.12}$$

where

$$\omega_0(z)^2 = k_{eff}/m \quad . \tag{4.13}$$

When the interaction force is zero, the resonance frequency is

$$\omega_0 = k/m \quad . \tag{4.14}$$

Substituting Eq. 4.13 and Eq. 4.14 into Eq. 4.10, the resonance frequency as a function of position is given by

$$\omega_0(z, \triangle V) = \omega_0 \sqrt{1 - \frac{1}{k}\left(\frac{\partial F(\triangle V)_{inter}}{\partial z}\right)} \quad . \tag{4.15}$$

Eq. 4.15 relates the gradient of the interaction forces to a shift in the resonance frequency.

An experiment based on Eq. 4.15 was implemented to determine how the electrostatic force affected the dampened resonance frequency of an AFM cantilever. During this experiment, the resonance frequency of the cantilever was measured as a function of applied tip voltage (V_{Tip}).

Figure 4.2 displays the experiment configuration used to detect the dampening of the cantilever's resonance frequency as a function of applied tip bias. The experiment was conducted with a homebuilt AFM with a force detector based on an optical beam bounce design. [26] The AFM was housed in a low vacuum system. All measurements were made in vacuum at a pressure of 20 mTorr; thus, removing any significant damping due to an ambient atmosphere.

For implementation of force gradient method, a cantilever was vibrated over a conducting substrate at a fixed distance of z (typically $\leq$ 200 nm). The cantilever's motion was detected with the AFM's force detector. The output from the force sensor was sent to the Nanotec electronics and a phase sensitive detector (lock-in amplifier in Fig. 4.2).

To produce an electrostatic interaction between the tip and substrate, electrical connections were made to both the cantilever's tip and a conducting sample of gold. This arrangement allowed for a different configuration for applying voltages to either the tip or the sample. The tip-sample potential difference was modified by applying a bias voltage to the tip. The bias voltage originated from a digital to analog converter (DAC). Incremental bias voltage steps (dV_{Tip}) were applied to the tip while the resonance frequency of the cantilever was measured for each voltage step.

The resonance frequency of the cantilever was determined by measuring the amplitude of the cantilever's oscillation as a function of frequency using the lock-in amplifier's oscillator. The frequency of vibration (ω) was ramped from a starting frequency (ω_i) to a final frequency (ω_f) about the resonance frequency of the cantilever (ω_0). For each frequency step, the amplitude of the cantilever oscillation was measured with a phase sensitive detector referenced to the frequency of vibration.

Typical resonance curves of the AFM cantilever used for these measurements are shown in Fig. 4.3. A non-linear fit algorithm based on Eq. 4.12 was used to fit each curve and precisely determine the resonance frequency.

The experiment was controlled by a general-purpose interface bus (GPIB) controller. GPIB software (see Appendix D) controlled the voltage step applied to the tip, the frequency used to drive the cantilever, and the measurement of the cantilever's amplitude of oscillation (via the EGG 7280 Lock-In amplifier). The GPIB code ran on a 233 MHz Pentium PC independently of the Nanotec control system.

The cantilever's resonance frequency was measured as a function of V_{Tip} for several different tip-sample separations. The tip-sample separation (z) was determined by measuring the deflection of the cantilever as a function of sample displacement as the sample was brought into contact with the tip.

To measure the cantilever deflection as a function of sample displacement, the sample is moved towards the tip from an initial position. When the initial tip-sample separation is large (usually the starting position), the interaction forces are too weak to deflect the cantilever. As the tip-sample separation decreases, the tip jumps into

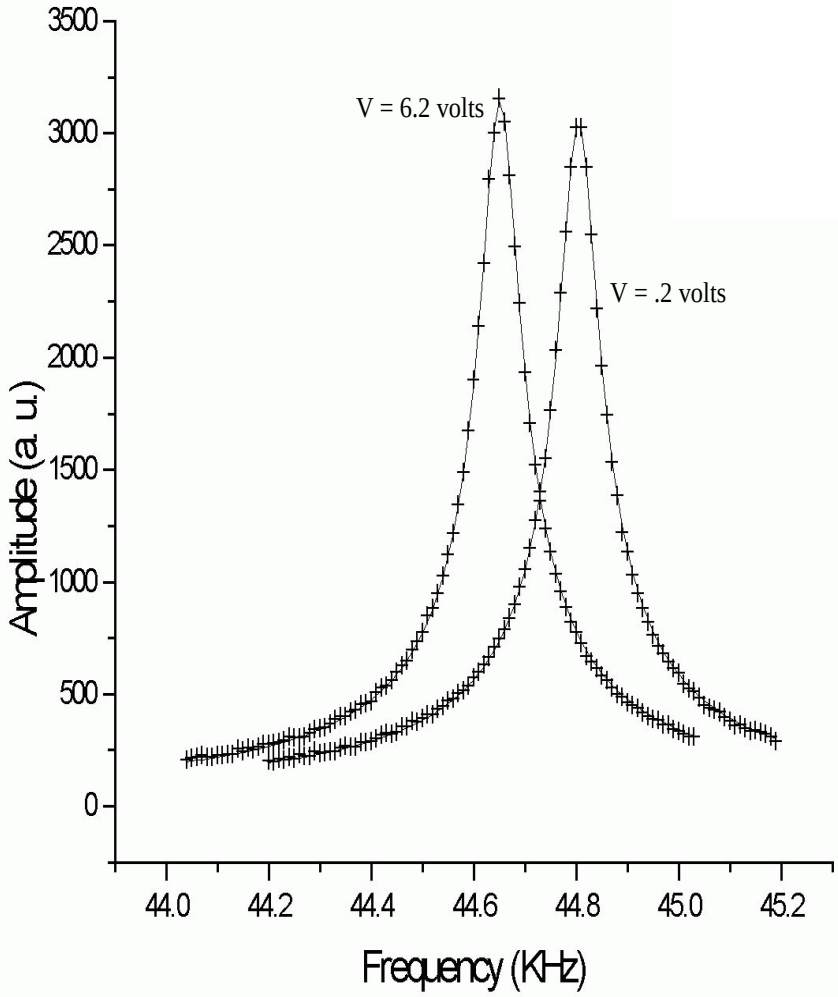

Figure 4.3. Typical measured resonance curves for different applied tip voltages. The data was acquired using cantilevers with a nominal spring constant of 0.24 N/m. The resonance frequency for each curve was determined by a non-linear fit based on Eq. 4.12.

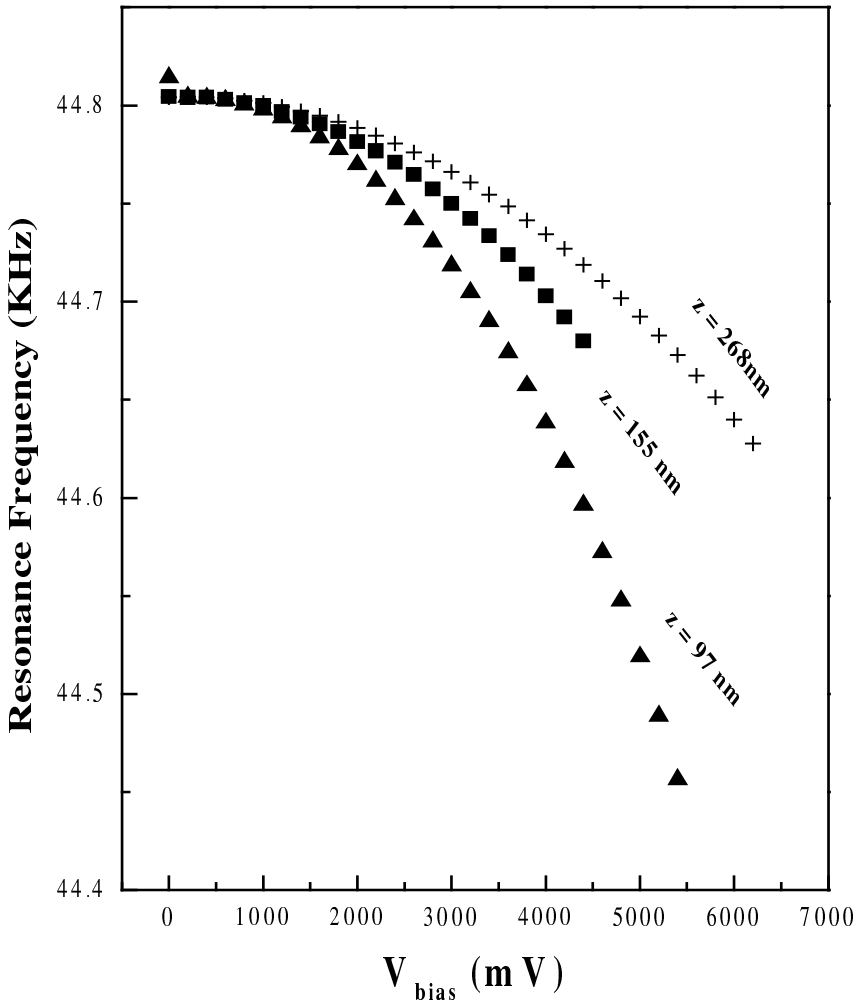

Figure 4.4. ω_0 measured as a function of tip voltage for several different fixed tip-sample separation distances. The data was acquired using cantilevers with a nominal spring constant of 0.24 N/m.

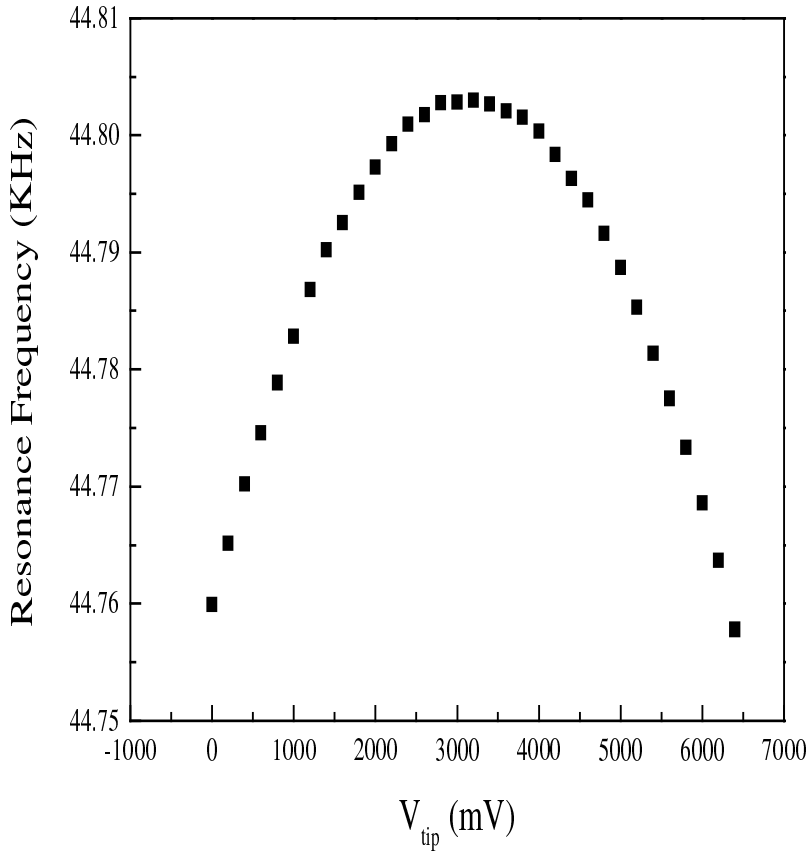

Figure 4.5. ω_0 measured as a function of tip voltage with a sample held at a potential of 3.0 V. The data was acquired using cantilevers with a nominal spring constant of 0.24 N/m.

contact with the sample (deflects towards the sample). This occurs at the point where surface forces overwhelm the restoring force of the cantilever. The distance from the sample's starting position to the jump to contact point is an initial estimate of the tip-sample separation (z_1). However, a better estimate can be achieved by taking into account the amount of distance that the cantilever moved (in the $-z$ direction) when jumping into contact with the sample's surface (z_2). z_2 is measured by moving the sample past the jump to contact point until the cantilever returns to its unperturbed (non-deflected) position. The distance from the initial starting position (along the z-axis) to the position where the cantilever is not deflected is the tip-sample separation distance ($z = z_1 + z_2$). These measurements were made using the Nanotec control system.

$\omega_0 \mid_{z_{fixed}}$ measured as a function of tip voltage (V_{tip}) for three different tip-sample separation distances above the grounded substrate ($V_S = 0$ V) are plotted in Fig. 4.4. The data indicates that as the potential difference between the tip and substrate increase, so does the damping of the cantilever's oscillation (lower resonance frequency). However, the resonance damping does not become significant until approximately 2.0 V. This is significant because for typical EFM experiments, the voltages of ≤ 1.0 V are typically used. Therefore, modifications to the tip-sample potential ≤ 1.0 V will not perturb the mechanical vibration of the cantilever.

Another experiment was conducted to determine if it was possible to measure the sample's electrostatic potential with this force gradient technique. The experimental set-up varied slightly from the set-up used for the earlier experiment. However, for this experiment an offset voltage was applied to the sample's surface ($V_S = 3.0$ V offset). The same technique used for resonance shift detection was employed for this experiment.

Fig. 4.5 is a plot of $\omega_0 \mid_{z_{fixed}}$ as a function of tip voltage, where the sample's potential was modified by an additional bias voltage. The data shows that as the potential difference between the tip and sample is eliminated (null of the electrostatic field), resonance shift returns to its original value. For this case, the sample voltage

was set to 3.0 V and the unperturbed resonance frequency was 44.8 kHz. This simple experiment showed that the electrostatic force could be eliminated when using a conducting tip connected to a controllable bias voltage.

The expression of the electrostatic force acting on a tip above a conducting plane, discussed in earlier (Eq. 4.3), was used to model the data displayed in Fig. 4.4. In addition to the forces acting on the tip, the interaction of the cantilever beam was also included for the modeling. The cantilever-sample system was modeled as a parallel plate capacitor. The total force acting in the cantilever is given by

$$F = -\frac{\lambda^2(V_{Tip})}{4\pi\epsilon_0}\ln(\frac{L}{4z}) - \frac{\epsilon_0 A_{beam} V_{Tip}^2}{2(L+z)^2} \quad , \tag{4.16}$$

where, A_{beam} is the area of the cantilever interacting with the substrate, L is the length of the tip, λ is the linear charge density given by Eq. 4.2, z is the tip-sample separation and $\triangle V = V_{Tip}$ since $V_S = 0$.

During the measurement, the electrostatic force pulls the cantilever towards the surface, decreasing the tip-sample separation. This effect is taken into account by calculating (using Eq. 4.16) the decrease in tip-sample separation (z) due to the total electrostatic force acting on the tip-cantilever system.

The decrease of resonance frequency is modeled by calculating the $\frac{dF}{dz}$ as a function of V_{Tip} (taking into account the decrease in z due to static attraction). The gradient of the interaction is given by differentiating Eq. 4.16 with respect to z:

$$\frac{dF}{dz} = \frac{\lambda^2(V_{Tip})}{4\pi\epsilon_0}\frac{1}{z^2} + \frac{\epsilon_0 A_{beam} V_{Tip}^2}{(L+z)^3} \quad . \tag{4.17}$$

Figure 4.6 displays the actual data taken at tip sample separation of 97 nm and the fit of Eq. 4.17. Nominal values of the spring constant and tip length were used for the fit calculations (0.24 N/m, 3 μm respectively). A_{beam} was estimated to be 1200 μm^2 corresponding to a 40 μm diameter region centered over the apex of the tip. The simple model fits the data reasonably well, given the large variations for the values of the spring constant and tip length.

These measurements have shown no significant alteration of the cantilever's resonance frequency for low tip bias voltages. They also demonstrate another possible

technique for detecting the electrostatic surface potential. However, for most problems under investigation, millivolt sensitivity is required for low bias voltages. The measurements indicated that this technique lacks the required sensitivity for low bias voltages.

4.3 Imaging Variations of the Electrostatic Force as a Function of Position

Initially high-resolution EFM (without electrostatic null feedback) images where made of several test structures. These test structures offered useful insight on interpreting EFM images and the effects of scanning parameters.

Figure 4.7 displays the configuration of the instrumentation needed to acquire both topographic and electrostatic force ($A_{\omega_1}(x, y)$) data simultaneously. As mentioned previously, the primary control system measures the surface topography in non-contact mode (red lock-in amplifier in Fig. 4.7). The control system moves the tip along the surface, while determining the topographic height at each position. At each position, the control system simultaneously measures the EFM Signal (blue lock-in amplifier in Fig. 4.7).

To make an EFM image, the ω_1 component of the detected force signal is measured as a function of position during the topographic scan while the tip is held at a fixed potential. This is accomplished by connecting the arbitrary output of the phase-sensitive detector (EFM Lock-In Amplifier in Fig. 4.7) to an additional input channel of the topographic control system. As the tip moves across the surface, variations in local surface potential causes a change in the electrostatic force experienced by the cantilever. These variations are detected by the lock-in amplifier and recorded by the control system.

The first EFM images were made on a uniform polycrystalline gold where the gold's surface potential was modified. These images were used to test the sensitivity of the electrostatic force sensor. All images were acquired using the air AFM described in Chapter 3.

During the scan, the tip-sample separation was held constant as the topographic feedback system measured the surface morphology. While the topographic control

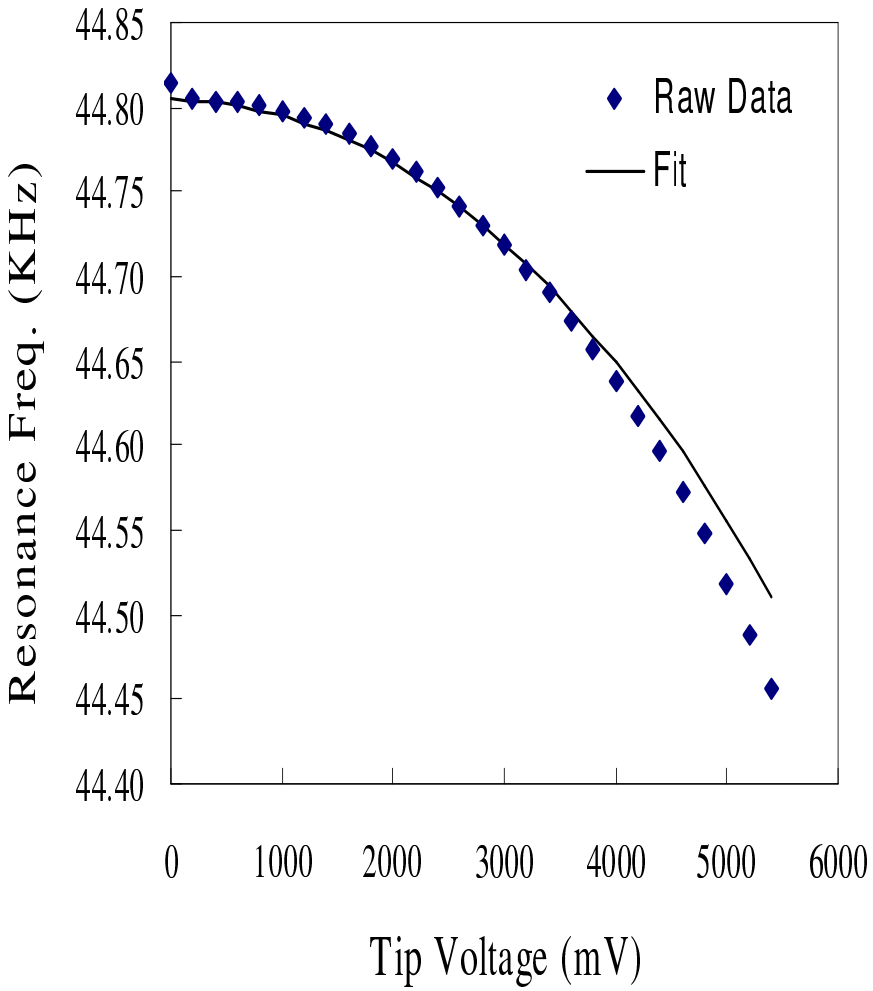

Figure 4.6. Fit to the $\omega_0(V_{Tip})$ data using Eq. 4.17. For this theoretical fit, the uniformly charge line model was used to model the electrostatic force acting on the tip.

system was measuring the surface morphology as a function of position, the sample's surface potential was modified in several incremental steps, producing different values of the electrostatic force. The sample's surface potential was modified by a physical connection to a bias voltage source. The samples surface potential was measured as a function of position (EFM image) using the EFM detection scheme mentioned above.

Measuring the arbitrary transitions between the forces from the acquired EFM image provided insight into the sensitivity of the electrostatic force detector. Since the voltage applied to the sample is known, the output to the electrostatic force detector is calibrated. Using the right selection of experimental parameters, a sensitivity of 20 mV for surface potential detection was obtained with this system.

A second set of EFM test images was made on a series of split electrode structures. These structures were designed to produce lateral variations in topography, as well as, surface potential. The samples consisted of two Au electrodes separated by a single trench.

Theses samples were constructed by a procedure developed at Purdue. [7] To produce the trench, a 4 μm wire was laid across a 1 cm^2 piece of glass. Both ends of the wire were glued down near the edge of the glass surface. After securing the wire, a 10 nm layer of Ti and a 200 nm layer of Au were then deposited on the substrate. After the evaporation, the wire was removed to create two isolated millimeter-sized electrodes separated by 4 μm. Samples used for this study were provided by Elton Graugnard.

Figure 4.8 is an EFM image of the electrode-trench system, with one electrode grounded while the other is biased by a potential of 1.0 V. The scan shows the expected change in the electrostatic force as the tip moves from one electrode to the other. The potential drop across the trench is also evident. The large variation near the edge of the trench is caused by an increase in the surface area of the tip that interacts with the electrode as the tip moves down into the trench. The images show high resolution in detecting the electrostatic variations. Typical parameters used by the EFM images are $\omega_1 \approx 20$ KHz, $V_0 = 5\ V_{pp}$, cantilever spring constant of 2 N/m [42] and a lock-in

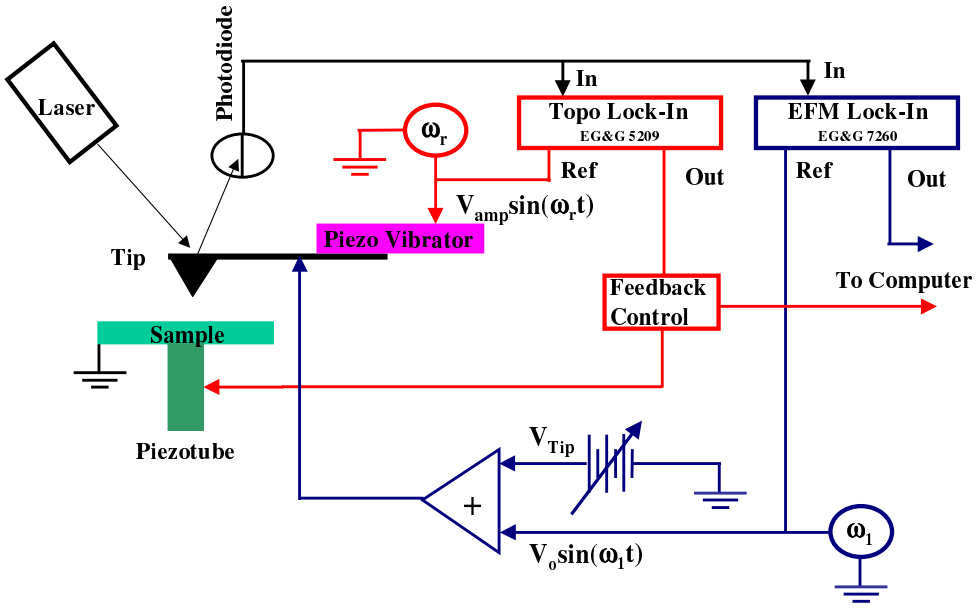

Figure 4.7. Setup used to detect variations in the electrostatic force as a function of position.

time constant of 600 μs. The lock-in amplifier used in the topographic feedback loop was the EG&G 5209 and the lock-in used in the EFM loop was the EG&G 7260.

4.4 Measuring the Electrostatic Surface Potential as a Function of Position

Measuring the actual surface potential ($V_S(x, y)$) as a function of position (KFM images) requires an experimental setup that is similar to the one used for acquiring EFM images. However, for KFM images, an additional feedback system is used to null the electric field in the region between the tip and sample (eliminating ω_1 component of electrostatic force acting on the cantilever).

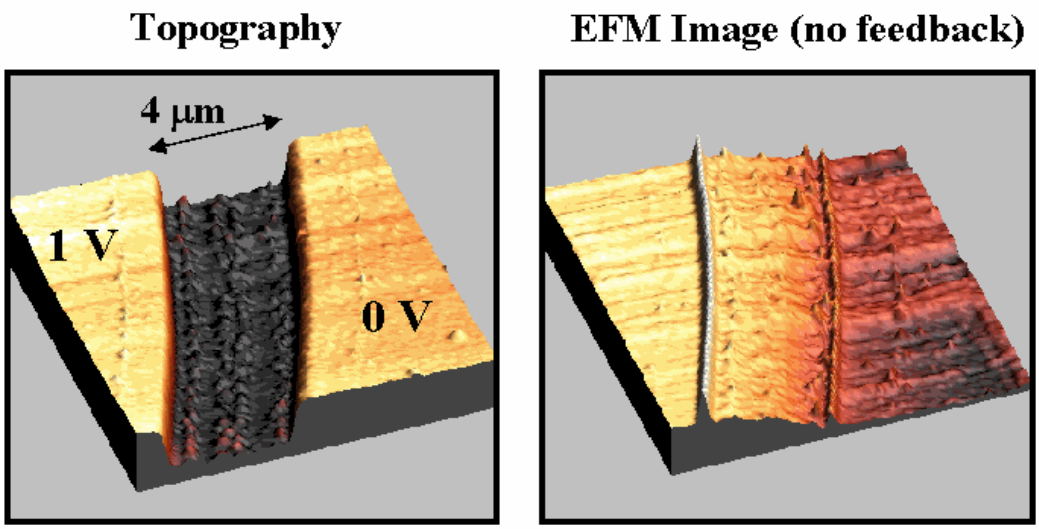

Figure 4.8. Variations of the electrostatic forces measured as a function of position across a split electrode system. One electrode was held at a potential of 1.0 V and the other was grounded.

For this experimental setup, the output of the phases-sensitive detector (blue lock in amplifier in Fig. 4.9) is fed into the KFM feedback circuit (shown in Chapter 3). The output of the feedback circuit is connected to the AFM's tip. The circuit produces a tip bias voltage that eliminates the ω_1 component of the detected force. As the topographic loop measures the surface morphology, the output of the feedback circuit (V_{Tip}) is measured as a function of position. The output the KFM feedback circuit is recorded with an additional input channel used by the control system; thus, producing maps of the sample's electrostatic surface potential and surface topography.

An initial test of the feedback system consisted of connecting a conducting Au sample to a bias voltage source. While both topographic and KFM feedback were engaged, the sample's surface potential was modified. As the sample's potential was modified, the KFM feedback system produced the correct tip voltage required to null the electrostatic force; thereby, verifying the correct operation of the KFM feedback system.

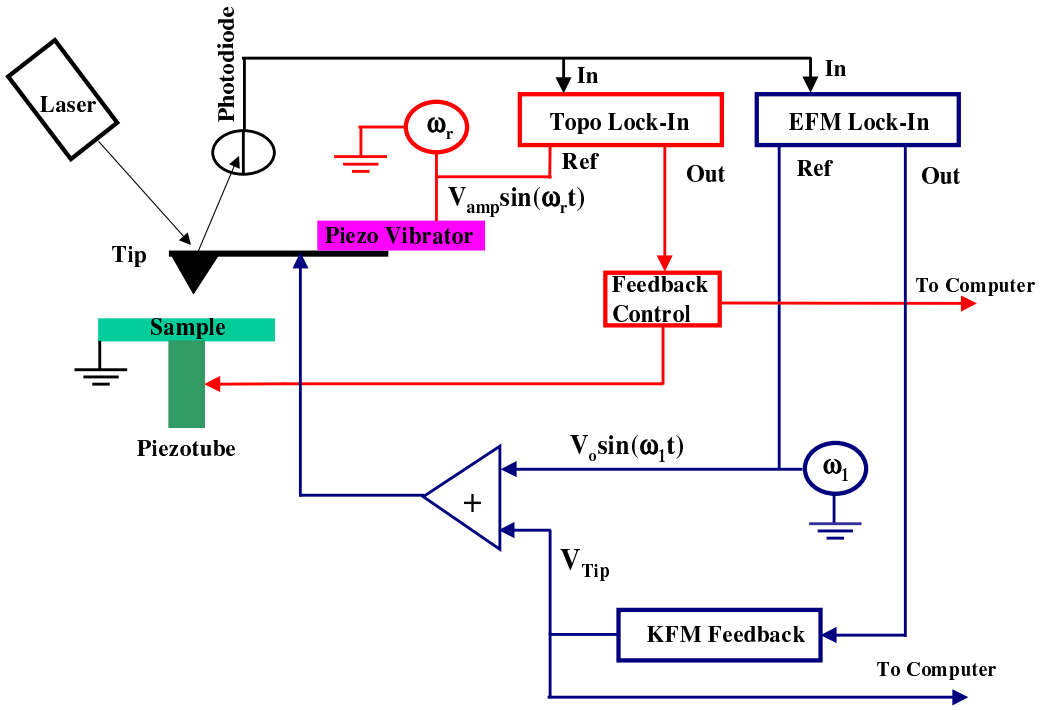

Figure 4.9. Setup used to measure the surface potential as a function of position. The output of the EFM lock-in is used by a feedback circuit to determine the tip voltage required to null the electrostatic field between the tip and sample.

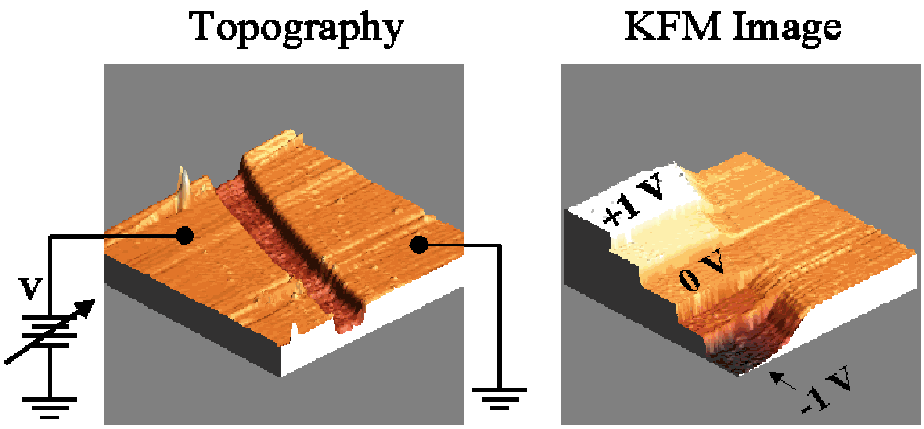

Figure 4.10. KFM image where one electrode's potential is modified by +500 mV increments during the scan.

Similar experiments were conducted on the Au electrodes-trench system. Figure 4.10 shows topographic and surface potential images of the split electrode system. A potential difference was placed across the trench by connecting one electrode to ground, while the other electrode's surface potential was modified by +500 mV increments during the scan. Analysis of the surface potential image indicated that unlike the measurements made over a uniform gold substrate, the surface potential (measured by the KFM feedback system) was 20 - 30 % lower than the actual voltage applied to the biased electrode.

In addition to the effects mentioned above, the KFM images displayed a lower resolution than EFM images. Unlike the EFM image, the KFM image did not display any high-resolution variations in the surface potential (lack of small features in the image). The loss of resolution in the surface potential images is due to the long-range nature of the electrostatic force. This effect is known as convolution. The next several sections will discuss the convolution of the electrostatic force in more detail.

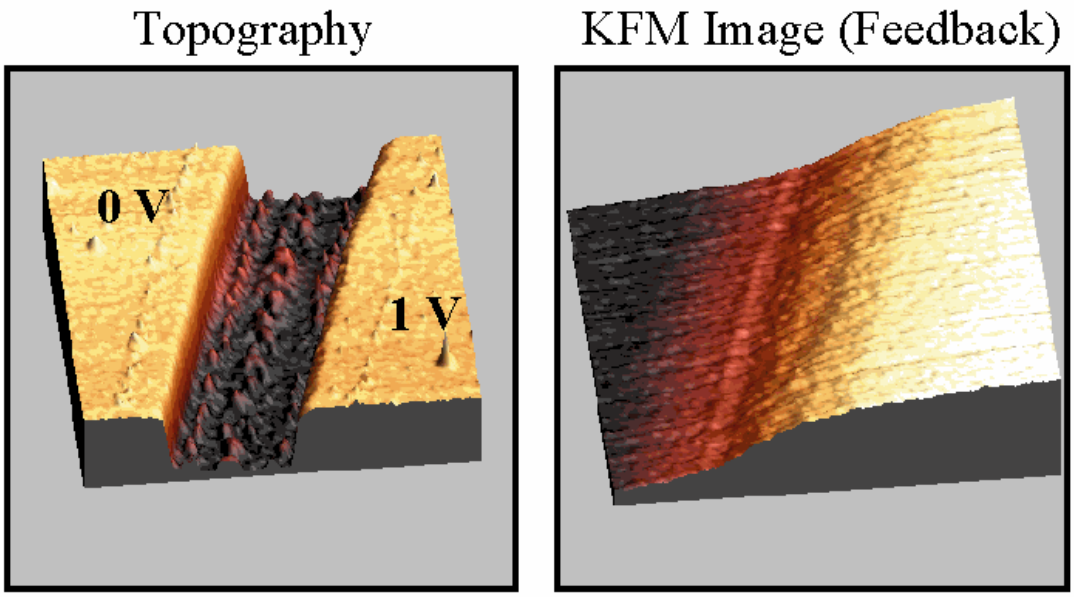

Figure 4.11. KFM images of the split electrode system. The surface potential appears to change before reaching the edge of the electrodes. This is an effect caused by the long-range nature of the electrostatic force.

4.4.1 Effects of Convolution on KFM Images

The effects due to the convolution of the electrostatic force can be seen from the KFM image shown in Fig. 4.11. During the scan, a potential difference of 1.0 V was placed across the split electrode system. However, the measured potential difference obtained from the KFM images showed a potential that was approximately 0.6 V. This discrepancy (the difference between the applied potential drop and the measured potential drop) originates from the long-range nature of the electrostatic interactions. Unlike the van der Waals force, which has a range of 5-20 nm, the electrostatic force can range over several microns.

Because of the long-range nature of the electrostatic interaction, the cantilever beam also experiences a force that is nearly equal to the force experienced by the cantilever's tip (Fig. 4.12). This can been seen by making a comparison between the modeled forces of both the tip and cantilever. The model used to calculate the electrostatic force acting on a conical tip has been discussed earlier (Eq. 4.3). Eq. 4.3 is used to calculate the electrostatic force acting a 3 μm long AFM tip, with a half-angle of 12^0. The force acting on the cantilever beam is estimated by using Eq. 4.4 and treating the beam-sample system as a parallel plate capacitor with a plate diameter of 40 μm (the size of the cantilever's apex where the base of the tip is connected) and a plate separation of 3 μm (the length of the tip). The forces are calculated for a 1.0 V potential difference between the tip (cantilever) and sample.

Figure 4.13 shows a comparison of the calculated forces acting on the tip and cantilever beam. The electrostatic force for each system has been plotted as a function of separation distance in nanometers. It clearly demonstrated that for large separations, the electrostatic force acting on the cantilever is greater than the force acting on the tip. Therefore, the total force acting on the tip-cantilever system is a weighted average of the forces due to the individual capacitance of tip and cantilever.

Since the tip has an end radius of $\approx$ 10 nm, it has a much higher resolution for detecting lateral variations of the electrostatic force compared to the cantilever. However, the cantilever is much larger than the tip, it interacts with a larger area of

the underlying substrate; thus, lowering lateral resolution for measuring electrostatic variations.

When the feedback system attempts to minimize the electrostatic forces between the tip and a small submicron feature with a surface potential V_{S1}, the potential applied to the cantilever will not be V_{S1}. It will be a modified voltage that will include the interaction of the cantilever with the background substrate. Thus, the actual potential of the feature under investigation is convoluted with the background on which it is resting.

The effects of convolution have been seen in all KFM images acquired with the Purdue instrumentation, as well as, additional observations reported in the literature. [64–66] From Fig. 4.14, the effects of convolution are seen as a premature change in the surface potential near the edge of each electrode. For the system in Fig. 4.14, a 1.0 V potential difference was applied across the electrodes. However, the feedback system only measured a potential difference of approximately 0.6 V.

In reality, the electrodes are equipotential surfaces where the surface potential is uniform across the entire electrode (including near the edge of the trench). These effects are due to the location of the tip on the cantilever beam. If the tip is located far from the edge of the cantilever, the electrostatic interaction between a distant region of the cantilever with the substrate can convolute the measurements at the location of the tip. As the tip moved across the image of Fig. 4.14, from the first to the second electrode, the cantilever interacted with the second electrode while the tip was still positioned over the first electrode. The premature interaction with the distant electrode caused the feedback to apply a voltage that was not representative of the true potential of first electrode.

4.4.2 Modeling the Convolution of a Split Electrode System

This concept can be demonstrated by modeling null voltage as a function of lateral tip position for a split electrode system (see Appendix E). This model represents a cross-sectional slice of the KFM image in Fig. 4.14. The cantilever-sample system is modeled as a simple parallel plate capacitor traveling across two electrodes separated by a distance of 4 μm (Fig. 4.15).

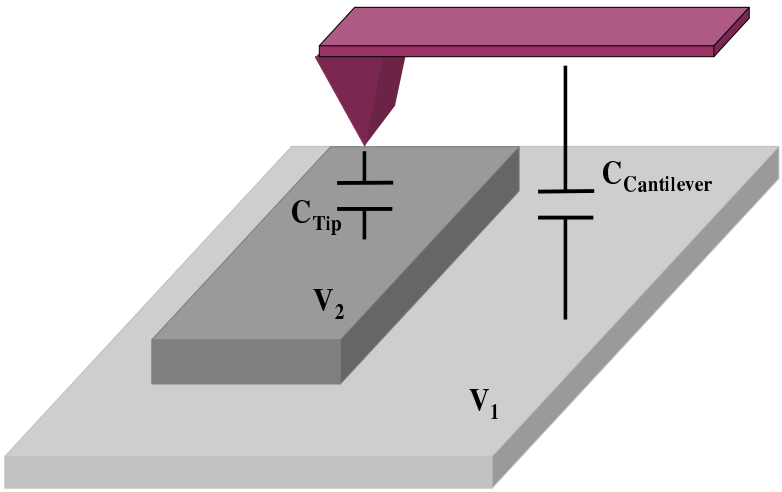

Figure 4.12. Typical cantilever beams have dimensions that are much larger than the length of the AFM tip. Thus, a parallel plate capacitor is formed where the beam interacts with a large area of the substrate. The force acting on the beam can be comparable to the force acting on the AFM tip.

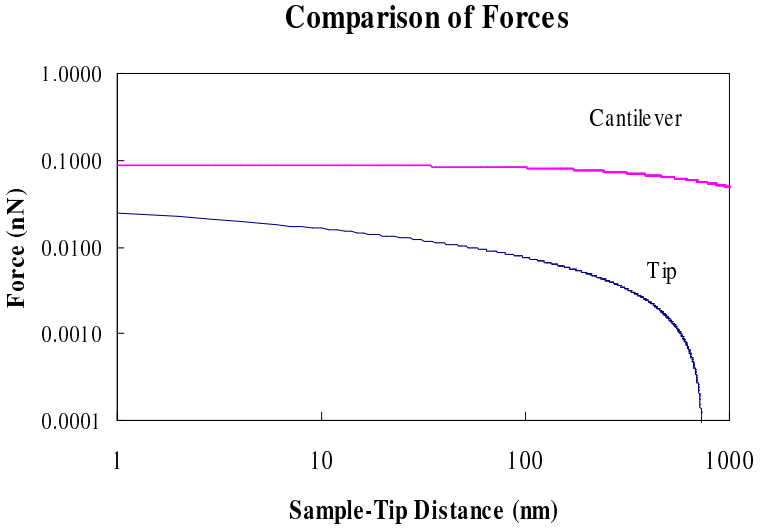

Figure 4.13. Comparison between the tip-sample and cantilever-sample electrostatic interactions. The force acting on a AFM tip was calculated using Eq. 4.3 and the force acting on the cantilever beam was calculated using Eq. 4.4.

The electrostatic interactions between the tip and sample are ignored for this crude simulation. The cantilever's tip is only used to mark a position along the scan trace where the null voltage (the voltage required to eliminate the ω_1 component of the electrostatic force acting on the cantilever) is recorded. At each point along the scan (moving the cantilever from $x = 0$ to $x = L$, where L is the length of the scan trace), the voltage required to null the electrostatic force was calculated for the location of the cantilever's tip. This simulates the control system's behavior for recording the total electrostatic signal (tip + cantilever) for every topographic acquisition point along the scan trace.

The force acting on the parallel plate capacitors is given by

$$F = -\frac{1}{2}\frac{\epsilon_0}{z^2}(A_1(V_{Tip} - V_1)^2 + A_2(V_{Tip} - V_2)^2) \quad , \tag{4.18}$$

where A_1 and A_2 are the areas of the cantilever beam over electrodes 1 and 2 respectively. The tip voltage required to minimize the electrostatic force ($\frac{dF}{dV_{Tip}}$=0) for this

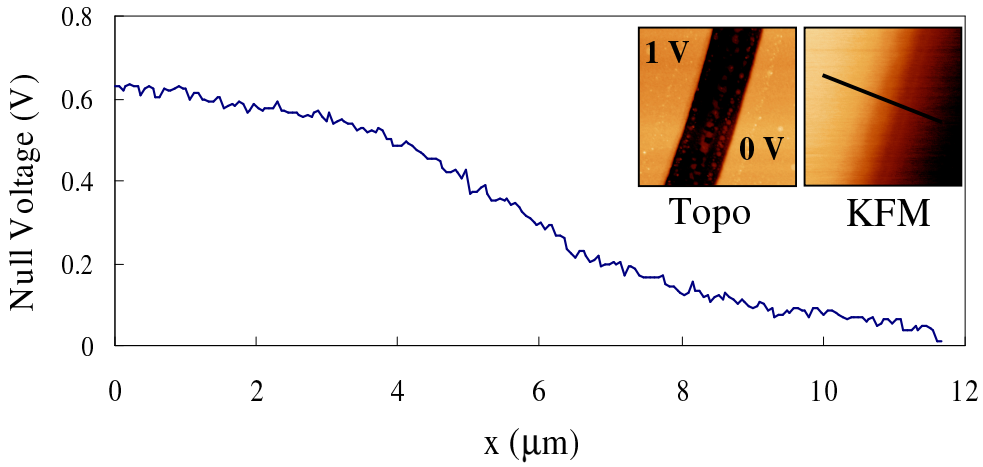

Figure 4.14. Profile of a KFM image (insert) where a 1.0 V potential difference was applied across the trench. The surface potential measured by the feedback system showed a potential difference of only ≈ 0.6 V.

system is given by

$$V_{Tip} = \frac{A_1 V_1 + A_2 V_2}{A_1 + A_2} \quad . \tag{4.19}$$

Figure 4.15 shows the modeled tip potential, based on Eq. 4.19, needed to eliminate the electrostatic force acting on the cantilever as a function of tip position. Initially, the electrostatic force acting on the cantilever is primarily due to the interaction with electrode #1, since the cantilever is positioned entirely over electrode #1. Therefore, the tip voltage require to null the electrostatic force is the electrode #1 surface potential (1.0 V).

As the cantilever moves across the system, the area of the cantilever covering each electrode changes with position. Thus, the total force acting on the cantilever becomes dependent on both electrodes. It is evident from Fig. 4.15, that as the cantilever's tip approaches the trench, electrode #2 begins to influence the potential required to minimize the total force acting on the cantilever. Therefore, the calculated null potential is lowered as the tip approaches the edge of electrode #1. This shows a consistent effect describing the discrepancy between the simulated and actual potential near the edge of the first electrode (Fig. 4.14).

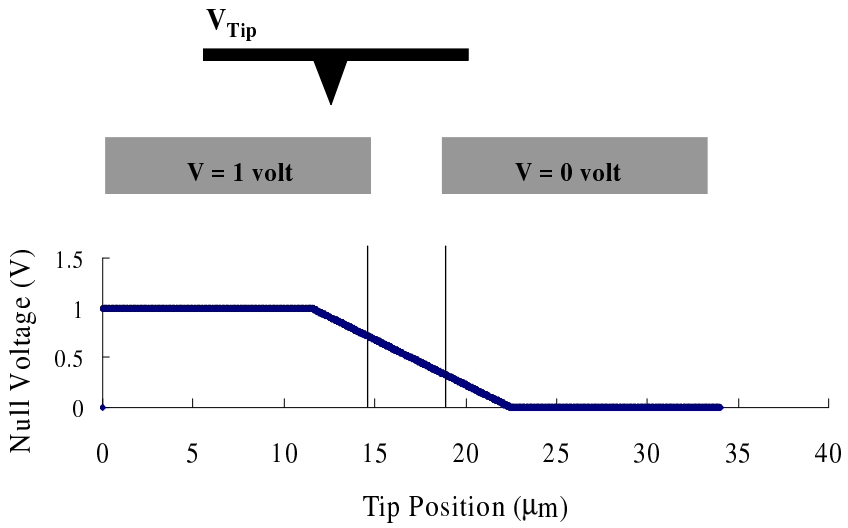

Figure 4.15. Model used for explaining the premature change of the null voltage near the edge of a large electrode. The cantilever beam is represented as one electrode in a parallel plate capacitor. Near the edge of one electrode, the cantilever beam can interact with the other electrode. Thus, the null voltage recorded at the tip's position will be influenced by both electrodes. This simulation displays the same behavior near the trench as the profile seen in Fig. 4.14.

The above model demonstrated how various parameters, such as tip length and shape, affected the convolution of KFM images. KFM images were made using several cantilevers that possessed a variety of different physical properties, such as cantilever dimensions and location of the tip's base on the cantilever beam. Cross-sections images of KFM images were used to judge the quality of the tip performance.

The best cantilever for KFM imaging would be a very long and slender tip mounted to a narrow cantilever beam. [64] Using a tip, with length that is equivalent to the size of the cantilever, places the cantilever beam far from the sample surface. Therefore, only the electrostatic interaction with the tip's apex dominates. This would increase the lateral resolution of the KFM images while decreasing the effects caused by the electrostatic interaction of the cantilever.

Recently, advances in mounting carbon onto AFM cantilevers have emerged as a powerful technique for producing long tips with high aspect ratios. The structural characteristics of nanotubes are well suited for the use as KFM probes (long and slender). Arnason *et al.* have shown the total elimination of the convolution using carbon nanotube tips. [67] However, mounting a nanotube is an extremely difficult process and is prone to low tip yield.

In addition to advances in AFM tip design, software corrections (image processing) can be made to the KFM images that will eliminate the effects of convolution. [65,66] These image corrections use the tip's geometry to determine how various parts of the tip-cantilever system influence lateral resolution for detecting potential variations. The data in the image is then corrected to compensate for the influence of the cantilever. Eliminating effects due to convolution using image processing techniques is difficult. Requiring detailed knowledge of the physical properties of the cantilever used for the experiment.

A simpler solution to eliminate the convolution is to position the entire tip over equipotential surface that has dimensions that are much larger than the beam of the cantilever. In this system, the tip and cantilever interact with the same equipotential surface; thus, eliminating the averaging of the electrostatic force across many

electrodes at different potentials. This requires samples that have large homogenous regions. The drawback to this technique is the loss of high-resolution potential maps of the sample's surface. However, the approach has demonstrated high precision in measuring the surface potential of samples with physical dimensions that are much larger than the cantilever.

4.5 Making Accurate Electrostatic Surface Potential Measurements

As mentioned in the last section, a simple way to measure the surface potential independent from convolution effects, is to place the cantilever over a homogenous region that has physical dimensions that are much larger than the cantilever beam. In this situation, there are only two electrodes: the entire cantilever, including tip, and the sample. In most cases, it is a relatively simple process to construct samples that meet the criteria mentioned above.

To measure the surface potential of a sample using this simple technique, an instrumentation setup similar to the one that makes EFM images is used (no null feedback). These measurements are made using heavily doped silicon tips with a nominal spring constant of 2.0 N/m. [42] These tips were found to have excellent characteristics for both detecting the electrostatics force and for imaging the sample surface. The electrostatic surface potential (V_S) measurements are based on the standard non-contact force detection technique initially described in Chapter 2. The tip is held at a fixed distance of approximately 100 nm above the sample using a non-contact topographic feedback system (red loop in Fig. 4.7). The topographic feedback system controls the separation by monitoring and maintaining a specific mechanical vibration of the cantilever (ω_r) near its resonance frequency.

The electrostatic force acting on the tip is measured by placing a controlled combination of a dc bias voltage (V_{Tip}) and a time varying dither voltage ($V_0 \sin \omega_1 t$), where ω_1 is at a different frequency than ω_r, on the AFM tip. The modified potential difference between the tip and sample produces an electrostatic force that has a frequency component ω_1. The ω_1 component of the force is detected using phase sensitive detection. By varying the dc bias voltage applied to the tip (V_{Tip}), the

sample's surface potential is measured by determining the dc tip voltage (V_{Tip}) required to minimize the magnitude of the ω_1 component of the electrostatic force. For this type of measurement, the tip bias voltage originates from a DAC controlled by the software (see Appendix F). To make the measurements of the sample's surface potential, the software modifies the tip bias voltage in incremental steps dV_{Tip} while measuring the amplitude of the ω_1 component (Eq. 2.14) for each voltage step. For typical measurements, ω_1 is $\simeq$ 80 kHz and V_0 is $\approx$ 5.0 V_{PP}.

Figure 4.16 shows a typical plot of the measured ω_1 component of force as a function of tip bias voltage. The minimization of the ω_1 component occurs when the tip is at the same dc bias voltage as the surface of the sample. Making the potential drop across the sample is zero. This is indicated as a minimum in the plotted curve (null point).

Several tests were conducted to verify that the dc bias needed to minimize the electrostatic force was independent of parameters such as the magnitude of the dither voltage, driving frequency ω_1 and tip-sample separation (small compared to the cantilever's dimensions).

One simple experiment was designed to test the sensitivity of this technique by measuring the modified surface potential of a polycrystalline gold sample. The sample's surface potential was modified by a physical connection to a dc bias voltage source. The sample bias voltage was increased for 0 mV to +200 mV in +50 mV increments. For every increment of the sample bias voltage, the surface potential was measured.

Figure 4.17 shows the plotted EFM curves for each voltage increment. This figure indicates that as the sample bias voltage is increased, the measured relative surface potential also increases by the same amount. Further review of this plot also provides information on the noise limit of the technique. For this particular choice of experimental parameters, such as the value of ω_1, the noise limit of the surface potential measurement was found to be $\pm$10 mV. The relative offset of the gold's surface potential, at a zero sample bias, is due to the work function difference between the Si tip and gold ($\triangle V_{CPD}$).

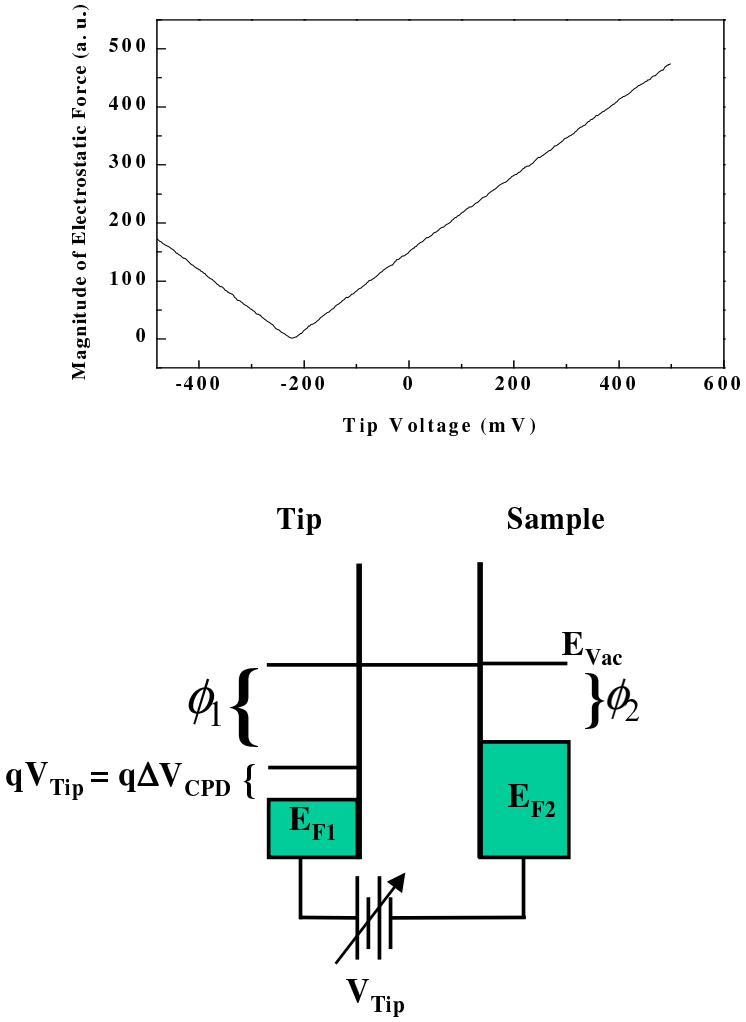

Figure 4.16. The minimum in the magnitude of the electrostatic force ($A_{\omega_1}(V_{Tip})$) from Eq. 2.14) data occurs when the tip has the same electrostatic potential as the surface (in the case of a metal or semiconductor $V_S = \triangle V_{CPD}$). This is the amount of bias voltage required to shift the Fermi level until the E_{Vac} of the tip and sample coincided.

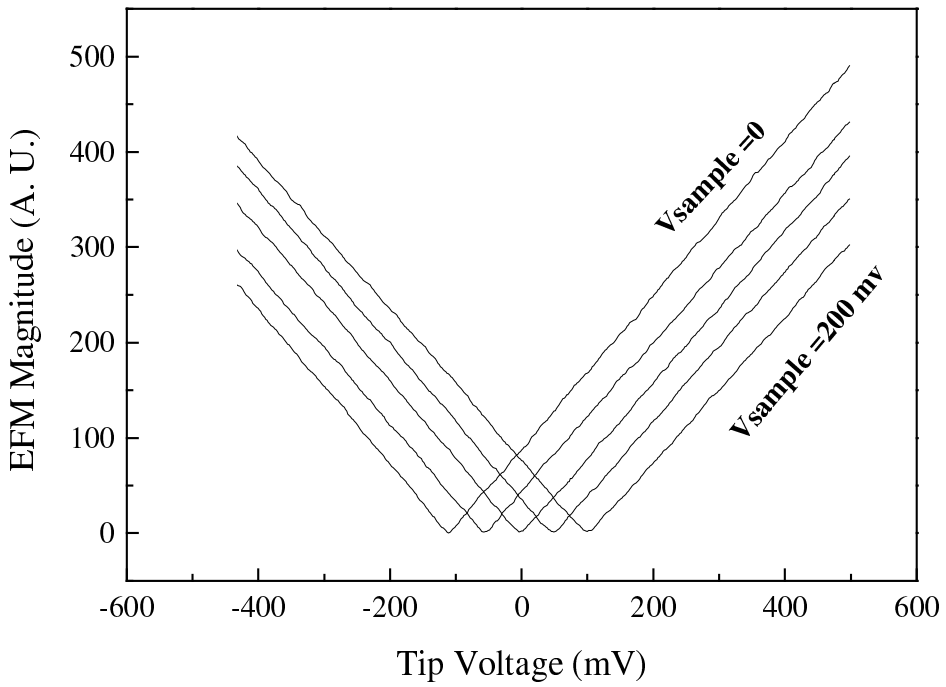

Figure 4.17. Several surface potential measurements of a sample whose surface potential was modified by +50 mV increments. The surface potential of the sample was modified by connection to a dc bias voltage source.

To understand the data shown in Fig. 4.17, it is useful to consider the energy band structure of the tip-sample systems as the sample is modified by the bias voltage. As the sample's bias is increased by +50 mV, the sample's Fermi level decreases by 50 meV. Therefore, the Fermi level of the tip also needs to shift down by an additional 50 meV to eliminate the electrostatic force. This requires a more positive tip bias voltage, which can be seen by the positive +50 mV shift of the null voltage.

After completing this initial experiment, additional experiments were conducted to determine the effects of experimental parameters, such has EFM driving frequency, on the surface potential measurements. Figure 4.18 shows multiple EFM measurements made for different dither frequencies (ω_1). This data indicates no dependence of the

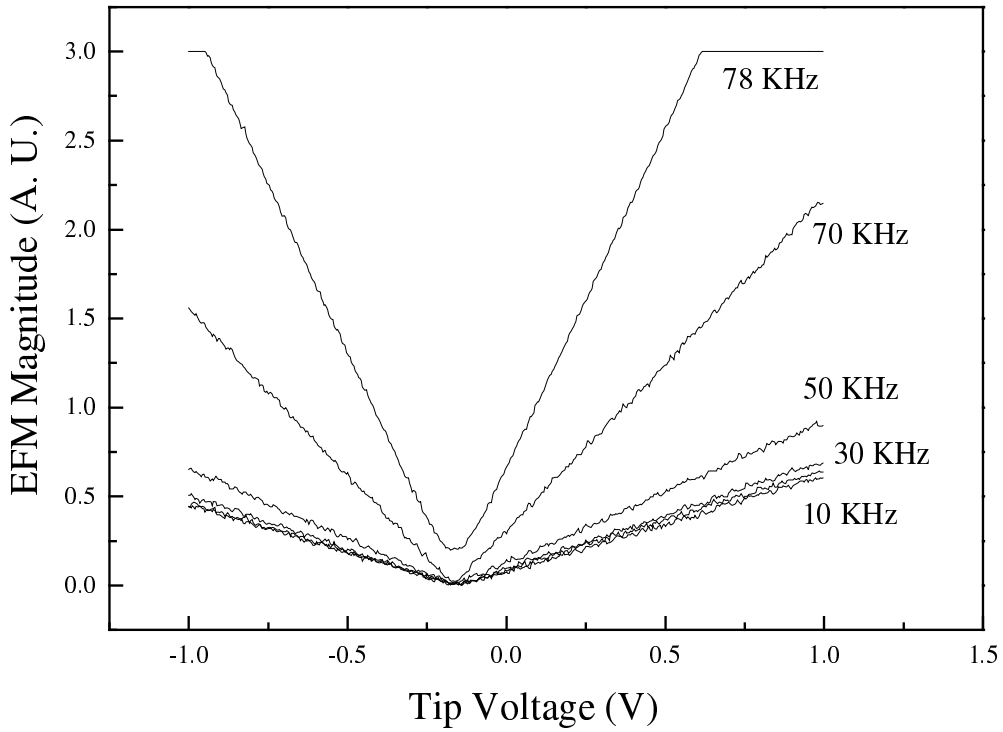

Figure 4.18. Surface potential measurements made for several different frequencies of ω_1.

surface potential on the EFM driving frequency. However, when ω_1 approaches ω_0 ($\leq$ 10 KHz), the signal to noise ratio of the measurements rapidly increases. It is very important not to use values of ω_1 that fall within a range of 10 KHz from ω_r (the topographic signal). This will prevent cross talk between the topographic and electrostatic portions of the measurements.

An additional experiment was conducted to determine the dependence of the surface potential on the tip-sample separation. This determination is extremely important because no two cantilevers have the same exact physical properties, which influence the tip-sample separation. For this study, the surface potential of a bulk gold sample was measured at different topographic set points. Different set points correspond to different tip-sample separation. No significant dependence of the surface potential on set point condition was observed (Fig. 4.19).

One interesting observation can be made from looking at Fig. 4.19. For increasing tip-sample separation, the slope of the EFM curves decrease. This effect is due to the modification of $\frac{dC}{dz}$ term of Eq. 2.14, which effects the magnitude of the ω_1 force component. This indicates that the cantilever-sample system is behaving like a parallel plate capacitor. Therefore, the voltage required to null the electrostatic field is independent of tip-sample separations (which are small compared to the lateral dimensions of the cantilever beam).

The dependence of the surface potential measurements on the amplitude of the dither voltage (V_0) was also investigated. Using the same sample and setup as for the previous experiments, the surface potential of a bulk gold test sample was measured

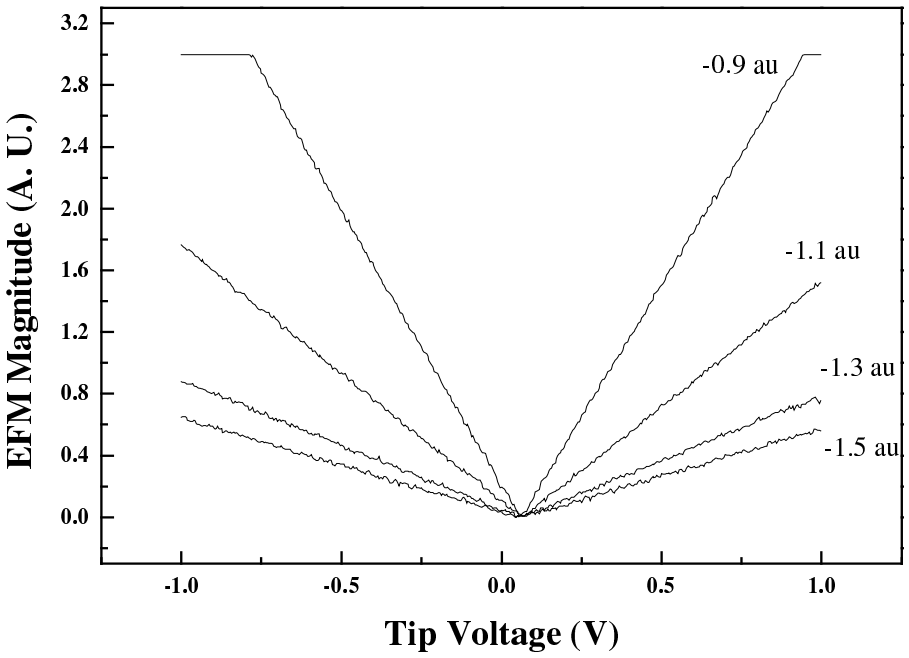

Figure 4.19. Surface potential measurements made at several different topographic set-points (in arbitrary units). The set-point values correspond to different tip-sample separation. Therefore, as the set-point value decreases, the tip-sample separation also decreases. This data indicates that the surface potential measurements are independent of z for displacements that are much smaller than the dimensions of the cantilever.

for different values of V_0. This data showed no significant dependence of the sample's surface potential on the magnitude of the dither voltage. However, an effect on the slopes of the EFM curves was observed. The slopes of the EFM curves increase as the magnitude of the dither voltage increase. This is due to the dependence of the ω_1 on the magnitude of the dither voltage ($\frac{dC}{dz}(V_S - V_{Tip})V_0 \sin \omega_1 t$).

4.6 Measuring Tip Independent Surface Potentials

One of the major utilities of EFM is the ability to probe the surface potentials produced by nanoscale objects in intimate contact with the supporting surface. The surface potential measurements provide information on the relative differences of the local work functions on a sample's surface (this is similar to the $\triangle V_{CPD}$ measured by the macroscopic Kelvin probe discussed in Chapter 2). [68] A simple experiment was conducted to determine the work function difference between two different samples probed with the same tip.

The sample used for this study consisted of a 0.5 cm $\times$ 0.5 cm Au electrode evaporated on to a clean low temperature grown GaAs (LTG:GaAs) substrate. The surface potential was first measured entirely over the exposed Au substrate and then over the LTG:GaAs surface. A plot of the surface potentials, measured with respect to the AFM tip, are shown in Fig. 4.20. The difference between the minimums of the EFM curves is +450 $\pm$ 50 mV. This result corresponds to the difference between the nominal values for work functions of Au (5.1-5.4 eV) and LTG:GaAs (4.7 eV). [69]

To understand how the relative change in the surface potential is related to the difference between the work functions of materials composing the sample, consider the situation where the surface potentials of two different metals (with work functions ϕ_1 and ϕ_2) are measured using the same AFM tip (Fig. 4.21). The surface potentials measured with respect to the tip are V_1 and V_2:

$$qV_1 = \phi_{Tip} - \phi_1 \tag{4.20}$$

and

$$qV_2 = \phi_{Tip} - \phi_2 \quad . \tag{4.21}$$

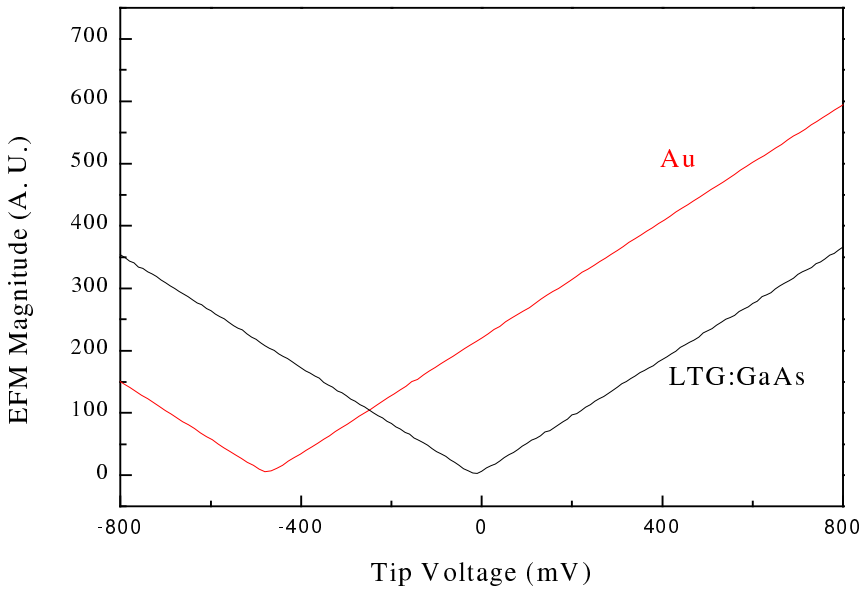

Figure 4.20. Surface potential measurements made over both the gold contact and LTG:GaAs surface. The relative difference between the minimums of the electrostatic curves corresponds to the work function difference between gold and LTG:GaAs (corresponding to a potential difference of $\triangle V_{CPD} \approx 450$ mV).

The relative difference in the potential between the two surfaces is given by

$$q(V_1 - V_2) = (\phi_{Tip} - \phi_1) - (\phi_{Tip} - \phi_2) = \phi_2 - \phi_1 \quad . \tag{4.22}$$

Since the same tip is used to measure the surface potential for each metal, the relative shift between the surface potentials is the work function difference ($\triangle V_{CPD}$) between the two metals. The data shown in Fig. 4.20 demonstrates this concept. For many experiments, it is often useful to reference the surface potential measurements to a standard reference, for example polycrystalline Au or Au(111). This is extremely helpful for complicated experiments where the same tip cannot be used between surface potential measurements.

These initial experiments helped to build confidence in the techniques used to measure the electrostatic force with an AFM. The results from these studies expanded

the understanding of the electrostatic interaction near a sample's surface, which led to improvements to the measurement techniques and exposed some shortcomings of different experimental methods. After completing this initial work, EFM techniques were used to probe the electrostatic force for several different types of systems with dimensions ranging from microns to nanometers. These studies revealed the usefulness of the EFM probe as a tool for characterizing nanoscale systems.

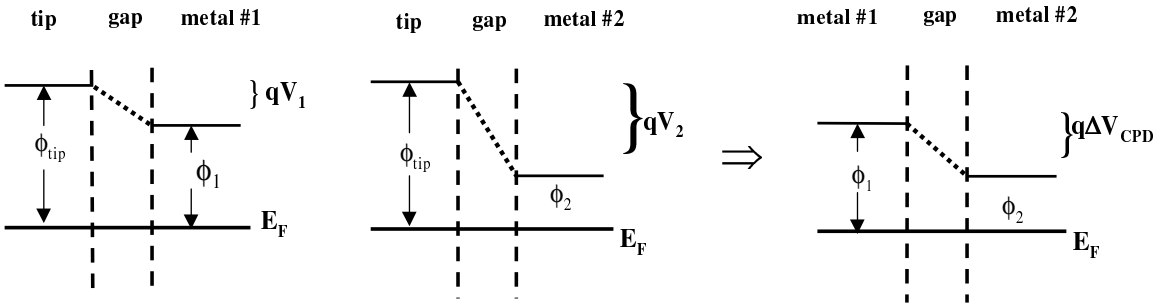

Figure 4.21. Comparison of different samples using the same probe tip.

5. SURFACE POTENTIAL MEASUREMENTS OF LTG:GaAs USING EFM

One of the most heavily used semiconductors in modern electronic applications is GaAs. GaAs possesses many characteristics that make its use in semiconductor devices very benifical. [69] However, GaAs oxidizes in only a few seconds when exposed to air. Oxygen in the air reacts with the GaAs surface and forms gallium oxide (Ga_2O_3) and arsenic oxide (As_2O_3). [70,71] Exposure of the GaAs surface to light has also been observed to enhance the rate of oxidation. [72] This enhancement results when electron-hole pairs that are formed by photons, interact with the surface.

Typically, GaAs is grown by molecular beam epitaxy (MBE) at a temperature of 600 °C. However, GaAs grown at lower temperatures (referred to as LTG:GaAs) of 250-300 °C has shown a dramatic reduction of the oxidation rate compared to GaAs grown at higher temperatures. [73] The slow oxidation of LTG:GaAs is due to a low concentration of minority carriers (holes) near the surface. LTG:GaAs offers more flexibility than GaAs due to the slow surface oxidation which can take place over several hours.

In addition to its slow oxidation, LTG:GaAs possesses a high density of point defects ($\approx 1.0\times10^{20}$ cm^{-3}) caused by the arsenic antisites (Fig. 5.1). [74] The point defects produce mid-gap states which are located 0.5 eV above the valance band and aid in conduction through the surface interface. [75] This makes LTG:GaAs useful for constructing high performance ohmic contacts.

After long exposure to ambient conditions ($\approx$ 24 hrs), the surface Fermi level is pinned at mid-gap due to the negative charge concentration of the oxide layer located on the surface (Fig. 5.2). [76] By removing the oxide layer, the negative surface charge residing at the surface of the LTG:GaAs is eliminated; thus, unpinning the

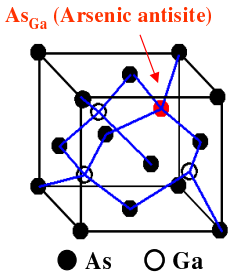

Figure 5.1. Sturcture of LTG:GaAs

conduction band of the LTG and reducing the barrier height ϕ_B (difference between the conduction band E_C and Fermi energy level E_F).

The process of building a high-quality metallic contact to an LTG:GaAs substrate requires unpinning of the Fermi level by stripping this oxide layer with a powerful etch. After the stripping, metallic contacts are then evaporated to form an electrical connection to the LTG:GaAs surface.

Several recent studies have thoroughly examined the conduction through ohmic LTG:GaAs structures. Patkar *et al.* has reported a contact resistance of $\rho_C \approx 3\times10^{-7}$ Ω-cm^2 for a macroscopic contact structure. [77] Lee *et al.* as also shown ohmic behavior of nanoscale contacts formed by a 5 nm diameter gold clusters tethered to a LTG:GaAs substrate. [78] Lee's measurements revealed that a nanoscale contact formed onto a LTG:GaAs surface possesses a contact resistance that is comparable to the large area contacts studied by Patkar.

Recently, models have been developed that accurately explain the reported conduction through macroscopic and microscopic contacts built onto LTG:GaAs surfaces. [79] These models require an unpinned Fermi level at the surface interface of the LTG:GaAs (ϕ_B < 0.7 eV).

Important questions that arise concerning the quality of the LTG:GaAs ohmic contacts are: what is the barrier height of the LTG:GaAs surface, how long does the LTG:GaAs surface remain unpinned, and how does the stripping process affect the

surface potential of the LTG:GaAs. These questions can be answered using electrostatic force microscopy.

EFM has been demonstrated to be a very useful tool for characterizing surface potentials of semiconductors. Xu *et al.* has used EFM to image and measure surface potentials of defects in GaAs thin flims. [80, 81] Rosenthal *et al.* used cross-sectional SCFM to probe the carrier concentration for different regions of heterojunction bipolar transistor (HBT). [30] Both of these studies display how EFM is capable of providing characteristic information on semiconducting surfaces.

The objective of this study was to determine the barrier height before and after the oxide layer was removed using the EFM techniques discussed earlier. Several types of LTG:GaAs surfaces were exposed to various stripping agents. The electrostatic surface potential was measured as a function of time to determine the oxidation rate and the influence of the stripping agent on the surface potential.

Previous observations of LTG:GaAs oxidation have been reported in several studies. Using STM spectroscopy, Hong *et al.* detected midgap states in a LTG:GaAs surface that had been stored in a dry nitrogen environment for approximately 25 hours. [82] These observations did not show a significant degradation of the surface states after 25 hours; indicating a slow oxidation of the surface.

Ng *et al.* has observed a slower oxidation rate for LTG:GaAs than for Stoichiometric GaAs. [73] LTG:GaAs and GaAs samples were exposed to both air and light for $\approx$ 31 hrs after removal from the MBE system. X-ray photoelectron spectroscopy (XPS) was used to measure the amount of oxide present on the samples' surfaces. These measurements revealed that the GaAs sample had a significantly higher concentration of oxide than LTG:GaAs. However, for both studies, no attempts were made to observe the transient behavior of the LTG:GaAs as the oxide layer was forming on the surface.

5.1 LTG:GaAs Sample Preparation

Figure 5.3 shows the type of LTG:GaAs samples used for this study. Several types of samples were used to determine how both the doping of the LTG:GaAs layers,

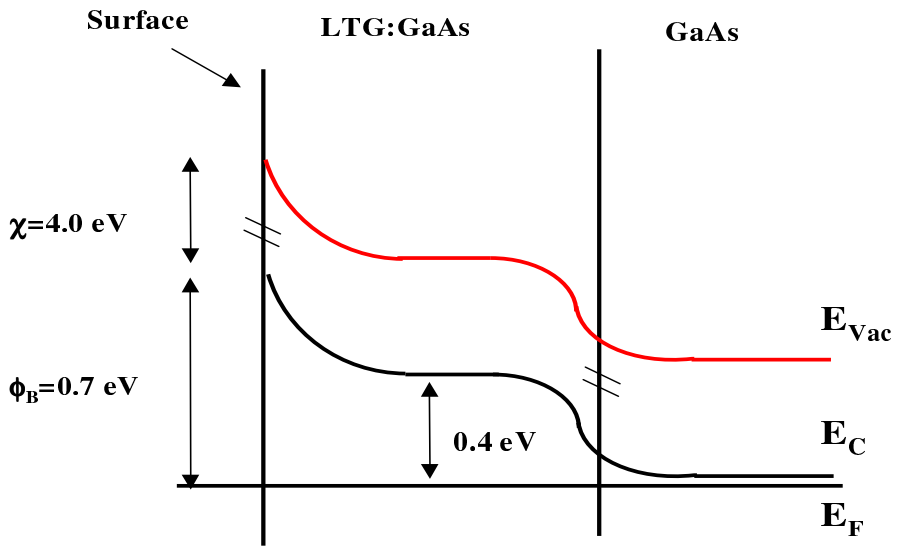

Figure 5.2. Band structure of LTG:GaAs (not to scale) after surface oxide formation. χ is the electron affinity, which is $\approx$ 4.0 eV for LTG:GaAs

as well as, the oxide removal affect the LTG:GaAs surface potential. All LTG:GaAs samples were made by Melloch *et al.* at Purdue University. [83] The first samples were made by growing a 0.5 μm buffer layer of GaAs onto a semi-insulating GaAs wafer using MBE. The buffer layer was grown at a temperature of 600 ^{o}C. An additional 0.5 μm thick layer of Be-Doped LTG:GaAs (p-GaAs: 2×10^{19} cm^{-3}) was grown onto the buffer layer at a temperature of 200 ^{o}C (Fig. 5.3 a).

Similarly, samples were also constructed with non-intentionally doped (NID) LTG layers grown on a similar buffer layer (Fig. 5.3 b). The final set of samples consisted of a thin layer of NID LTG:GaAs with a thickness of 5 nm grown onto two thin layers of doped GaAs (Fig. 5.3 c).

All samples had dimensions of 1.0 cm^2. A millimeter-sized region of Ti and Au was evaporated over a small region of the LTG:GaAs surface (evaporations were conducted by Macus Bastiutua [84]). These contacts provided both electrical connections to the LTG:GaAs surface and a reference surface that is not affected by the stripping agents.

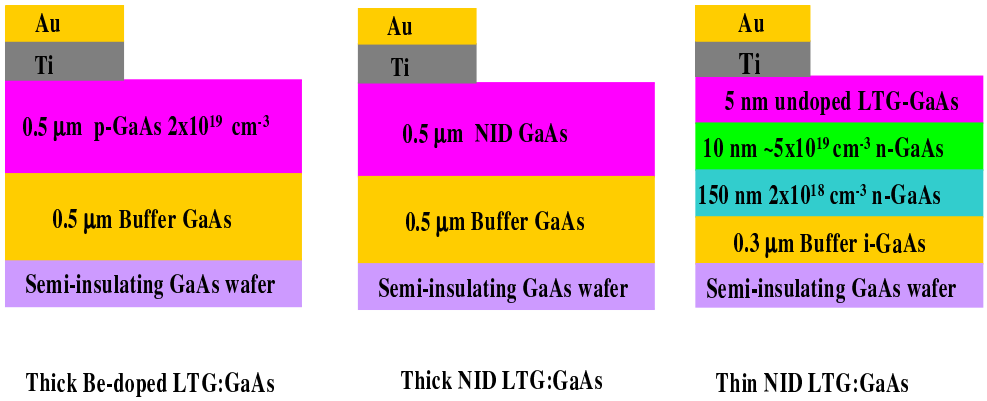

Figure 5.3. Samples structures used for this study. All samples were grown in a MBE system.

5.2 LTG:GaAs Surface Potential Measured as a Function of Time

Initially, the surface potentials of heavily oxidized Be-doped and NID LTG:GaAs were measured with respect to a polycrystalline gold substrate (Fig. 5.6 a). The AFM tip was first held at a fixed position $\approx$ 100 nm above the LTG:GaAs. The surface potential (V_S) was determined by measuring the tip bias voltage necessary to eliminate the ω_1 component of the electrostatic force ("flat-band" condition displayed in Fig. 5.4). After making several measurements over LTG:GaAs, the tip was repositioned over the Au reference electrode. All measurements were made in ambient conditions.

The LTG:GaAs was observed to have an average surface potential of $+450 \pm 50$ mV with respect to gold. This corresponds to the known differences between the work function of gold and an oxidized LTG:GaAs substrate ($\phi_{Au} = 5.1$-5.4 eV and $\phi_{LTG} = 4.7$ eV). This simple measurement helps to provide a consistent check to the techniques used to determine the surface potential of LTG:GaAs surfaces. [69]

Experiments were also conducted to determine the stability of the oxidized LTG:GaAs surfaces prior to exposure to a stripping agent. The surface potential for several LTG:GaAs and gold pieces were measured over an eight day period using the same

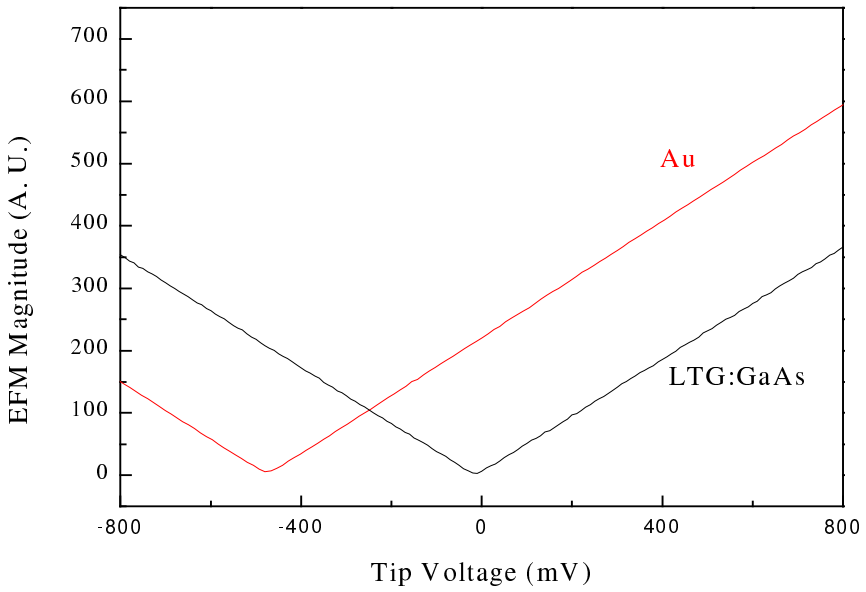

Figure 5.4. Surface potential measurements made over both the gold contact and LTG:GaAs surface. The relative difference between the minimums of the electrostatic curves corresponds to the work function difference between gold and LTG:GaAs ($\triangle V_{CPD}$= +450 $\pm$ 50 mV).

AFM cantilever. Figure 5.5 displays the relative surface potential of LTG:GaAs measured as a function of time. These observations indicated that oxidized LTG:GaAs substrates are stable for long periods of time. This information is useful in determining how instrumentation drift will affect the attempts to measure transient behavior of the LTG:GaAs surface potential after the removal of the oxide layer.

After several initial measurements, numerous studies were conducted to determine the transient behavior of the LTG:GaAs surfaces after removal of surface oxide. The LTG:GaAs samples were exposed to three different stripping agents: hydrochloric acid (HCl), potassium hydroxide (KOH) and ammonium hydroxide (NH_4OH).

The first step, prior to stripping the oxide from the surface, was to measure the surface potential of both the LTG:GaAs and gold surfaces. These measurements represented a base line for determining the initial effects of the oxide removal on the band structure of the LTG:GaAs surface.

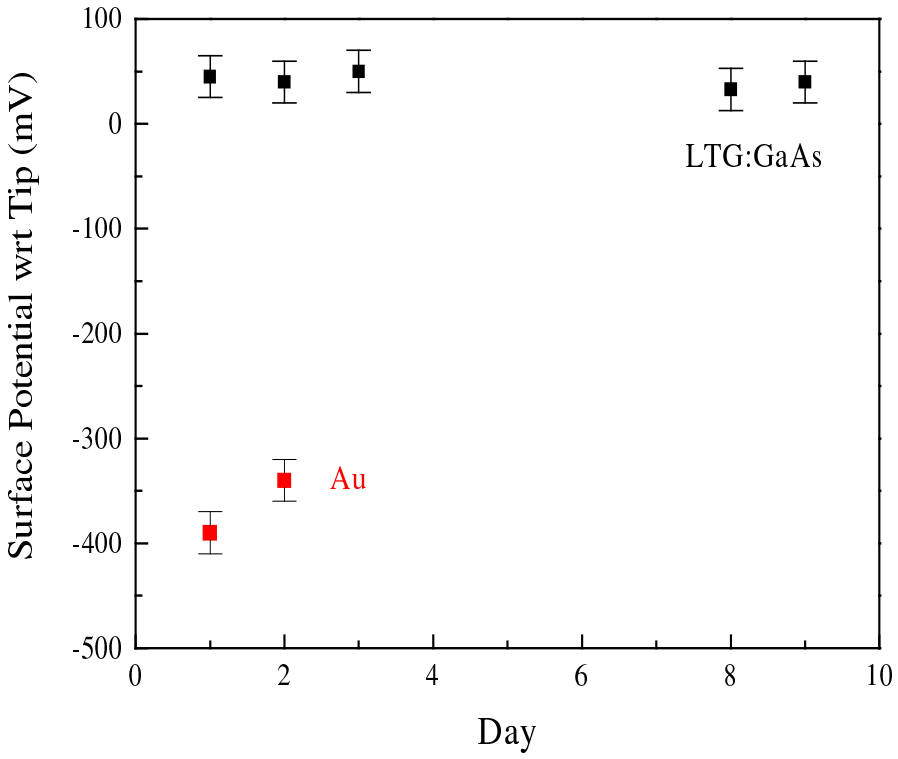

Figure 5.5. Surface potential of a LTG:GaAs surface measured as a function of time. The surface has a thick oxide layer due to prolonged exposure to air.

Based on the known band structure of NID doped, the time-evolution of the surface potential can be predicted. Prior to the oxide removal, the surface Fermi level is pinned midgap (Fig. 5.6 a). Assuming a realistic value of the work function of the Si AFM tip, in this case $\approx$ 5.1 eV, a voltage of +400 mV would have to be applied to the tip in order to produce the "flat-band" condition; thereby, shifting the tip's Fermi level down by -400 meV.

Once the oxide is stripped from the LTG:GaAs's surface, the bending of the conduction band, caused by the negative surface charge near the surface (0.7 eV), will flatten and return to its unperturbed value of 0.4 eV (Fig. 5.6 b). Therefore, a larger positive tip voltage is required to null the electrostatic force. As time passes, the surface will oxidize. The accumulation of the negative surface charge will begin to cause an increase in the bending of the conduction band, decreasing the amount of positive tip bias voltage required to eliminate the electrostatic field (Fig. 5.6 c).

After initially measuring the surface potential, the oxide layer was removed from the LTG:GaAs surface by a $\approx$ 30-60 second exposure to a solution of one of the three stripping agents used for this study. The stripping solutions used for this study were a 1.2 M solution of HCl, 0.8 M solutions of KOH and 0.8 M solution of NH_4OH. After exposure to the particular stripping agent, samples were then rinsed in DI water for $\approx$ 30 seconds and dried with N_2. The samples were then immediately placed back into the commercial AFM. [32]

Figure 5.7 displays the transient behavior that was observed for both thick Be-doped and NID LTG:GaAs after a 30 second oxide strip using HCl. As seen from the data, there is an abrupt change in the surface potential after the oxide strip. Then, as time passes, the surface potential increases and finally saturates back to its original value. The typical time to reach saturation was an average 4-9 hrs. The surface potential measured for the gold is also plotted in Fig. 5.7. The gold appeared to lack the transient behavior that was observed over the LTG:GaAs surfaces. For Be-doped LTG:GaAs surfaces, an average -350 $\pm$ 50 mV change in the surface potential was observed. Similarly, a -430 $\pm$ 120 mV average shift was also observed for NID

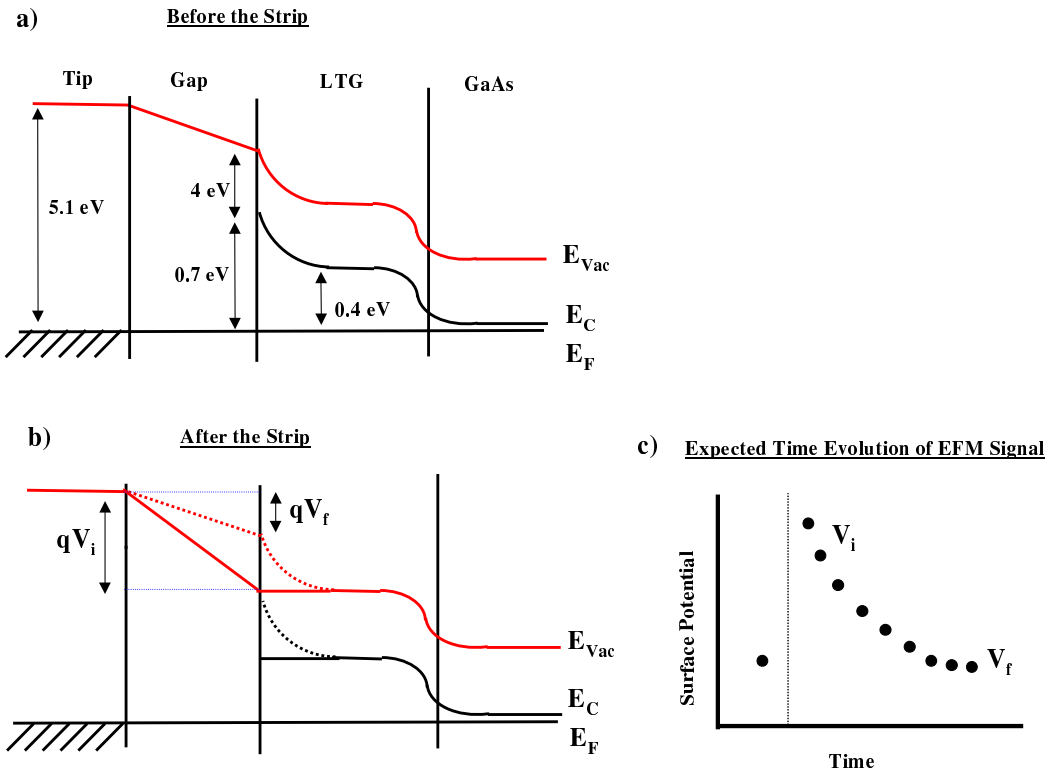

Figure 5.6. a) Band structure of LTG:GaAs surface prior to exposure to a stripping agent. b) Evolution of the structure after the removal of the oxide layer. c) the predicted response of the surface potential as the oxide layer grows on the surface.

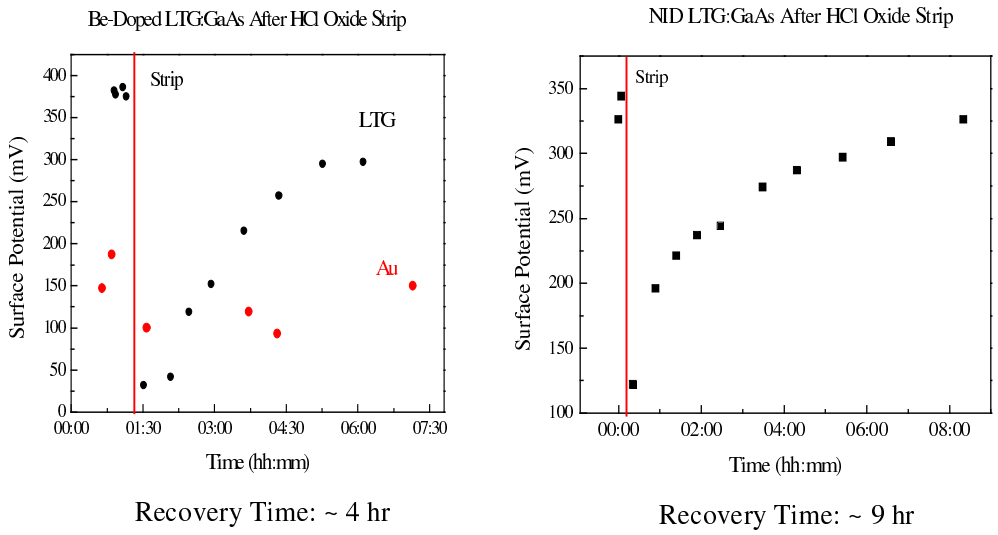

Figure 5.7. Surface potential measured as a function of time for thick LTG:GaAs before and after an HCl oxide strip.

LTG:GaAs surfaces. The transient behavior was present in both samples, indicating that the doping of the LTG:GaAs layers did not influence the time-evolution.

The time-evolution shown in Fig. 5.7 is opposite to what was predicted by the simple model proposed earlier (Fig. 5.6 c). Attempts to determine the discrepancy between the observed and predicted behaviors consisted of repeating the experiments for thin LTG:GaAs samples grown on top of thin dope layers of GaAs (Fig. 5.3). The motivation for repeating the experiments on samples composed of thin LTG:GaAs layers, was to determine if the thickness of the LTG:GaAs layers influenced the transient behavior.

Figure 5.8 shows the observed evolution of the surface potential for a thin NID LTG:GaAs (ohmic contact structure) sample after an HCl strip. Similar behavior of the surface potential was also observed over a 1 day period. The motivation for performing this experiment with thin NID LTG:GaAs was to see if the effects observed for thick layers of LTG:GaAs would be present for a thin conducting layer of LTG:GaAs. The data clearly indicates that this transient behavior is present for all three types of LTG:GaAs surfaces.

These observations indicate that the transient behavior of the LTG:GaAs surface potential has an exponential relationship with time t (in units of minutes). The time-evolution for this system is modeled as

$$V_S(t) = V_C(1 - e^{-\frac{t}{\tau}}) \quad , \tag{5.1}$$

where V_C (in units of mV) is the maximum change of the LTG:GaAs surface potential after the oxide removal and τ (in units of minutes) is a parameter representing the evolution rate of the surface potential. To determine τ for the various oxide measurements, the surface potential data was plotted on a $\ln(1 - \frac{V_S(t)}{V_C})$ vs t plot (see Fig. 5.8). τ is determined by fitting the plotted data with a linear fit. From these measurements, the average value for τ was found to be 300 ± 100 minutes.

Since the previous data showed a transient behavior that was opposite of the predicted behavior, an experiment was conducted to determine if exposure to the dark and dry nitrogen (N_2) environment would influence the time-evolution of the LTG:GaAs. Effects of due to the environment were tested by placing a LTG:GaAs sample into a dark chamber filled with nitrogen immediately after removal of the oxide with an HCl etch; thus, reducing exposure of the LTG:GaAs surface to oxygen. After making surface potential measurements for several hours in a dark, low oxygen environment, the sample was then exposed to ambient conditions.

Figure 5.9 shows the transient behavior for the different environments compared with a measurement made complete in ambient conditions. There is clear evidence that the environment plays a role in the rate of surface oxidation (zero slope in the time-evolution data during the dark N_2 exposure). This result is significant because it shows that the environment can influence the rate of change in the surface potential as the oxide layer reforms on the LTG:GaAs surface. However, even with exposure to a N_2 environment, the time evolution of the surface potential still did not correspond with the theoretical expectations.

To further investigate the differences between the observed and predicted transient behaviors, experiments were conducted to determine how different strip agents (different stripping chemistries) would affect the transient behavior. After making

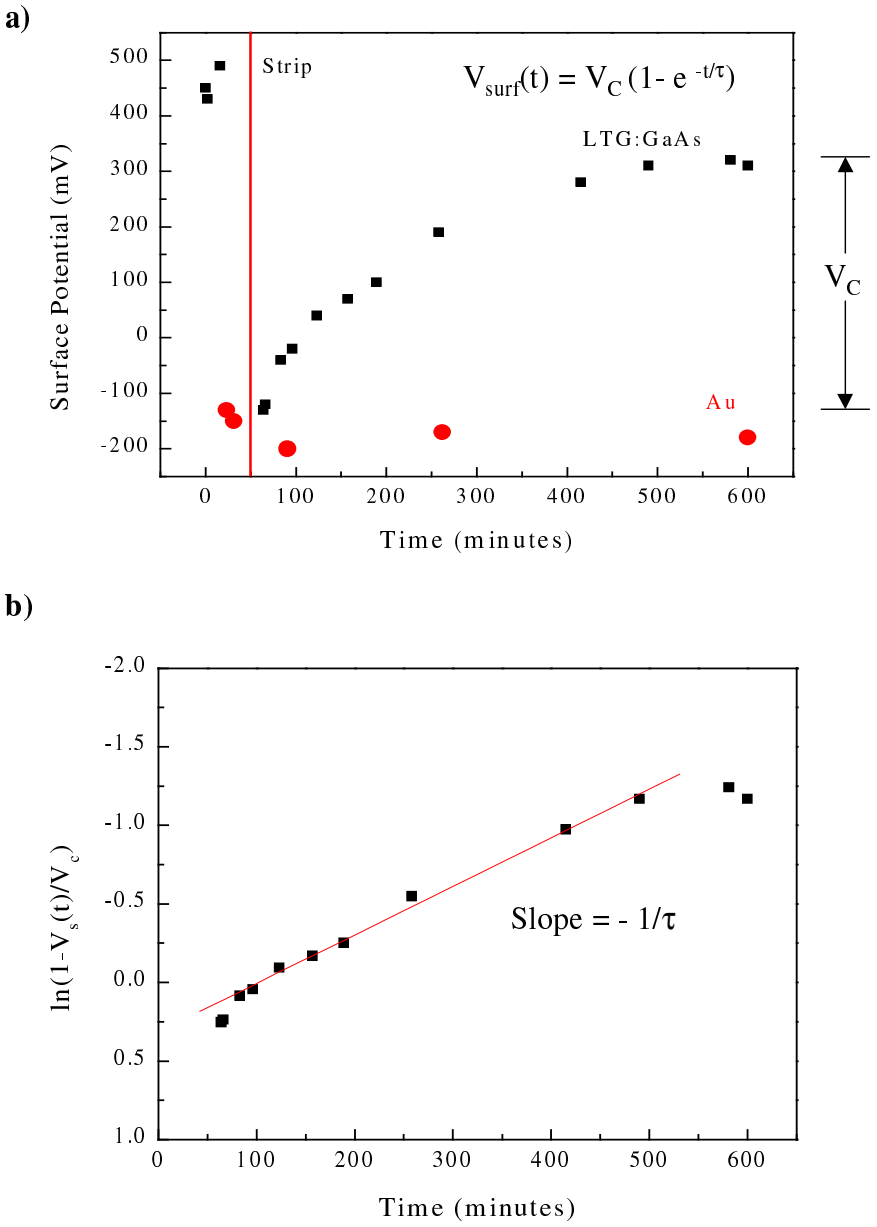

Figure 5.8. Surface potential measured as a function of time for thin LTG:GaAs before and after an HCl oxide strip

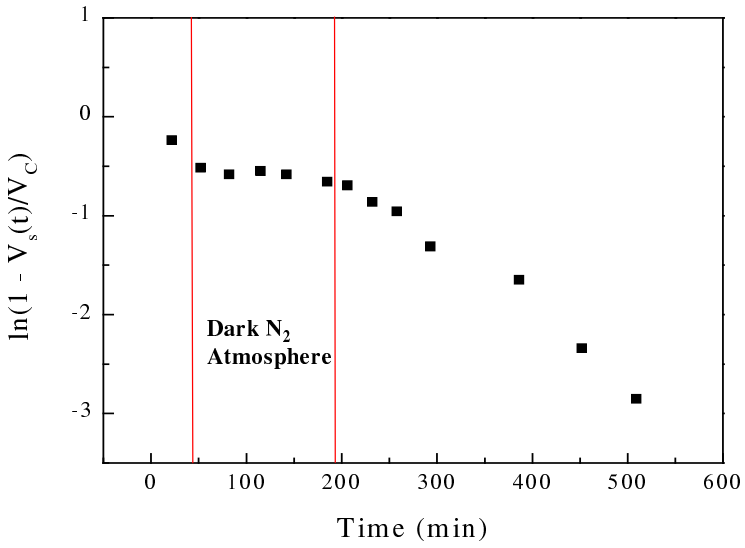

Figure 5.9. Behavior of a LTG:GaAs surface that was stored for 3.3 hrs in a dark N_2 environment shortly after an HCl oxide strip. The data shows a distinct reduction of the recovery time (smaller slope) when the sample was stored in a N_2 environment.

initial measurements of LTG:GaAs surface stripped using HCl, several measurements were then made for LTG:GaAs samples that had been exposed to KOH and NH_4OH strips.

Figure 5.10 show a difference in the transient behavior compared to surfaces that had been stripped with HCl. For both KOH and NH_4OH the average change in the surface potential after the strip was $+300 \pm 50$ mV. This would be the behavior that would be expected by the simple band structure model proposed earlier. In addition, the samples seem to saturate faster than for HCl with the surface potential never returning to its original value. This data is significant because it shows that the chemistry occurring on the LTG:GaAs surface is responsible for the observed behavior using HCl strips.

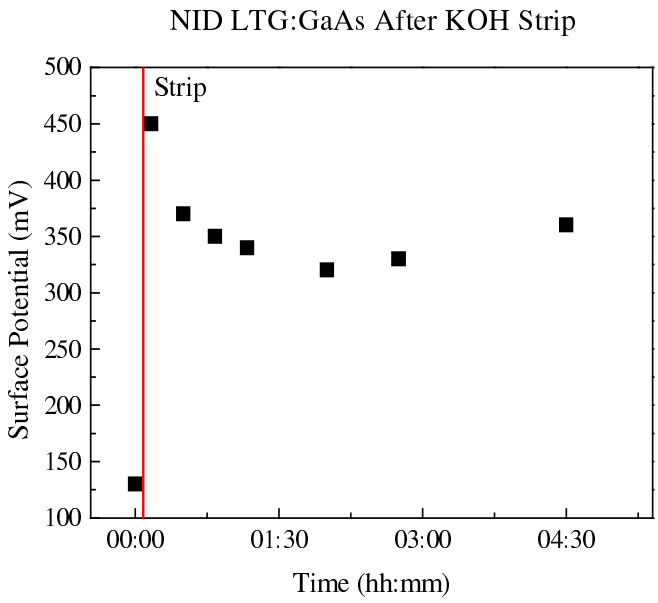

Figure 5.10. Transient behavior of the surface potential for LTG:GaAs after an KOH oxide strip.

5.3 Surface Model

The data reported in the previous section clearly shows that the surface potential of LTG:GaAs depends on the stripping process. LTG:GaAs surfaces that were stripped in KOH and NH_4OH have completely opposite behavior than surfaces stripped with HCl. However, the magnitude of the change in surface potential before and after the strip appears to be the same for all three agents ($\approx$ 300 mV).

A simple model for explaining the transient behavior could be based on the effects of ions deposited on the LTG:GaAs surface by the striping agent. In the case of HCl, there may be a mono-layer of negatively charged Cl ions attached to surface after the removal of the negative charge associated with the oxide layer. This causes an increase in the curvature of the energy bands near the LTG:GaAs surface (Fig. 5.11 a).

After long exposure to air, oxygen will react with the LTG:GaAs surface. This process forces the Cl ions off of the surface where they will form Cl_2. Thus, the negative surface charge density decreases with time (Fig. 5.11 a).

For a KOH strip, positively charged potassium ions would remain after the oxide removal; thus, producing flat energy bands near the surface of the LTG:GaAs (Fig. 5.11 b). As the sample's exposure to air continues, the potassium will react with the ambient atmosphere to produce KCO_3. This has the effect of reducing some of the positive surface charge. However, since KCO_3 is not as reactive as Cl, it is possible that KCO_3 will remain on the LTG:GaAs surface. This additional material on the surface prevents the surface potential from returning to its original value (prior to the oxide strip).

Unfortunately, these effects make it difficult to observe the unpinning of the energy bands near the LTG:GaAs surface. However, these observations do show that the striping agent does have a considerable effect on the surface potential. Further investigation is required to study the evolution of the energy bands during the formation of the oxide layer. This would have to incorporate a process of removing the ions contaminating the LTG:GaAs surface.

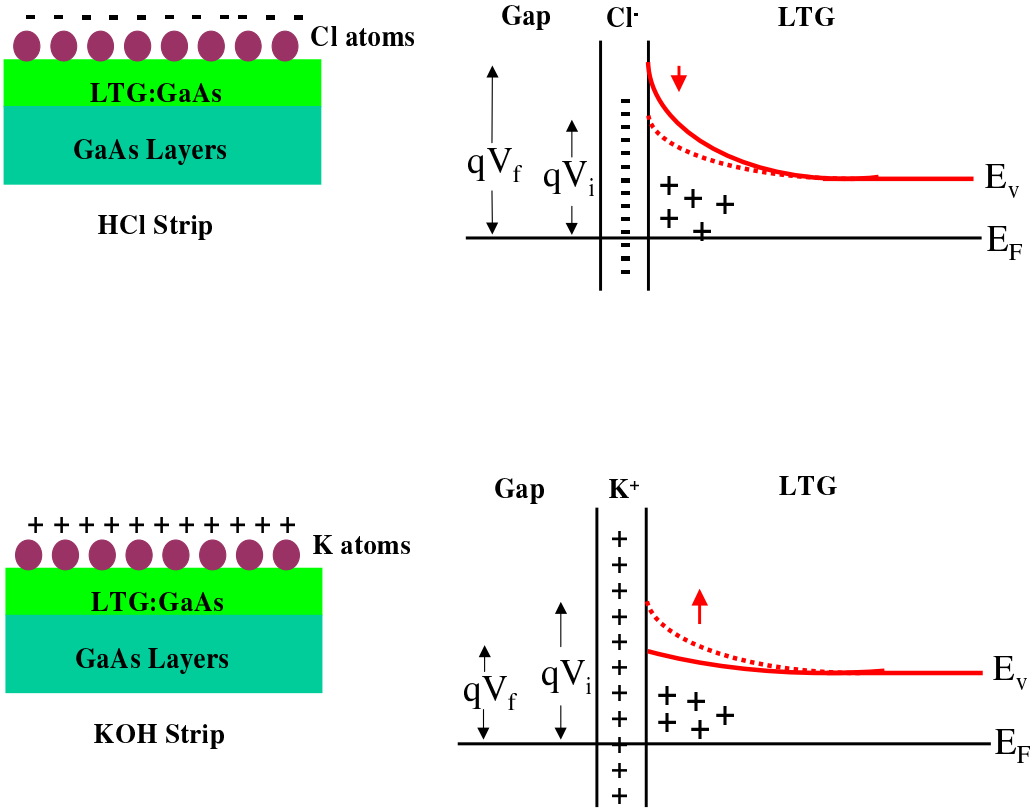

Figure 5.11. Simple models used to explain the differences in the observed transient behavior of the surface potential after different etching processes. In the case of an HCl strip, Cl ions (negative charge) remaining on the surface cause an increase in the curvature of the energy bands near the surface of the LTG:GaAs. After an oxide strip using KOH, K ions (positive charge) cause a decrease in the curvature of the energy bands. The red arrows indicate the direction in which the surface potential will shift after prolonged exposure to an ambient environment.

6. EFM MEASUREMENTS OF SINGLE Au CLUSTERS AND Au CLUSTER ARRAYS

Recent developments in self-assembled cluster technologies have allowed for the manufacture of large cluster array networks. The use of cluster arrays may play a major role in the development of nanocomputing [85]. Since cluster arrays appear to have promising applications in the world of nanoelectronics, it becomes crucial to understand the electrical characteristics of individual clusters and cluster networks. Several recent studies have shown that gold clusters tethered to a low temperature grown GaAs (LTG:GaAs) substrate possess possible applications as nanoscale devices. Lee *et al.* has observed ohmic conduction through individual dodecanethiol (DDT) encapsulated gold clusters, with a diameter of 5 nm, tethered to a low temperature grown GaAs (LTG:GaAs) substrate by a conjugated molecule. [69, 78, 86]

Recently, a model developed by Chen *et al.* has explained the conduction through a Au cluster tethered to a semi-conducting substrate reasonably well. [79] The model treats the DDT encapsulated clusters as a single system and makes the assumption that the work function of a DDT coated cluster, with a diameter of 5 nm, is $\approx$ 200 - 300 meV smaller than bulk gold. If the work function of the DDT coated cluster is smaller than bulk gold, one would expect the DDT/cluster system to have a different electrostatic surface potential than bulk gold. Therefore, probing the electrostatic properties of the clusters can provide information that is critical for supporting theories that explain the electrical properties of nanoscale metallic clusters tethered to semi-conducting substrates. These properties can be investigated using EFM techniques discussed earlier.

6.1 EFM Measurements of Single DDT Encapsulated Au Clusters Tethered to LTG:GaAs

Initial attempts to determine the work function of a gold nanocluster were conducted using single isolated encapsulated gold clusters, with a diameter of 20 nm, tethered to a low temperature grown GaAs (LTG:GaAs) substrate. These experiments helped to develop not only a useful characterization of the electronic properties of nanoclusters, but also a useful test of the obtainable resolution of EFM imaging. As noted in Chapter 4, the EFM technique can have restrictions in the resolution of images due to the convolution of the tip-cantilever system. Therefore, a great deal of experience was gained by imaging nanoscale objects, such as gold nanoclusters.

Previous studies have demonstrated the capability of using AFM to make electrostatic potential maps of individual nanoparticles deposited on various substrates. Nyffenegger *et al.* have made electrostatic force maps of sliver particles resting on a HOPG surface. [87] The nanoparticles were found to have a different potential than the background substrate. The potential variation was due to the difference in the work functions of sliver ($\approx$ 4.5 eV) and carbon (HOPG = 5.0 eV).

6.1.1 Sample Preparation

The samples used for these experiments consisted of 20 nm diameter gold clusters tethered to Be-doped LTG:GaAs. The gold clusters are encapsulated using dodecanethiol. This molecular coating helps to prevent the agglomeration of the clusters while they are suspended in a colloidal solution.

The Be-doped LTG:GaAs used for the background substrate was prepared by Melloch *et al.* [83] The substrate consisted of 0.5 μm thick layer of buffer GaAs deposited on a support semi-insulating GaAs wafer at 600 ^{o}C. A 0.5 μm thick of p-GaAs (2×10^{19} cm^{-3}) and was then deposited on top of the buffer at a lower temperature of 200 ^{o}C. Both layers were grown using molecular beam epitaxy (MBE).

Previous studies have shown that non-contact imaging produces the best topographic images of the nanoclusters. [26] During a contact scan, the forces exerted on a cluster from the AFM tip, overwhelm the surface forces holding the cluster on the

surface. [88–91] Therefore, AFM scanning in contact mode pushes the clusters across the surface, producing images devoid of clusters. When the AFM is operating in non-contact mode, the tip-sample interactions are much weaker which makes it possible to image objects that are weakly coupled to the substrate. In most situations, the tip interactions will not overwhelm the surface forces holding an object in place. However, certain situations can occur where the surface forces acting on a soft nanoscale object will be overwhelmed by the tip, even in non-contact mode. To eliminate this problem, it is often useful to tether objects to the surface using a linking molecule.

For this study, the clusters are tethered to the LTG:GaAs substrate using xylyl dithiol (XYL: HS-CH_2-C_6H_4-CH_2-SH). In order to deposit XYL SAM on the flat LTG:GaAs surface, the substrates are soaked in 1 mM solution of XYL in an organic solvent (such as ethanol or acetonitrile) for 12 - 18 hours. The oxide layer on the surface of the LTG:GaAs is stripped using HCl prior to adsorption of the XYL.

The advantage of using XYL is that the sulfur end groups of the molecule can bond to both the 111 facets of the cluster and the LTG:GaAs surface. XYL also has unique electrical properties that are instrumental for forming good nanoscale ohmic contacts. XYL is a conjugated molecule that provides good electrical contact between the clusters and the LTG:GaAs surface. This conjugation is necessary in order to allow equilibrium of Fermi levels of the cluster and substrate.

After adsorbing XYL on the LTG:GaAs surface, the clusters are deposited by placing a millimeter-size droplet of clusters suspended in solvent onto the XYL coated surface. As the solvent evaporates, the clusters come into contact with the XYL, which bonds them to the surface. All samples, used for this study, were prepared by Jia Liu [92] and Marcus Batistuta [84].

6.1.2 Measured Results

Figures 6.1 and 6.2 display simultaneous non-contact and EFM (without null feedback) images obtained for 20 nm diameter encapsulated gold clusters tethered to a LTG:GaAs substrate. The close examination of the topographic and EFM images, shown Fig. 6.1, provides information on the tip convolution. The effect of tip con-

volution is seen when comparing the experimentally measured height of the cluster (21 $\pm$ 1 nm) to its laterally measured diameter (200 $\pm$ 30 nm, which is 10 times the height). For non-contact measurements, the topographic height is more accurate than lateral dimensions. Similarly, the EFM images also show lateral convolution of the electrostatic force, which is approximately the same as for the topography.

An EFM image for several gold clusters can be seen in Fig. 6.2. The magnitude of the electrostatic force was measured for six clusters residing in a 740 nm square region on the LTG:GaAs surface. The EFM image indicates that AFM tip is experiencing nearly the same electrostatic force while over each cluster. This is a strong indication that the clusters acquire the same potential ($V_{Cluster}$) relative to the LTG:GaAs substrate. The potential difference originates from the work function difference between gold and LTG:GaAs.

Displayed in Fig. 6.1 are several EFM images of a single 20 nm diameter gold cluster. The images were acquired using different tip voltages. By applying different voltages to the tip, the magnitude and phase of the detected electrostatic force will change. This is seen in Fig. 6.1 b) and d). For Fig. 6.1 b), the tip bias voltage was +680 mV, while for d) the tip voltage was -680 mV. From these images, it is clearly seen that the EFM Map of the clusters transforms from a peak to a pit.

The cluster's electrostatic potential is determined by adjusting the tip voltage until the variations in the EFM image disappeare. At this point, the force due to the tip's interaction with the substrate and cluster is balanced. The contrast of the cluster in the EFM image of Fig. 6.1 c) was eliminated by a tip bias of -230 $\pm$ 20 mV. Therefore, there were no detectable differences between the force acting on the tip from the substrate or the cluster (no contrast in the EFM image).

By applying a simple convolution analysis to this system, the potential difference between the clusters and the substrate can be determined. To better illustrate this analysis, consider the forces acting on the tip and cantilever as the tip moves over nanometer sized cluster with a electrostatic potential $V_{Cluster}$ tethered to a substrate with a potential V_{Sub} (Fig. 6.3). The total force acting on the tip when it is positioned

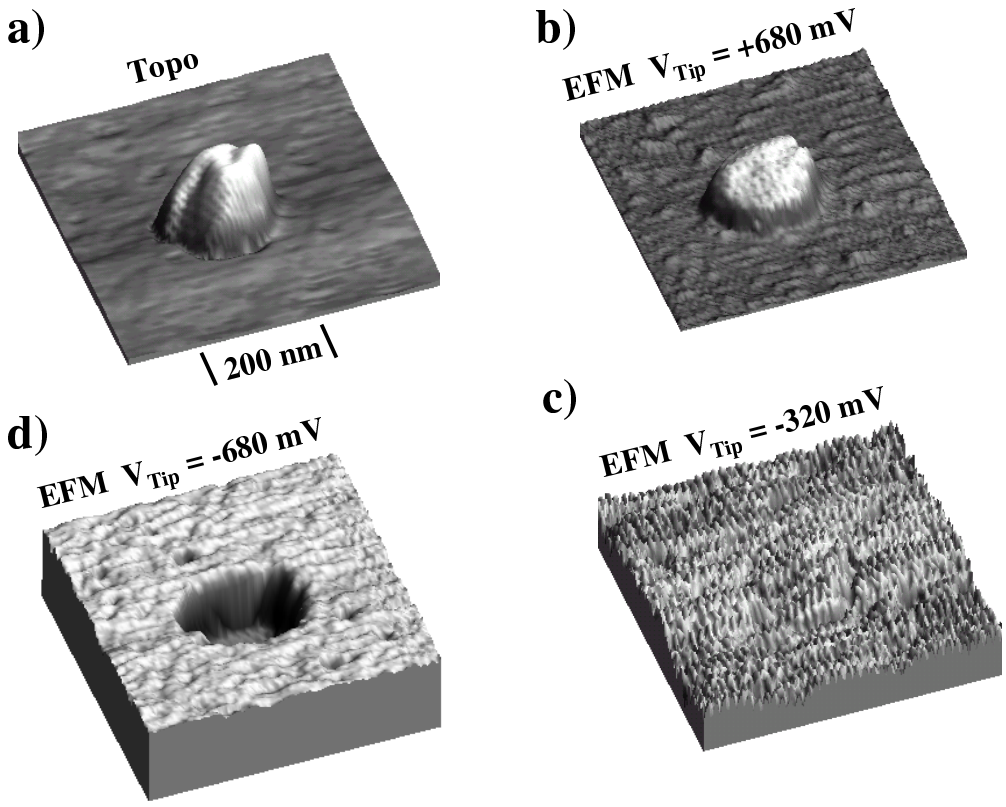

Figure 6.1. Simultaneous topographic and electrostatic images of a 21 nm diameter gold cluster tethered to a LTG:GaAs surface. The EFM images were acquired for several different tip bias voltages.

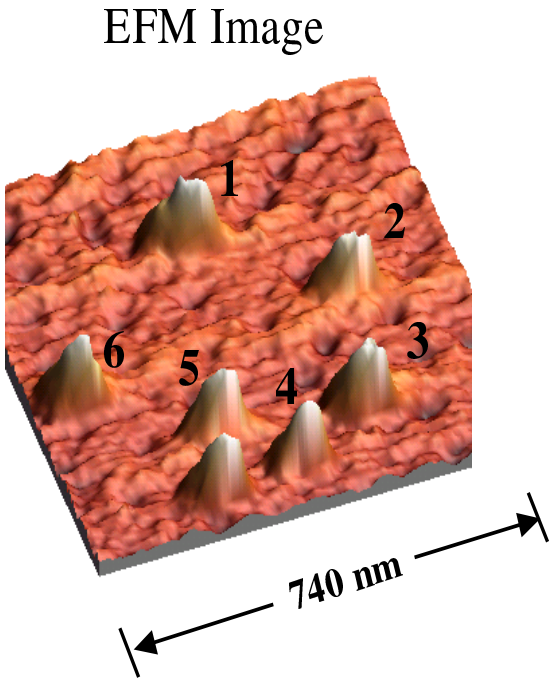

Cluster	Electrostatic Force A.U.
1	0.48
2	0.45
3	0.48
4	0.44
5	0.47
6	0.48

Figure 6.2. An EFM image of several 20 nm clusters tethered to a LTG:GaAs surface. The clusters appear charged to a uniform electrostatic potential (same height profiles in the EFM image).

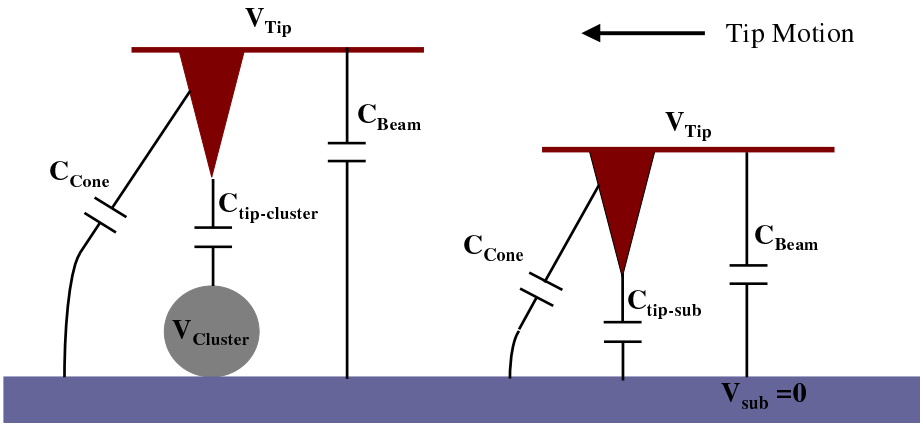

Figure 6.3. Simple model for determining the potential of the cluster based on the convolution of the cantilever with the background. Since the cantilever's dimensions are orders of magnitude larger that the cluster, it will only interact with the substrate. Therefore, EFM variations are only due to the interaction of the tip with cluster.

only over the substrate is given by

$$F_{Total_{Sub}} = \frac{dC_{Tip-Sub}}{dz}(V_{Sub} - V_{Tip})^2 + \frac{dC_{Cone-Sub}}{dz}(V_{Sub} - V_{Tip})^2 + \frac{dC_{Beam-Sub}}{dz}(V_{Sub} - V_{Tip})^2 \quad , \tag{6.1}$$

where $C_{Tip-Sub}$ is the capacitance of the tip's apex over the substrate, $C_{Cone-Sub}$ is the capacitance of the tip's canonical shaft over the substrate and $C_{Beam-Sub}$ is the capacitance of the cantilever beam over the substrate.

The force acting on the tip-cantilever system is a combination of interactions between tip's apex and substrate, the tip's cone with the substrate and the cantilever's beam with the substrate. When the apex of the tip is located over the substrate, the capacitance of the tip-substrate system ($C_{Tip-Sub}$) is modeled by a conducting sphere over a conducting plane.

Similarly, the forces acting on the tip when it is positioned over the cluster is given by

$$F_{Total_{Cluster}} = \frac{dC_{Tip-Cluster}}{dz}(V_{Cluster} - V_{Tip})^2 + \frac{dC_{Cone-Sub}}{dz}(V_{Sub} - V_{Tip})^2$$

$$+\frac{dC_{Beam-Sub}}{dz}(V_{Sub}-V_{Tip})^2 \quad . \tag{6.2}$$

When the apex of the tip is located over the cluster, the capacitance of the tip-cluster system ($C_{Tip-Cluster}$) is modeled by the capacitance of two conducting spheres with the same diameter separated by height of the tip above the cluster.

Since the cone of the tip and beam of the cantilever have physical dimensions much larger than the cluster, these interactions will be dominated by the background substrate. Therefore, the forces acting on the tip's cone and cantilever's beam do not depend on the presence of the cluster. Because the cone and beam interact with a large area of the substrate, force variations in the EFM images are mainly due to the interaction of the tip's apex with the sample surface.

Based on the discussion above, the condition for eliminating the contrast in an electrostatic force map is (eliminating the ω_1 component of the total force)

$$F_{Total_{Sub}} = F_{Total_{Cluster}} = \frac{dC_{Tip-Sub}}{dz}(V_{Sub}-V_{Tip})^2 = \frac{dC_{Tip-Cluster}}{dz}(V_{Cluster}-V_{Tip})^2 \quad . \tag{6.3}$$

From equation 6.3, the relative difference between the cluster and substrate can be estimated from the measured V_{Tip}.

The interaction between the tip and substrate can be modeled as a sphere over a plane. Similarly, the interaction between the tip and clusters can be modeled as two spheres with approximately the same diameter. For this simple system, the capacitance of two spheres is $\frac{1}{2}$ of the capacitance of a sphere over a conducting plane:

$$C_{Tip-Cluster} = \frac{1}{2}C_{Tip-Sub} \quad . \tag{6.4}$$

Substituting this relation of the capacitance into Eq. 6.3, the potentials can be related by

$$(V_{Sub}-V_{Tip})^2 = \frac{1}{2}(V_{Cluster}-V_{Tip})^2 \quad . \tag{6.5}$$

Taking the potential of the surface to be ground (V_{sub} = 0 Volts) and the tip voltage required to eliminate the contrast of the EFM image (V_{Tip} = -230 $\pm$ 20 mV), the potential difference between of the cluster relative to the substrate is estimated

to be -550 $\pm$ 50 mV. The potential estimated for a single cluster corresponds to the difference between the work functions of Au ($\phi_{Au} \approx$ 5.1-5.4 eV) and LTG:GaAs ($\phi_{LTG} \approx$ 4.7 eV). [69]

Using the capacitance of this simple system along with the cluster's contact potential, the charge on the cluster can be estimated. For this system the capacitance can be modeled as a sphere over a conducting plane: [93]

$$C_{cluster-sub} = 4\pi\epsilon_0 R(1 + \frac{R}{2(z+R)} + \frac{(R^2/4(z+R)^2)}{(1 - R^2/4(z+R)^2)} + ...) \quad , \qquad (6.6)$$

where R is the radius of the clusters and z is the distance between the cluster's surface and substrate.

Using a cluster radius of 10 nm and a cluster-substrate separation of 1 nm, the charge on the clusters is estimated to be 1.06×10^{-18} Coul. This corresponds to approximately 7 electrons. However, even though this simple model which produces results that are consistent with the work function difference between gold and LTG:GaAs, the tip convolution still increases the uncertainty of the surface potential measurements of objects with dimensions smaller than the AFM's tip. The effects of tip convolution can be reduced by probing a sample with an equipotential surface with an area much larger than the cantilever's beam. Such a surface can be produced by self-assembling the clusters into a well-organized array with dimensions of hundreds of microns. The next section will discuss electrostatic measurements of this type of self-assembled system.

6.2 AFM and EFM Measurements of Au Cluster Arrays

For this portion of the study, the electrostatic surface potential was measured for several unlinked self-assembled arrays of DDT encapsulated 5 nm diameter gold clusters. The arrays are tethered to an underlying gold substrate by a linking molecule, which chemically bonds to both the clusters and the substrate.

The motivation for conducting studies on self-assembled arrays of clusters was based on two goals. Initially, electrostatic force images made of the cluster array were used to gain important insight on the minimum resolution of the EFM imaging

technique. The second goal was to measure the electrostatic surface potential of the array using the techniques discussed earlier.

Since the array consisted of many smaller individual clusters close-packed together, they formed a much larger equipotential surface with dimensions much larger than the cantilever. This led to a reduction in convolution effects present in electrostatic measurements.

All surface potential measurements were made with respect to the underlying gold surface coated with a linking molecule; thereby, deducing the surface potential only produced by the encapsulated clusters. These potential measurements can yield information into the work function of the encapsulated clusters.

6.2.1 Sample Preparation

Figure 6.4 displays the schematic of the samples used in this study. All samples consisted of an array of encapsulated gold clusters tethered to a bulk Au substrate. The size of the array was small enough to allow large exposed regions of the underlining gold substrate near the edge of the sample, which makes it possible to measure the electrostatic surface potential over millimeter-sized regions of both the self-assembled cluster array and coated bulk Au substrate.

The underlying substrate was made by depositing 10 nm Ti and then evaporating 200 nm of gold evaporated onto to a Be-Doped LTG:GaAs substrate [83] (evaporations were made by Marcus Batistuta [84]). The cluster array was tethered to the gold substrate using XYL as the linking molecule. SAMs of XYL were prepared in a similar fashion as for the single cluster experiments.

Clusters used to form the array had a nominal diameter of 5.2 ± 0.6 nm and were stored in a colloidal solution. To prevent the clusters from agglomerating while in the solution, they were encapsulated by a thin film of DDT. A lift process was used to deposit the cluster array on the gold surface. [94, 95] DDT encapsulated Au clusters were mixed with the solvent hexane. A few drops of the concentrated cluster-hexane solution were cast onto the surface of water. As the hexane evaporated, the clusters self-assembled into a close-packed array. With the array floating on the surface of the

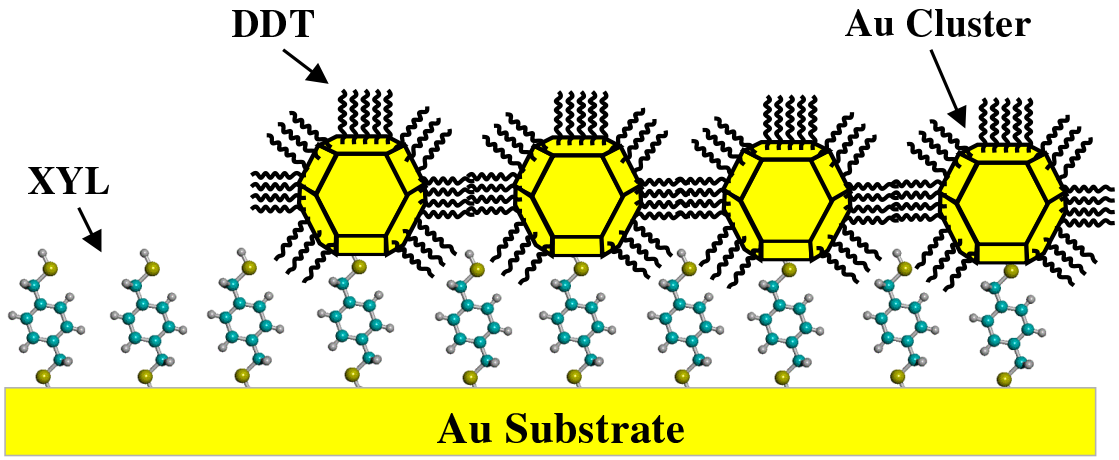

Figure 6.4. Schematic diagram (not to scale) of the samples used in this study. Gold clusters, with a diameter of 5 nm, are tethered to a gold substrate using XYL as the tethering molecule. The clusters are encapsulated in DDT to prevent agglomeration when they are stored in solution. Using a unique deposition process, cluster arrays that were continuous over hundred of microns were tethered to centimeter-sized gold substrates. The cluster was deposited in the center of the bulk gold sample, leaving millimeter-sized regions of exposed bulk gold near the edge of the sample. This allows for measurements of electrostatic surface potential to be made completely over the array and then over the XYL coated gold surface.

water, a flat gold substrate coated with a tether molecule (XYL) was brought into contact with the water layer. Once in contact with the array, the tether molecules bonded to the 111 sites on the clusters, tethering them to the substrate. This process can create self-assembled cluster arrays that are continuous over hundreds of microns (all cluster arrays were deposited by Jia Liu [96]).

6.2.2 Measured Results

Initial evidence of the difference between the surface potential of cluster arrays and bulk gold substrates can be seen in Fig. 6.5. Figure 6.5 displays both the topographic image of the cluster array and a map of the relative electrostatic force (ω_1 component of Eq. 2.13) as a function of position. The topographic image of the array indicates the existence of large defects that expose the underlying gold substrate. The measured depths of the defects were found to be 5 ± 1 nm, which corresponded to the size for the clusters used to form the array.

Variations in the contrast of the EFM image (Fig. 6.5 b), indicate a change in the magnitude and phase of the electrostatic force for different regions of the sample. It is clearly noticeable that the XYL coated gold substrate has a lower surface potential than the cluster array (bulk gold regions appear darker using false color scale).

Since the defects in the array were small when compared to the dimensions of the cantilever, convolution effects present in KFM images made quantitatively measuring relative differences in the surface potential very difficult. In addition, high-resolution images of the arrays, demonstrate that this particular AFM was not capable of resolving the individual 5 nm diameter clusters that were close-packed to form the array. This was also evident in the EFM image.

To determine the surface potential of the array, the technique discussed in the Chapter 2 was utilized. Using samples designed to minimize the effects of convolution, the AFM tip was held in a stationary position approximately 100 nm over the cluster array.

Since the cluster array typically has some defects, several topographic non-contact scans were made prior to the EFM measurements to verify the tip's position over the

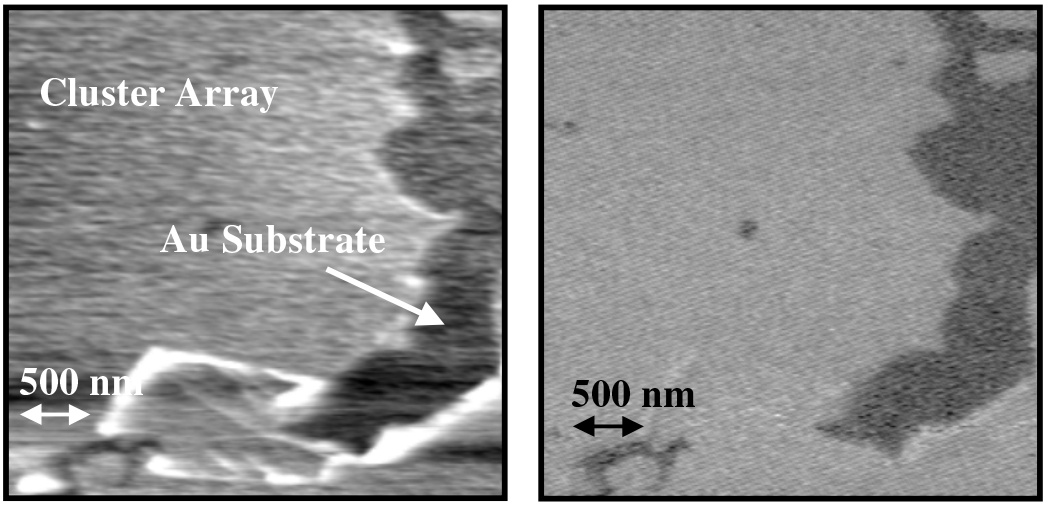

Figure 6.5. a) Topographic image of the cluster array that has been tethered to a gold substrate. b) EFM image of the surface. The topographic and electrostatic images were measured simultaneously. The topographic image revealed defects that were present in the cluster array. These defects expose the underlying bulk gold substrate. The electrostatic image displayed a variation in the electrostatic force when the AFM tip was located over a hole in the array. This image indicated the array has a higher electrostatic surface potential compared to the underlying XYL coated gold substrate

array. Figure 6.5 shows a typical topographic image of the array. The density of the defects was low enough as to not affect the overall surface potential measurement (since their dimension was small when compared to the AFM cantilever).

After verifying the tip's position over the array, the electrostatic surface potential of the array was measured by determining the tip bias needed to eliminate the ω_1 component of the force. These measurements were made for several different positions over the array separated by approximately several hundred microns. After making electrostatic measurements over the array, the AFM tip was repositioned over the exposed XYL coated Au substrate. Once again several surface potential measurements were made for several different locations over the XYL coated Au substrate.

Figure 6.6 shows typical measurements of the electrostatic force as a function of dc tip bias voltage for positions on and off of the cluster array. The EFM measurements of several cluster arrays indicate an average surface potential of $+200 \pm 20$ mV with respect to the surface potential of XYL coated bulk gold.

Since the array has a more positive electrostatic surface potential, a larger positive dc tip bias voltage was required to achieve the "flat band" condition when compared to the XYL coated gold substrate. The major implication of this finding is that the work function of the DDT/cluster system forming the array, has a lower value than XYL coated gold. If the DDT/cluster system had the same work function as XYL coated gold, there would be a very small difference in the surface potentials between the cluster array and the XYL coated gold substrate.

The charge density of the array can be estimated using the array's surface potential with respect to the XYL coated gold and by modeling the array as a sheet of charge positioned over a conducting plane. The surface potential of the array can be modeled as a thin disk with a surface charge σ_{array} positioned a distance d over a grounded conducting plane. The electrostatic potential produced on axis by a thin disk (with a radius R) is given by

$$V(z,R) = \frac{\sigma}{2\epsilon}[\sqrt{R^2+z^2} - z] \quad , \tag{6.7}$$

where $\epsilon = K \times \epsilon_0$ and K is the dielectric constant of the molecule's tethering the array to the substrate. Since the array is suspended above a grounded gold surface, the potential above the array will be a combination of the potential produced by the clusters' charges and their images. Using Eq. 6.7, the potential above the array is given by

$$V_{array}(z,R) = \frac{\sigma_{array}}{2\epsilon}[\sqrt{R^2+z^2} - z] + \frac{-\sigma_{array}}{2\epsilon}[\sqrt{R^2+(z+2d)^2} - (z+2d)] \quad . \tag{6.8}$$

For the EFM experiments, $R \gg z$, thus, Eq. 6.8 reduces to

$$V_{array} = \frac{\sigma_{array} d}{\epsilon} \quad . \tag{6.9}$$

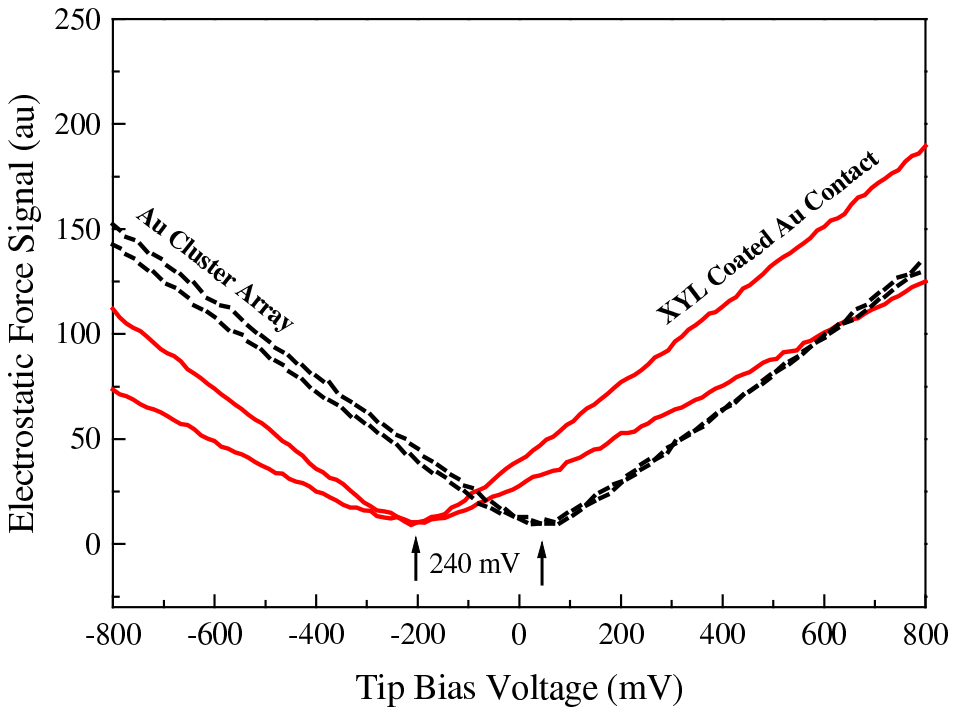

Figure 6.6. Several typical measurements of the electrostatic force as a function of the dc tip bias voltage for different positions located over the cluster array and XYL coated gold substrate. When the tip is at the same electrostatic potential as the substrate, the magnitude of the electrostatic force is minimized. By measuring the tip voltage that produces the minimum electrostatic force, one can determine the relative electrostatic potential differences between cluster array and XYL coated gold substrates.

Eq. 6.9 can now be used to estimate σ_{array}:

$$\sigma_{array} = \frac{V_{array}\epsilon}{d} \quad . \tag{6.10}$$

Using a d of 3.3 nm (combined length of the XYL molecule, 0.8 nm, and the cluster's radius), $K = 2$ (dielectric constant of the XYL monolayer) and the array's surface potential of +200 mV, the σ_{array} is estimated to be $\approx 1.0 \times 10^{-3}$ Coul/m^2. The amount of charge located on each individual encapsulated cluster is estimated from the charge density of the array and the lateral area of an individual cluster. The lateral area of the cluster is approximated by a thin disk with a radius of 4.1 nm (the combined length of the DDT molecule, 1.6 nm, and the cluster's radius). The cluster's area is estimated to be to be $\approx 5.3 \times 10^{-17}$ m^2. Therefore, the estimated charge on an individual cluster is $\approx 5.7 \times 10^{-20}$ Coul. This amount of charge roughly corresponds to ≈ 0.4 electrons on each individual DDT/cluster system.

The potential of an individual cluster is also determined from the its net charge and capacitance. For this system, the capacitance of a 5 nm diameter cluster positioned 0.8 nm (length of XYL molecule) above a conducting plane is calculated to be 5×10^{-19} F. This yields a DDT/cluster potential of ≈ 100 mV with respect to the underlying bulk gold substrate.

This data provides strong support to the assumptions needed to explain current conduction through a nanoscale ohmic contact. However, one must take into account the effects of the molecular interactions on electrostatic fields close to the clusters and substrate.

Independent measurements made of XYL SAMs deposited on flat gold substrates indicate that a small electrostatic surface potential is generated by the dipole moments formed by the molecular bonds attaching to the gold surface. XYL coated gold was found to have an electrostatic surface potential of 50 ± 30 mV with respect to bare bulk gold. Since XYL is a symmetric molecule, one would expect a small dipole moment to be formed by the molecule's bond to the bulk gold and an equal and opposite dipole moment to be formed by the molecule's bond to a 111 facet on a cluster. Therefore, the net dipole formed by the XYL bonds should be small compared

to the electrostatic field produced by the difference in the work functions of the bulk gold and the clusters.

Since the clusters were prepared from a colloidal solution, they were also encapsulated in DDT. Independent measurements of DDT SAMs deposited on flat gold surfaces have shown initial indications that the DDT forms a stronger surface dipole than XYL. DDT coated bulk gold has been found to have a surface potential that is 102 $\pm$ 40 mV with respect to bare gold. This may account for the potential determined for an individual DDT/cluster system. This would suggest that the work function of the naked 5 nm cluster is the same as bulk gold. However, determination of the molecule's effects on the cluster requires further experiments.

The measurements of single clusters and array of clusters have shown that EFM is capable of imaging with a lateral resolution of 50 nm. In addition, EFM measurements have shown that in the case of a single 20 nm cluster, the cluster's potential is approximately that of bulk gold when taken with respect to a LTG:GaAs substrate. This suggests that the work function of the 20 nm clusters is close the bulk value of gold. However, for a cluster consisting of 5 nm encapsulated clusters, the work function appears to be lower than bulk gold. An interesting aspect of the later situation is that potential of an array may depend on the electronic properties of the molecules adsorbed to the clusters. This effect may have significant application for chemical sensing.

7. EFM MEASUREMENTS OF SELF-ASSEMBLED MONOLAYERS

It is well known that when a solution of thiols is exposed to a gold surface, they will chemisorb to the gold surface and form a highly oriented self-assembled monolayer (SAM). [1,3] In recent years, various uses of SAMs have been vigorously investigated. [97] The self-assembly of molecules will have many applications in the rapidly developing field of nanotechnology, nanolithography, nanoelectronic devices, and nanosensors. [98–100]

In general, the interaction between a surface and a molecule is not well understood. The measurement of electrostatic surface potential, defined simply as dipole-charge distribution, can provide a fast and quantitative measure of this process. In addition, the surface potential measurements can yield insight into structural and electronic properties of monolayers. They can also provide a diagnostic signature or fingerprint for the molecule or a class of molecules. Further, the surface potential measurements can aid in developing better models that describe the current flow through a molecule. [101,102]

In recent years, the modification to a metal's surface potential after the adsorption of a SAM has become of considerable interest to the nano-electronic community. The electrostatic potentials produced by SAMs can eventually be used to create built-in potential drops across nanoscale components. As molecular devices approach a nanometer length scale, EFM will play a critical role in the characterization of such devices.

To further improve the understanding of the resulting effects on the electrostatic potential of a metallic surface due to a molecular monolayer, EFM measurements were conducted for aliphatic and aromatic thiols chemisorbed to Au(111) substrates. The

measured electrostatic potential in all cases was referenced to a clean Au(111) substrate in order to remove the background electrostatic potential between the tip and bare Au. Thus, we have deduced the electrostatic potential produced by a molecule that is bound to a substrate. The origin of the measured potential is intimately related to the bonding and orientation, as well as, the chemical composition of the molecule and thus, represents a quantity of considerable fundamental interest, as well as, potential application for chemical sensors.

In order to build a level of confidence, initial surface potential measurements were conducted and modeled for alkanethiol SAMs. The variation of surface potential was measured as a function of chain length. After initial work with the alkanethiols, several molecules were investigated. Additional studies were conducted on molecules that possessed a symmetric and non-symmetric molecular structure. EFM studies were also conducted on a molecular system that was modified by a chemical charge transfer complex. These studies revealed the possibility of using a modification to a molecule's dipole moment as a chemical sensor. Additional studies on other types of molecules are listed in Appendix G.

7.1 Modeling the Surface Potential Produced by a SAM

The electrostatic surface potential produced by SAM originates from the dipole moment of the molecule's charge density. It is convenient to model the molecular monolayer as a sheet of electric dipoles. The electrostatic potential produced at point P in space due to a single electric dipole is given by [103]

$$V(P) = \frac{\vec{p} \cdot \hat{r}}{4\pi\epsilon_0 r^2} \quad , \tag{7.1}$$

where $\vec{p} = \sum_{n=1}^{i} q_n \vec{d_n}$ is the dipole moment of a collection of i point charges.

Eq. 7.1 can be used to calculate the potential a distance z above the center of a circular sheet of dipoles with a radius R and density N_p (number of dipole moments / unit area). The potential produced from a sheet of dipoles oriented in the z direction is given by,

$$V(z,R) \quad = \quad \frac{1}{4\pi\epsilon_0} \int_0^R \int_0^{2\pi} \frac{N_p p z R' dR' d\theta}{(R'^2 + z^2)^{3/2}} \tag{7.2}$$

$$= -\frac{N_p p z}{2\epsilon_0}\left(\frac{1}{\sqrt{R^2+z^2}} - \frac{1}{z}\right) \quad , \tag{7.3}$$

where p is the magnitude of an individual dipole moment oriented along the z-axis. In the situation $R \gg z$ (typical dimensions of an EFM experiment), Eq. 7.3 becomes

$$V_{surf} = \frac{N_p p}{2\epsilon_0} \quad . \tag{7.4}$$

In the simplest case, if p is the dipole formed for two equal and opposite charges $(+q, -q)$ separated by a distance d in the z direction, Eq. 7.4 becomes

$$V_{surf} = \frac{N_p p}{2\epsilon_0} = \frac{N_p q d}{2\epsilon_0} = \frac{\sigma d}{2\epsilon_0} \ , \tag{7.5}$$

which is the potential above two equal and opposite charge sheets separated by a distance d.

Eq. 7.4 can be used to calculate the surface potential formed by a monolayer of molecules. To make such calculations, it becomes necessary to determine the magnitude and location of charges associated with the molecular bonds. Once an individual molecule's dipole moment is known, the total surface potential for the monolayer can be calculated using (Fig. 7.1),

$$V_{mol} = 2\frac{N_{mol}\sum_{n=1}^{i} q_n d_n \cos\theta}{2\epsilon} \quad , \tag{7.6}$$

where N_{mol} is the packing density of the molecule on the sample surface, θ is the angular orientation of the molecule with respect to the z-axis and $\epsilon = K\epsilon_0$ (K is the dielectric constant of the monolayer). Since the SAMs are bonded to a gold surface, Eq. 7.6 is a factor of two larger than Eq. 7.4 due to the addition of image dipoles.

Eq. 7.6 appears simple, but calculating the $\sum_{n=1}^{i} q_n d_n$ component is no easy task. To determine the location and magnitude of the charge requires the use of sophisticated quantum chemistry algorithms. Initial calculations of surface potentials formed by alkanethiols SAMs will be discussed in further detail in later sections.

7.2 Characterization of Self-Assembled Monolayers

When attempting to conduct studies of SAMs, it becomes important to characterize the SAM prior to the experiment. There are many different well-established

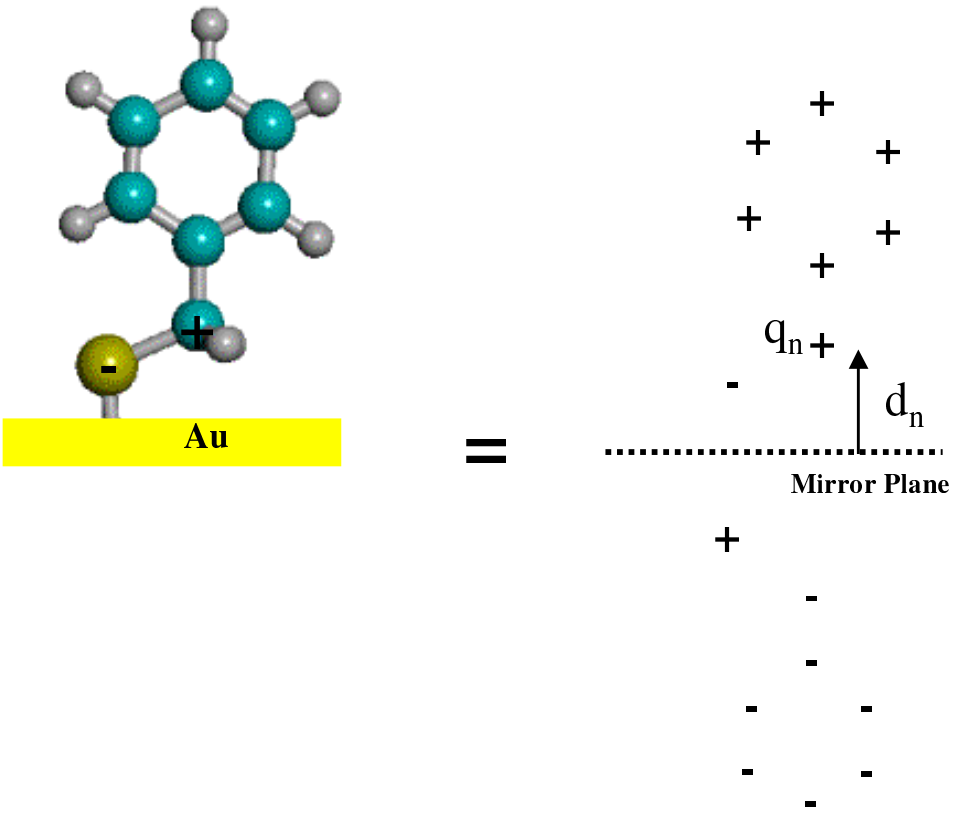

Figure 7.1. Physical interpretation used to model a SAM of molecules as an array of dipoles.

techniques that can provide a great deal of useful information on the properties of a SAM. Some of the more commonly used methods for characterizing SAMs are reflection absorption infra red spectroscopy (RAIRS) and ellipsometry. Both techniques are based on the interaction of photons with the molecules forming the SAM. In addition to the optical methods, the AFM and scanning tunneling microscopy (STM) are also valuable tools for characterizing SAM formation.

7.2.1 Optical Characterization of SAMs

RAIRS can be used to detect the presence and orientation of molecules bonded to a surface. [104] RAIRS works by shining infrared light on a surface coated with molecules that are vibrating. If the molecules have a dipole moment, they can absorb

infrared light only at certain frequencies. Thus, the infrared spectrum of the reflected light will have absorption peaks that are characteristic of the molecules present on the surface.

Elliposometry is a similar optical technique that works by shining polarized light onto the sample's surface at an oblique angle. [105] Measuring the relative intensities of the parallel and perpendicular components of the reflected light provides information on the thickness of the monolayer. By using variable wavelengths of the polarized light, the dielectric properties of the monolayer can be estimated.

7.2.2 AFM Characterization of SAMs

The optical techniques mentioned above are useful for characterizing the SAM over the entire sample. However, they lack the resolution to identify submicron defects in SAM. The ultra-high resolution capabilities of AFM makes it a vital tool for characterizing the SAM's structural properties that have length scales smaller than the minimum resolution of the optical methods. Since the surface potentials produced by molecules depend strongly on their structural properties, topographic information is necessary for the interpretation of EFM measurements.

In recent years, a large number of AFM experiments have yielded a great deal of information regarding molecular structure. [106–109] It has been demonstrated that AFMs have the ability to image the individual molecules comprising the SAM. However, in order to achieve molecular imaging, a very stable and sensitive AFM is required. Some AFMs lack the ultra-high resolution capabilities need to accomplish structural work. However, useful information can still be obtained by examining images of SAMs with a submicron length scale.

Figure 7.2 is a non-contact topographic scan of a Au(111) surface coated by a nonanethiol ($CH_3(CH_2)_8SH$) molecule (nonanethiol samples were prepared by Emilia Lugowska [110]). Even though the AFM used for these studies did not achieve molecular resolution, useful information can still be extracted from the surface imaging. There is clear evidence of this due to a large number of defects, $\approx$ 100 defects/μm^2, present in the SAM. The defects have a depth of $\approx$ 1 nm which corresponds to the

length of the nonanethiol molecule. This image is supportive of claims made in the literature that nonanethiol does not form a well-ordered SAM. [3,111]

Imaging the formation of nano-scale water droplets on a hydrophobic SAM also provides additional characterization. Figure 7.3 shows sequential images of a C-10 calixarene SAM acquired during the exposure to a dry N_2 environment for 12 hrs (C-10 calixarene samples were prepared by Steve Tripp [112]) Initially, after the calixarene was exposed to a humid ambient environment, a thin monolayer of water was adsorbed onto defects in the SAM. This was evident from the formation of water droplets on the sample's surface (Fig. 7.3 a). After three additional hours of exposure to the N_2 environment, the water droplets evaporated from the surface (see Fig. 7.3 b).

The formation of water droplets on the surface of the SAM is caused by the hydrophobic nature of the C-10 calixarene molecule. Since the calixarene SAM is hydrophobic, small water droplets on the surface will migrate to defected sites where there is no monolayer of molecules. At these sites, the water droplets will conglomerate to produce large droplets. The water droplets are large enough to be detected in non-contact mode; thus, providing a non-destructive technique for pinpointing defects in the SAM. The technique of using the hydrophobic nature of a molecule to pinpoint defects in the monolayer is an adequate method of characterization of the SAM when the AFM is not capable of achieving sub-angstrom resolution.

7.3 Surface Potential Measurements of Alkanethiols Bonded to Au(111)

To place the electrostatic surface potential measurement of molecules on a firmer foundation, initial studies focused on alkanethiols. The surface potentials of various alkanethiols have been investigated previously [111, 113, 114] providing a point of reference for EFM studies on molecules of more interest.

7.3.1 Previous Studies of Alkanethiols

Evans *et al.* first studied the surface potentials of self-assembled alkanethiols of different chain lengths adsorbed on gold surfaces. [111] These measurements were conducted using a macroscopic Kelvin probe. Since the probe diameter was on the order of a few millimeters, the surface potential produced by a large number of molecules

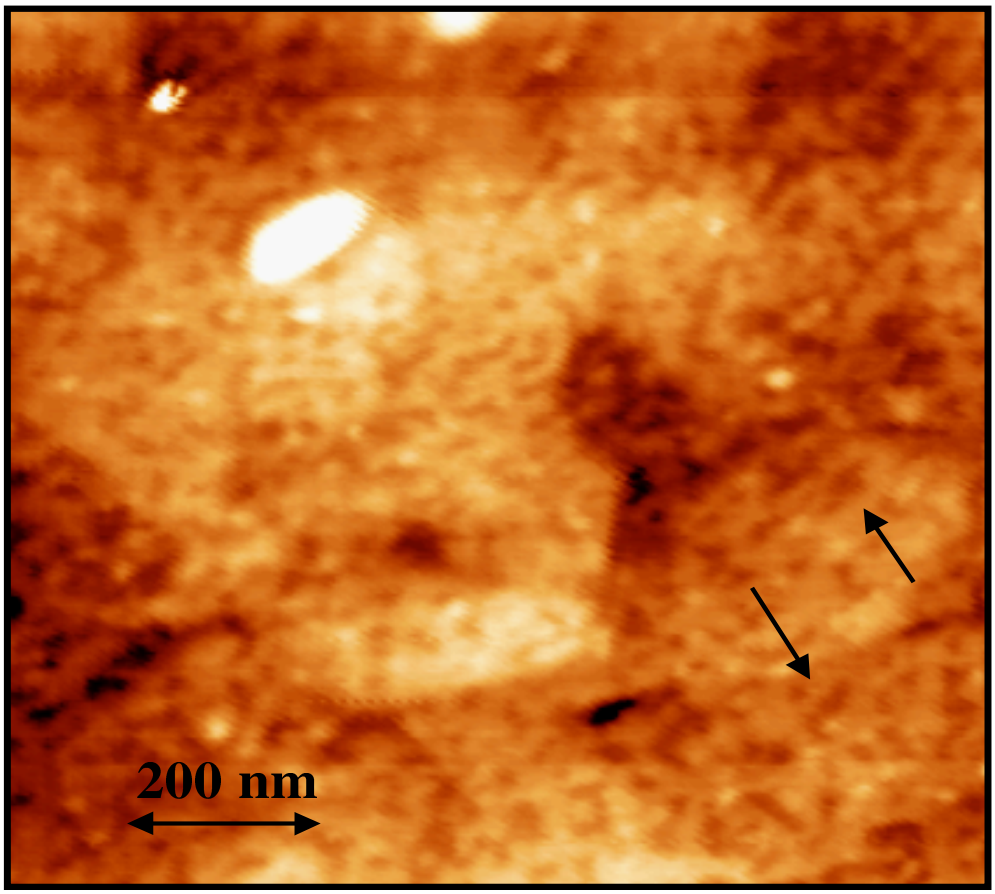

Figure 7.2. Non-contact image of nonanethiol (C-9) SAM adsorbed on a Au(111) surface. Defects in the SAM are evident by the appearance of the small pits on the gold grains (arrows).

($\approx 10^{13}$) was measured. The results of these measurements indicated a dependence of the electrostatic surface potential on the number of CH_2 groups that formed the backbone of the alkanethiols. A change of ~10 mV per CH_2 group was observed.

More recently, Lu *et al.* have used a Kelvin force microscope (KFM) to measure the surface potential of alkanethiol SAMs transferred to a gold substrate using micro-contact printing techniques. [113,114] Since the measurements were made using KFM, lateral resolution of the surface potential measurement was reduced to $\approx$ 50 nm. These measurements also indicated a similar dependence of the surface potential on the chain length of alkanethiols. A dependence of ~14 mV per CH_2 group was observed. Unfortunately, these measurements were made with respect to a COOH terminated thiol SAM, making it difficult to estimate the absolute value of the potential produced by the molecules themselves.

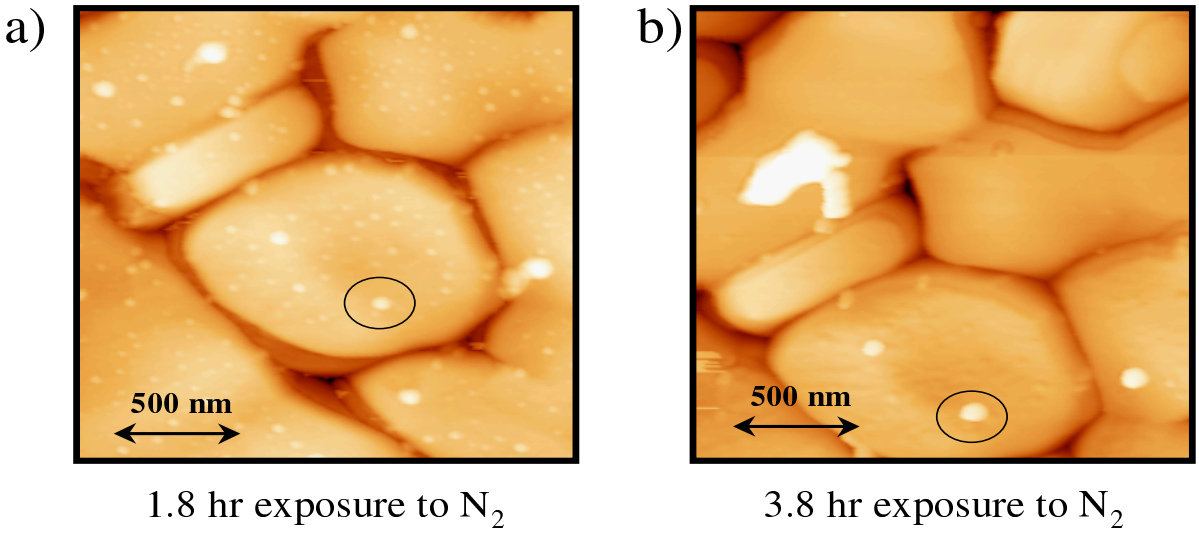

Figure 7.3. Non-contact images of a C-10 calixarene SAM during long exposure to N_2. As the exposure continues, small water droplets on the surface vanish. Larger objects located on the grains are used as references for comparison of different images. The large object that appeared in the upper-middle left side of Fig. b is contamination from the ambient surrounding and not related to the water droplets present in the earlier image.

Taken together, these two previous studies show a strong dependence in the polarity and magnitude of the electrostatic surface potential on the number of CH_2 groups present in an alkanethiol molecule. In these previous studies [111, 113, 114], the SAMs were modeled as a two-dimensional ensemble of dipoles with length l, where l is approximately the length of the molecule. A layer of negative charge resides very close to the Au substrate, while the positive charge was thought to lie at the tail of the molecule, approximately a distance l above the gold surface. The orientation of the dipole moment is inferred from the positive slope in the surface potential as the chain length is increased. This implies that the increase in potential measured with increasing alkane chain length is directly related to the change in the distance between the two charge sheets.

7.3.2 EFM Measurements of Dodecanethiol and Octadecylthiol SAMs

For initial studies, SAMs of alkanethiols - dodecanethiol (DDT, $CH_3(CH_2)_{11}SH$) and octadecylthiol (ODT, $CH_3(CH_2)_{17}SH$) (Fig. 7.4) were prepared on flat, clean Au(111). The Au(111) surface was prepared from a commercially available gold substrate made by depositing 10 nm of Cr and then 200 nm of Au on a glass substrate having dimensions of 1 cm $\times$ 1 cm. [115] The substrates were flame annealed and cleaned in ethanol prior to SAM preparation. The annealing process produced large atomically flat regions of Au(111). A Au reference electrode was established by using one of Au(111) substrates. The surface potential measurements were also referenced to an oxidized piece of LTG:GaAs. As reported earlier, the LTG:GaAs has a stable surface potential (Fig. 5.5).

The electrostatic surface potential of each flamed gold substrate, as well as, the gold reference electrode was measured prior to SAM deposition. These measurements indicated that the surface potentials of the bare Au(111) samples were within $\pm$ 50 mV of the gold reference. The measurements were also referenced to the LTG:GaAs to ensure that the Au pieces had a reasonable surface potential ($\approx$ -450 mV with respect to LTG:GaAs).These measurements indicated that the flame annealing process did not affect the relative surface potential of the gold substartes. For these studies, only substrates that had similar surface potentials after the annealing process were used.

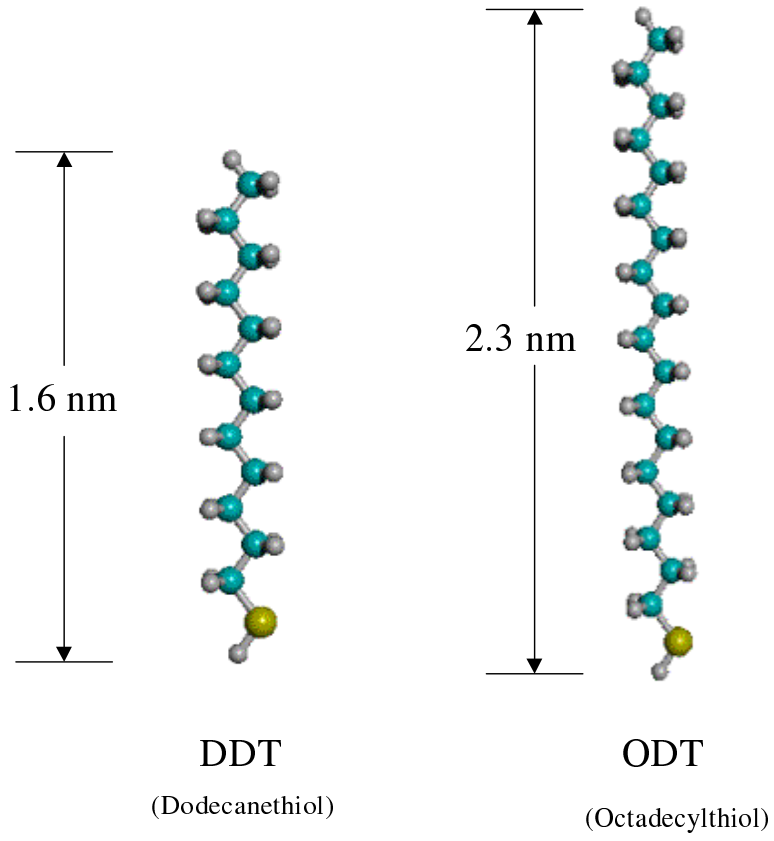

Figure 7.4. Structure of DDT and ODT.

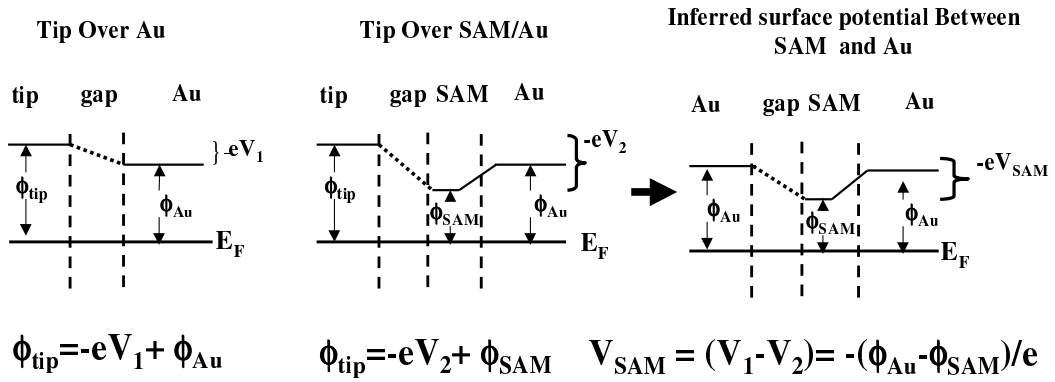

Figure 7.5. Comparison of surface potentials measured for a SAM/Au and bare Au surface using the same AFM tip.

After an initial EFM surface check, the substrates were then placed in a 1-5 mM solution of thiols in an organic solvent (such as ethanol, dichloromethane and acetonitrile) for $\approx$ 12 hrs. The samples were then rinsed and soaked repeatedly in ethanol to remove any physisorbed molecules. The samples were then dried with nitrogen gas and placed in a vacuum desiccator until the measurements were made.

The commercial air AFM [32] was used to measure the morphology and electrostatic potential of alkanethiol SAMs adsorbed to gold substrates. A standard optical beam bounce detection scheme was employed to detect both the surface and the electrostatic forces. The reported measurements were made using heavily doped silicon tips with a nominal spring constant of 2 N/m. [42] The electrostatic surface potential (V_S) was measured using a standard non-contact force detection technique discussed in previous chapters.

The surface potentials of different samples were measured with the same AFM tip with respect to a Au(111) reference sample. This allows us to subtract the surface potential of Au(111) from the potential produced by the adsorbed molecule (see Fig. 7.5). This is possible, because the work function of the tip is the same for each potential measurement.

EFM measurements were made over several different regions of the sample surface. All measurements were conducted in both an ambient and a dry N_2 atmosphere, in order to determine the effects of the surrounding ambient environment. For this set of initial measurements, effects from the ambient environment had no noticeable effects on the surface potential. This is most likely due to the hydrophobic nature of the alkanethiols.

Since the electrostatic force is a long-range interaction [64], the cantilever, as well as the tip, contributes to the electrostatic force. For this reason, we estimate that the region of the SAM interrogated by the EFM technique is roughly given by a circular region having a diameter of ≈ 40 μm, a dimension determined roughly by the triangular region of the cantilever supporting the tip.

Initial EFM measurements indicated an average surface potential of 100 ± 20 mV for a DDT SAM and 230 ± 30 mV for an ODT SAM. Figure 7.6 shows our data in addition to data from the previous studies conducted on alkanethiols. The large offset between our measured surface potentials and those reported in the literature arise from referencing the measurements to different standards. Lu *et al.* used a COOH terminated alkanethiol as their reference, making direct comparisons to our data imposible. [113,114] However, Evans *et al.* did reference their measurements to polycrystalline Au. [111]

There are many factors that may explain the large offset between the two sets of data referenced to bare Au. For our experiments, we use flame annealed Au(111) surface and Evans *et al.* use freshly evaporated polycrystalline Au. If the S-Au bonding is affected by the orientation of the surface Au atoms, then it is plausible that the charge associated with the S-Au bond also depends on the orientation of the Au surface atoms. Thus, the charge associated with the S-Au bond can cause an offset in the magnitude of the surface potential, while the relative dependence of the surface potential on chain length controlled by the charge associated with the CH_2 groups. However, more investigations are required to determine if orientation of the Au atoms influence the magnitude of the surface potential.

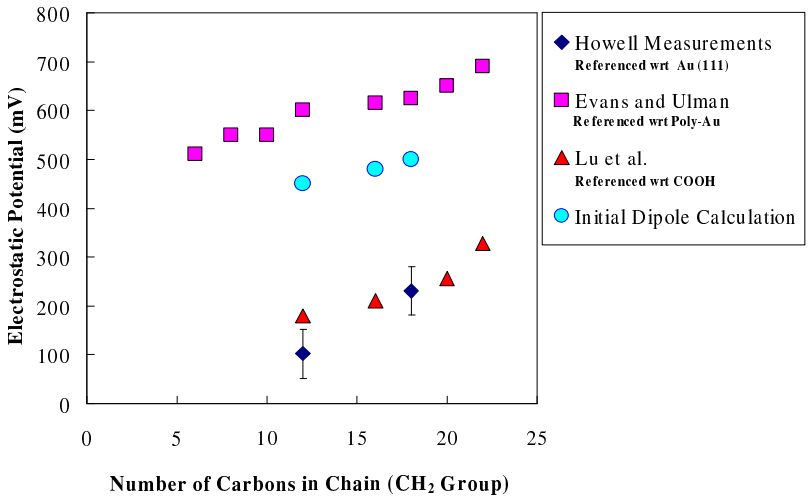

Figure 7.6. Electrostatic surface potentials as a function of alkane chain length. Measurements from two previous studies are also included in the plot. The relative dependence of the surface potential on chain length is similar for all three studies.

In addition, the surface potential of Au is very sensitive to contamination. Similarly, the preparation of the Au surface can also have an impact on the overall potential difference. The preparation of the Au surface can affect the packing density as well as the orientation of the molecule. These factors can greatly influence the overall magnitude of the molecule's surface potential. The determination of how exactly these factors influence surface potential of SAM is still under investigation.

As a result of the uncertainties of the absolute values of the surface potentials, it becomes relevant to discuss only relative changes between alkanethiols with different chain lengths. For our measurements, the relative dependence of the surface potential on chain length was determined to be 20 $\pm$ 30 mV per CH_2 group. This is in reasonable agreement with chain length dependence observed in the previous studies despite the offsets in the absolute potential measurements. [111,113,114]

Measurements were also conducted over several days, with 1-2 day separation between measurements. The relative difference between surface potentials of the DDT

and ODT SAMs was found to decrease slightly with time (Fig. 7.7). This may be an indicator that the SAM is in a process of organizing. This hypotheses is supported by reported observation of SAM structural changes observed over time. [108]

7.3.3 Modeling the Surface Potential for an Alkanethiol SAM

While qualitative pictures for variations of surface potentials with chain length or top end groups have been presented previously, there is no quantitative understanding of these measurements at present. As a first step toward developing a comprehensive model, the surface potentials of alkanethiols bonded to Au(111) is modeled by Eq. 7.6. The dipole moments of DDT and ODT are calculated using commercially available quantum chemistry software. [116] These initial calculations determine the dipole of the alkanethiol molecule without the Au(111) atoms (ignoring the molecular sulfur-Au interaction).

The dipole moments, normal to the Au(111) surface, for DDT, hexadecanethiol (HDT: $CH_3(CH_2)_{15}SH$) and ODT are calculated to be 0.67 D, 0.72 D and 0.74 D respectively (D = 1 Debye = 3.336×10^{-30} C m). Eq. 7.6 is used to calculate the surface potential produced by a sheet of molecular dipoles. Using typical parameters such as a packing density of 4.46×10^{18} molecules/meter^2 [106], a molecular tilt of 30^o [3] and a dielectric constant of ≈ 2.5 [111], the model potentials for DDT, HDT and ODT are calculated to be +450 mV, +480 mV and +500 mV respectively (see Fig. 7.6). The modeled potentials show a similar dependence on the number of CH_2 groups as the experimental data. The magnitude of the calculated potentials is closer to Evans' data. This suggests that EFM measurements may be an indicator of how well the SAM is organized when it is bound to a metallic surface

Eq. 7.6 is also used to determine the dipole moments of DDT and ODT from the Purdue surface potential data. Using the parameters mentioned above, the dipole moments of DDT and ODT are estimated to be 0.17 D and 0.39 D respectively. The measured dipole moments for DDT and ODT were smaller than the calculated values. In addition, the dependence of the dipole moments on number of CH_2 groups present in the molecule is different by a factor of three between the calculated and measured

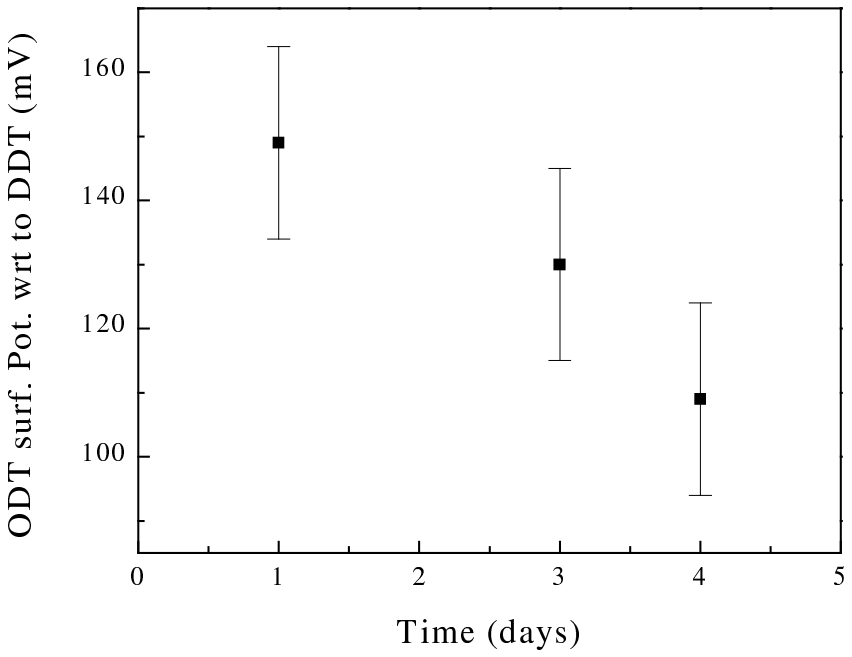

Figure 7.7. Surface potential of ODT (referenced to DDT) measured as a function of time. The data shows a nearly linear decay of the potential difference between ODT and DDT. These measurements were made with the same AFM tip and molecular samples.

dipoles. Even with these discrepancies, the measured dipole values are within an order of magnitude when compared with primitive calculations. However, to establish a more appropriate model, the bonding of the alkanethiols with the Au(111) surface must be taken into account. [117]

7.4 EFM Measurements of Symmetric and Non-Symmetric Molecules

Having completed initial studies on alkanethiols, initial surface potential measurements of aromatic thiols were conducted using the same technique to provide an insight into the charge distribution for a conjugated molecular system (see Fig. 7.8). These experiments were devised to test the hypothesis that the symmetry of the molecular structure influences the surface potential.

The molecules used for this study were classified into two groups. Each set contained a symmetric molecule in addition to a non-symmetric variant. The first group consisted of xylydithiol (XYL: $C_8H_{10}S_2$) and benzyl mercaptan (BM: C_7H_8S). The second group was formed by tetramethyl-xylyl-dithiol (TMXYL: $C_{12}H_{18}S_2$) and pentamethylbenzyl mercaptan (PMBM: $C_{12}H_{18}S$).

Samples were prepared in a similar manor as the alkanethiols. The same solvents were used to deposit the symmetric and non-symmetric molecular set (such as TMXYL and PMBM). All TMXYL and PMBM samples were prepared by Bala Kasibhatal [118] and all benzyl mercaptan samples were prepared by Debasish Kuila [119] This helped to minimize any effects due to the polarities of different solvents.

The samples, used for this study, were also characterized by RAIRS. [120] The RAIRS data indicated that the benzyl mercaptan monolayer had a thickness of 4.5 Å. This suggests that the molecules are tilted by $\approx 30^o$ with respect to the z-axis since the length of the molecule is 5-6 Å. RAIRS data also revealed a thickness of 6.7 Å for the PMBM monolayer and a thickness of 8.0 Å for the TMXYL monolayer, indicating a vertical orientation of these molecules.

The results of the EFM measurements performed on the sets of molecules are summarized in Fig. 7.8. The molecules that have a symmetric structure, XYL and TMXYL, showed a small surface potential with respect to Au ($\approx +50$ and $\approx +16$ mV,

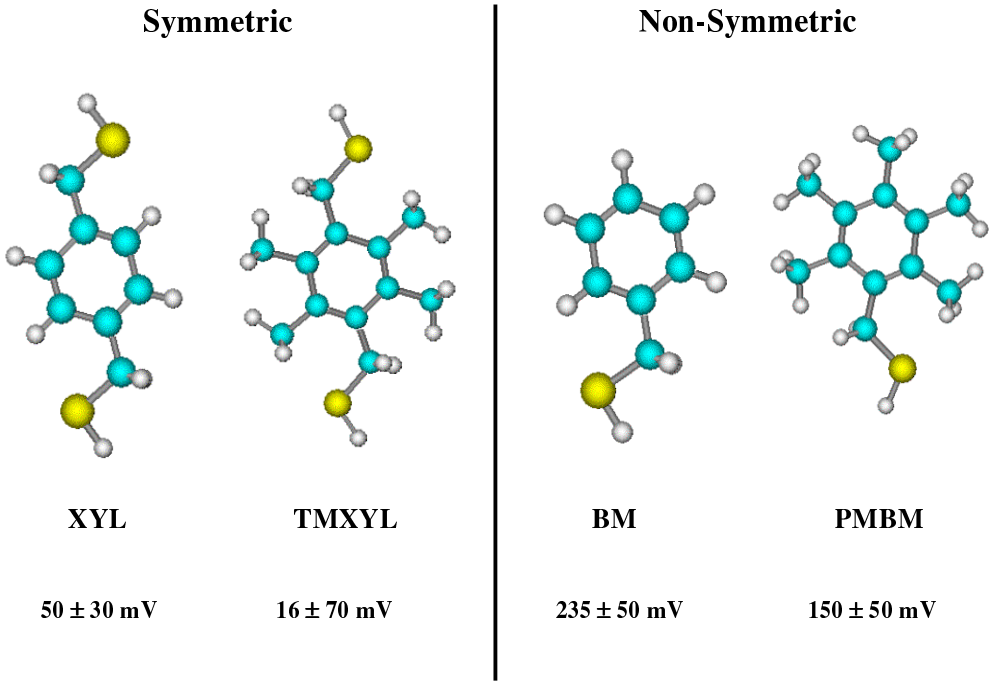

Figure 7.8. Symmetric and non-symmetric molecules used for the second part of this study. Surface potential measurements were made with respect to bare Au(111).

respectively), while the non-symmetric molecules showed significantly higher values. More significantly, benzyl mercaptan, which is equivalent to replacing one of the -CH_2SH groups of XYL with a hydrogen atom, yielded an average surface potential that is $\geq$ 200 mV with respect to gold. Similarly, replacement of one -CH_2SH of TMXYL with a -CH_3 group (PMBM) results in a large surface potential with respect to bare Au(111).

In order to understand these differences, we may consider the structures of these molecules. Examination of the chemical structures suggests that the dipole moment of XYL and TMXYL should be low or negligible due to the presence of high symmetry in the molecule. In other words, symmetry of the charge distribution will produce very insignificant dipole moments because of the orientations of the charge associated with chemical bonds. Attachment of one sulfur atom to a Au(111) site, as in the preparation of SAMs in both cases, should create a non-symmetric environment. However, the observed surface potentials are still quite small. The scenario of symmetry is disrupted in benzyl mercaptan and thus, produces a significant surface potential compared to XYL. Similar effects on surface potential are observed by comparing TMXYL with PMBM.

The calculated dipole moments of the molecules used for this portion of the study are displayed in Fig. 7.10. The dipole moments were calculated using the quantum chemistry software package: HyperChem 6.0 Professional Version^{TM}. [116] The dipole calculations ignored the molecule's interaction with the Au(111) surface. However, the calculations do support the trends observed in the data, which show that symmetric molecules have a significantly smaller dipole moment than non-symmetric molecules.

These initial measurements suggest that the surface produced by a monolayer of molecules is dominated by the molecular structure with a very weak influence from the charge associated with the sulfur-gold bond. These initial measurements support the simple physical picture of how the molecule's structural symmetry affects the relative magnitude of the molecule's surface potential. However, a more fundamental understanding is needed. Theoretical work is currently underway to understand the magnitude of these differences. [117]

7.5 Surface Potential Measurements of a Charge Transfer Complex

In recent years, conduction through SAMs of molecules has gained considerable interest. A great deal of progress has been made in understanding the nature of molecular conduction. [121–126] Previous work has shown that the molecule's conduction is greatly influenced by the location of the equilibrium Fermi level within the HOMO-LUMO gap. For a situation where the Fermi level is near the HOMO or LUMO levels, the conduction can be ballistic. If the Fermi level is located near the center of the HOMO-LUMO gap, the molecule's conduction will be considerably lower.

Based on the discussion above, the conduction of the molecule can be controlled by modifying the position of the Fermi level. The first convincing evidence of this principle was demonstrated by Kasibhatal *et al.* [127] They have shown that by using a charge transfer complex, the conductivity of a TMXYL molecule could be dramatically increased (switched "on"). Their initial report also indicates that this chemical gating process is reversible. The conductivity decreased (switched "off") substantially after the removal of the charge transfer complex.

The charge complex is formed by reacting a strong electron acceptor such as tetracyanoethylene (TCNE) with a SAM of TMXYL (an electron donor). For this situation it is thought that the electron donor has a HOMO level located below the Fermi level and the acceptor has a LUMO that also lies beneath the Fermi level. After the reaction, the acceptor will pull electrons out of the donor. This movement of charge hybridizes the energy levels of the molecular system. An increase in conduction occurs when one of the new hybridized energy levels coincide with the Fermi level. This effect has been experimentally verified using scanning tunneling microscopy (STM). [127]

Since the modification of molecular conduction can be regulated using the charge transfer complex, there should be significant change in the surface potential of the SAM. Therefore, surface potential measurements are useful for characterizing this molecular system prior to more complicated STM experiments.

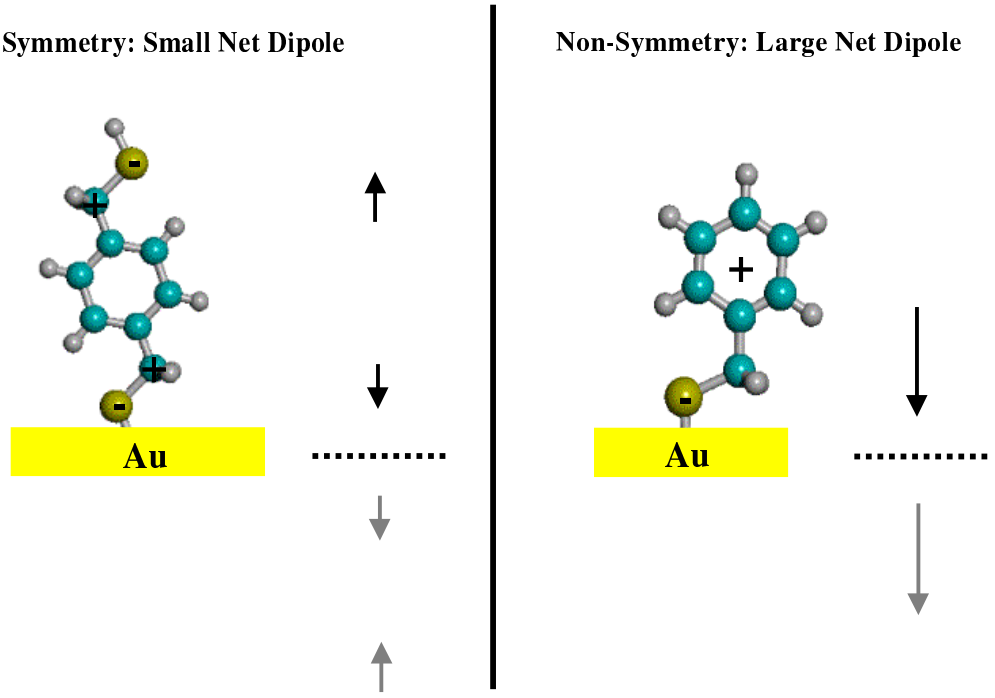

Figure 7.9. A simple physical model used to explain the dependence of surface potentials on molecular structure.

	Symmetric		Non-Symmetric	
Molecule:	**XYL**	**TMXYL**	**BM**	**PMBM**
Calculated Dipole (D):	**0.1**	**0.03**	**1.0**	**0.9**

Figure 7.10. Calculated dipole moments of XYL, TMXYL, BM, and PMBM. The calculations support the trends observed in the surface potential data.

For this study, the electrostatic surface potential was measured for samples of TMXYL, TMXYL+TCNE (charge transfer complex) and TMXYL after removal of the TCNE complex. These measurements were conducted on samples made in conjunction with the samples investigated by Kasibhatal *et al.* All measurements were referenced to a bare gold sample; thus, providing the electrostatic potential produced by the molecules.

7.5.1 Sample Preparation

Several TMXYL SAMs were prepared on a gold surface that had been annealed to form Au(111). The samples used in this study were prepared by Bala Kasibhatal. [118] The TMXYL samples were also characterized by RAIRS and ellipsometry. RAIRS measurement indicated a vertical orientation on the Au(111) surface.

To form the charge transfer complex, gold samples with a TMXYL SAM were soaked in a concentrated (0.1 M) CH_2Cl_2 solution of TCNE. Analysis of the RAIRS spectrum indicates that when the TCNE docks onto the TMXYL, both thiols of TMXYL bond to the Au(111) surface (Fig. 7.11 b). [120] Characterization conducted using ellipsometry and contact angle indicated a flat TMXYL+TCNE orientation.

The TCNE was removed from several samples by prolonged exposure to a solution of a strong electron donor, trimethyl tetrathiafulvalene. RAIRS measurements were conducted to determine the morphology of the TMXYL after the removal of the

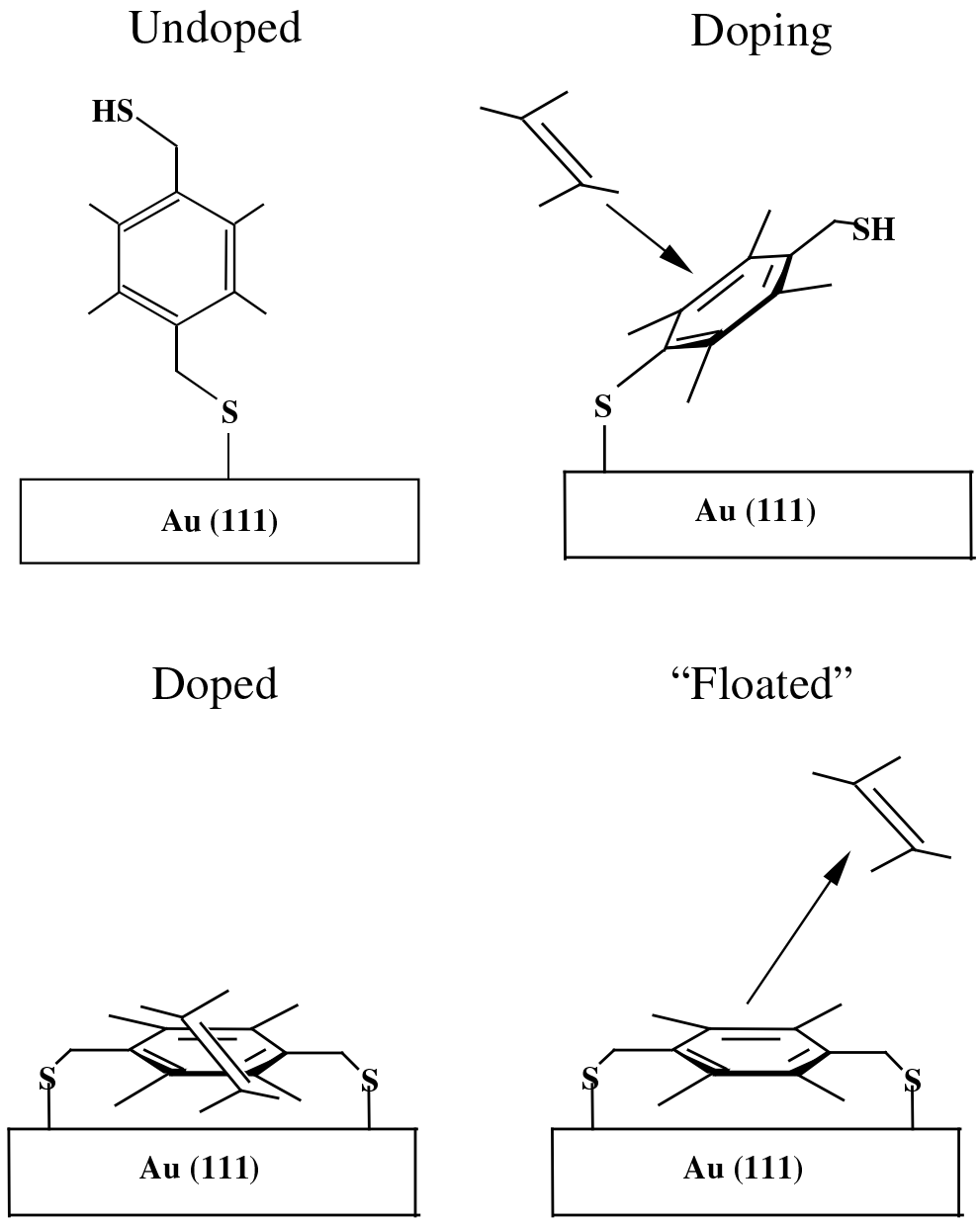

Figure 7.11. Orientation of TMXYL before and after the doping with a TCNE charge transfer complex.

Molecule	TMXYL	TMXYL+TCNE	TMXYL (TCNE Removed)
Surface Potential (mV)	20 ± 70	-142 ± 20	30 ± 50

Figure 7.12. Surface potential measurements of TMXYL SAMs with and without the TCNE charge transfer complex.

TCNE. These measurements indicated that both thiol end groups of the TMXYL remained bonded to the Au(111) (Fig. 7.11). These measurements also confirm the absence of TCNE. [127]

7.5.2 Measured Results

After sample formation and characterization, the electrostatic surface potential was measured for SAMs of TMXYL, TMXYL+TCNE and TMXYL after TCNE removal. Figure 7.12 displays the measurements taken with respect to a Au(111) reference. The surface potential of TMXYL is close to that of Au(111). As mentioned earlier, this is probably due to the molecule's symmetric structure.

However, measurements of the TMXYL with the addition of TCNE charge transfer complex displays a different behavior. These initial measurements indicate that when TCNE reacts with TMXYL, the surface potential of the charge complex is negative with respect to bare Au by -140 $\pm$ 20 mV. This negative surface potential is the result of the accumulation of negative charge near the top of the charge transfer complex. Since the TCNE is a strong π electron acceptor, there should be a negative charge displaced from the TMXYL and redistributed in the TCNE. Thus, these measurements support the chemistry which is responsible for the conduction mechanism.

In addition to the surface potential measurements of TMXYL and TMXYL+TCNE, measurements conducted on TMXYL after the removal of the TCNE also provides some insight into the chemistry that has taken place at the surface. The data in Fig. 7.12 shows that after the removal of TCNE, the surface potential of TMXYL returns to nearly the same value as before the TCNE reaction and thus, supports the complete removal of the TCNE after a prolonged exposure to a strong electron donor solution.

Overall this data tends to support the chemical mechanism responsible for doping the TMXYL molecule. The data reported here was acquired prior to the STM study of the systems, which also verified the effects of the charge transfer complex on molecular conduction. As can be seen, EFM can play an important role in characterizing such charge transferring molecular systems.

7.6 Additional Experimental Concerns for EFM Measurements on Molecules

The initial studies presented do tend to show the expected trends in the surface potential data. However, EFM measurements on molecules are very sensitive to many factors and the sample preparation techniques used for these investigations were prone to low yield. To develop a complete understanding of the surface potential produced by a SAM, these influencing factors will eventually need to be addressed.

Molecules	Dipole Moment (D)	Chem Formula
Water	1.85	H_2O
Ethanol	1.6	C_2H_6O
Terahydrofuran	1.7	C_4H_8O
Dichloromethane	1.6	CH_2Cl_2
Acetonitrile	3.9	CH_3CN

Figure 7.13. A list of solvents and water with their known dipole moments.

One major consideration is the quality of the Au(111) surface. If there are problems with the Au(111) surface, the monolayer will be affected. The nature of surface contamination must also be examined. Both of these issues can be answered using surface analysis techniques.

Additional attention must be paid to the effects of solvents and water on molecular surface potentials. Figure 7.13 is a list of solvents and water with their known dipole moments. The dipole moments of these substances tend to be larger than the dipoles of molecules used for these EFM studies. The solvents used for SAM formation do not chemically bond with gold. So it is unlikely that they will form a close-packed monolayer. However, if a fraction of the solvents were to become trapped in the SAM, they could cause an unwanted modification to the surface potential.

Figure 7.14 displays the surface potential of a well-oriented monolayer of ethanol as a function of packing density (using Eq. 7.6). The magnitude of the surface potential drops off dramatically as the surface density decreases. However, only a few molecules trapped in a 10 nm $\times$ 10 nm could have an effect on the potential produced by the self-assembled molecules.

In the case of a trap solvent, a study found in the literature has shown that solvent molecules do not embed themselves in the monolayers of long-chain alcohols formed on an air/water interface. [128] However this study was conducted using infrared spectroscopy and most likely lacks the ultra-high resolution needed to detect a low density of solvent molecules. If future endeavors are to continue with these experiments, ultra-high resolution scanning probe microscopy should be used to investigate the presence of embedded solvent molecules.

The effects of solvents may be responsible for the low sample yield. However, for the initial EFM measurements presented earlier, several ODT SAMs were prepared in ethanol, dichloromethane and acetonitrile. Even with the low sample yield, these samples produced surface potentials that were consistent (average surface potential of $+200 \pm 50$ mV with respect to Au(111)), providing some initial indication that solvents do not affect the measurements.

Ultimately EFM measurements on molecules should be conducted in a UHV environment. These initial studies were only conducted in air and dry nitrogen to build a fundamental level of confidence before moving to a more complicated situation of conducting experiments in a UHV environment. This was the primary motivation for the construction of the UHV AFM presented earlier.

The advantage of performing experiments in UHV is the lack of surface contamination. Additionally, recent reports in the literature have found that warming the SAMs to a temperature of 50^{o} C under a vacuum removes any unwanted physisorbed material from the surface of the monolayer. [129] This allows for better organization of the SAM.

The initial studies present here demonstrate the capabilities of using the EFM to probe SAM. Despite observed trends that support our initial understanding of the surface potentials produced by molecules adsorbed to metallic surfaces, more work must be done to more accurately measure the absolute magnitude of the surface potentials with respect to Au(111). To accomplish this requires advances in both sample characterization and environmental control.

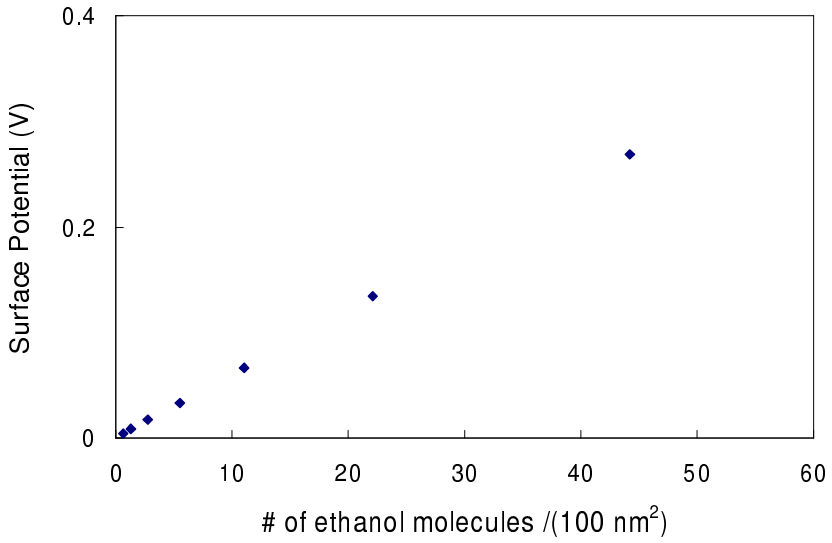

Figure 7.14. Surface potential produced by the dipole moment of ethanol as a function of packing density

8. CONCLUSIONS

Electrostatic force microscopy has been used to study the electrostatic force on a nanometer length scale. A series of initial experiments were conducted to test the principles of detecting the electrostatic force with current AFM technology. These experiments help to improve the understanding of how the EFM technique works.

In addition to the simple calibration experiments, an UHV AFM was constructed to provide a clean environment to perform future EFM experiments. The force detection sensor was based on a fiber optic interferometer design found in the literature. The system has been tested and found to be fully operational.

After obtaining a fundamental understanding for interpreting EFM data, several experiments were conducted to probe the electrostatic surface potential for several nanoscale systems. These experiments helped to provide insight into the fundamental mechanisms governing the electrical properties of nanoscale systems.

The surface potential of the unlinked array of 5 nm diameter DDT encapsulated gold clusters was measured using EFM techniques. The average surface potential of the array was found to be $+200 \pm 20$ mV with respect to the supporting gold substrate; thereby, providing some information on the relative difference between the work functions of the DDT encapsulated gold clusters and bulk gold. These initial studies indicate that the work function of the encapsulated clusters is lower than bulk gold. This information supports claims from the theory used to model the current conduction through nanocontact formed by a 5 nm diameter gold cluster tethered to a LTG:GaAs substrate.

The effects of striping the oxide layer off of LTG:GaAs samples were also studied using EFM. Observations were made of the LTG:GaAs's surface potential over a prolonged period of time after the removal of the surface oxide. These observations

indicated a transient behavior of the surface potential that had a characteristic time of $\approx$ 6-9 hrs. The behavior was found to be dependent on the environment, as well as, the agent used to remove the oxide layer. A simple surface model has been proposed to explain the behavior of the surface potential data. The model is based on the hypothesis that the surface potential is influenced by ions that remain on the LTG:GaAs surface after the stripping process. The surface potential of a heavily oxidized LTG:GaAs surface was measured over a nine day period using the same AFM tip. These measurements indicated that the surface potential of the LTG:GaAs was extremely stable. This stability makes LTG:GaAs a perfect choice to use as a reference for EFM measurements that require a comparison between different samples.

The final study using EFM techniques was based on measuring the surface potential of a SAM of molecules adsorbed onto a Au(111) surface. An initial level of confidence was developed by conducting surface potential measurements on alkanethiols. The dependence on the surface potential of alkanethiols on chain length was found to be consistent with published reports. Further, the study was extended to aromatic thiols, which show a strong dependence on the symmetry of the molecular structure.

In addition to EFM studies on alkanethiols and aromatic thiols, the modification of the surface potential due to chemical gating was also observed for TMXYL. These observations supported the observed conduction measurements and provided an alternative means to characterize the TMXYL SAM. These measurements also provided some initial insight to into how the EFM technique could be used for chemical sensing.

These initial studies are only in their infant stages. Additional experimental and theoretical work must be conducted in order to provide a better understanding of the current results and how to apply the results in future applications. However, these studies demonstrate the usefulness of the EFM. A wide variety of interesting and fundamental work can still be conducted on nanoscale systems that may become vital components of nanoscale electronics.

BIBLIOGRAPHY

BIBLIOGRAPHY

[1] C.D. Bain, E.B. Troughton, Y. Tao, J. Evall, G.M. Whitesides, and R.G. Nuzzo, J. Am. Chem. Soc. **111**, 321 (1989).

[2] C.D. Bain, J. Evall, and G.M. Whitesides, J. Am. Chem. Soc. **111**, 7155 (1989).

[3] M.D. Porter, T.B. Bright, D.L. Allara, and C.E.D. Chidsey, J. Am. Chem. Soc. **109**, 3559 (1987).

[4] Abraham Ulman, *An Introduction to Ultrathin Organic Films: from Langmuir Blodgett to Self-Assembly*, Academic Press, Boston, 1991.

[5] T. D. Krauss and L. E. Brus, Phys. Rev. Lett. **83**, 4840 (1999).

[6] G. Binnig, C.F. Quate, and Ch. Gerber, Phys. Rev. Lett. **56**, 930 (1986).

[7] P.J. De Pablo, E. Graugnard, B. Walsh, R.P. Andres, S. Datta, and R. Reifenberger, Appl. Phys. Lett. **74**, 323 (1999).

[8] M. S. Jean, S. Hudlet, C. Guthmann, and J. Berger, J. Appl. Phys. **86**, 5245 (1999).

[9] R. Gomez, A. Pak, A. Anderson, E. Burke, and A. Leyendecker, J. Appl. Phys. **83**, 6226 (1998).

[10] Kevin F. Brennan, *The Physics of Semiconductors With Applications To Optoelectronic Devices*, Cambridge University Press, New York, 1999.

[11] P.P. Craig and V. Radeka, Rev. Sci. Instrum. **41**, 258 (1970).

[12] Neil W. Ashcroft and N. David Mermin, *Solid State Physics*, Holt, Rinehart and Winston, New York, 1976.

[13] Lord Kelvin, Philos. Mag. **46**, 82 (1898).

[14] I. D. Baikie and P. J. Estrup, Rev. Sci. Instrum. **69**, 3902 (1989).

[15] I. D. Baikie, P. J. S. Smith, D. M. Porterfield, and P. J. Estrup, Rev. Sci. Instrum. **70**, 1842 (1999).

[16] I. R. Peterson, Rev. Sci. Instrum. **70**, 3418 (1999).

[17] S. Hamma and P. Cabarrocas, Rev. Sci. Instrum. **74**, 3218 (1999).

[18] F Rossi, Rev. Sci. Instrum. **63**, 3744 (1992).

[19] R. Reifenberger, unpublished results.

[20] Y. Leng et al., Appl. Phys. Let. **66**, 1264 (1995).

[21] M. Nonnenmacher, M.P. O'Boyle, and H.K. Wickramasinghe, Appl. Phys. Let. **58**, 2921 (1991).

[22] J. M. R. Weaver and D. Abraham, J. Vac. Sci. Technol. **B 9**, 1559 (1991).

[23] R. Reifenberger, Proposal (1996).

[24] J. W. Hong, K. H. Noh, S. Park, S. Kwun, and Z. Khim, Phys. Rev. B **58**, 5078 (1998).

[25] Roland Wiesendanger, *Scanning Probe Microscopy and Spectroscopy*, Cambridge University Press, New York, 1994.

[26] David M. Schaefer, PhD thesis, Purdue University, 1993.

[27] D. Schaadt, E. Yu, S. Sankar, and A. Berkowitz, Appl. Phys. Lett. **74**, 472 (1999).

[28] J. Jones, P. Bridger, O. Marsh, and T. McGill, Appl. Phys. Lett. **75**, 1326 (1999).

[29] T. Hochwitz, A. Henning, C. Levey, and C. Daghlian, J. Vac. Sci. Technol. **B 14**, 457 (1995).

[30] P. Rosenthal, E. Yu, R. Pierson, and P. Zampardi, J. Appl. Phys. **87**, 1937 (2000).

[31] F. Giessibl, S. Hembacher, H. Bielefeldt, and J. Mannhart, Science **289**, 4422 (2000).

[32] The Nano-Tec scanning force system is available from Nanotec^{TM}, FUAM, Edificio Rectorado, Universidad Autónoma de Madrid, E-28049 Madrid (Spain).

[33] PID feedback control theory and circuit design is available at http://newton.ex.ac.uk/teaching/CDHW/Feedback/SystemModel.html.

[34] Proportional-Integral-Derivative (PID) Fabrication available at http://mechatronics.me.vt.edu/_vti_bin/shtml.exe/book/Section3/PID.html/map.

[35] Basics of Proportional-Integral-Derivative Control by Vance vanDoren available at Contol Engineering *ONLINE*.

[36] C. A. Putman, B. G. De Grooth, N. F. Van Hulst, and J. Greve, J. Appl. Phys. **72**, 6 (1992).

[37] S. Fujisawa, M. Ohta, and T. Konishi, Rev. Sci. Instrum. **65**, 644 (1993).

[38] Laser Diode Module Model No. LDM1459/670/3 available from Imatronic.

[39] Quadrant Photodiode Part No. S4349 available from Hamamatsu Photonics K. K.

[40] Optical Cubes Part No. 03PBB011 available from Melles Griot.

[41] PELCO Conducting Silver 415 Cat. No. 16038 available from TED PELLA, INC.

[42] ThermoMicroscopes^{TM} Non-Contact Ultralever (ULNC-AUHW).

[43] ThermoMicroscopes^{TM} Non-Contact Piezolever (PLNC-SAMT).

[44] M. Tortonese, Appl. Phys. Lett. **62**, 831 (1992).

[45] UHVL Inchworm Motor available from Burleigh Instruments, Inc.

[46] D. Rugar, Appl. Phys. Lett **55**, 2588 (1989).

[47] P.J. Mulhern, Rev. Sci. Instrum. **62**, 1280 (1991).

[48] N. Nakatani and T. Oshio, J. Vac. Sci. Technol. B **12**, 1648 (1993).

[49] Charles Davis, Edward Carome, Martian Weik, Shaoul Ezekiel, and Robert Einzig, *Fiberoptic Sensor Technology Handbook*, Optical Technologies A Division of Dynamic Systems, Inc., 1986.

[50] Fiberoptic Sensor Technology Handbook is available at www.fiberoptic.com/handbook2.html.

[51] Fiberoptic laser diode Cat. No.HL1326CF/CN availabe from Thorlabs, INC.

[52] Dual Wavelength 1310 nm and 1550 nm 2x2 Coupler 50/50 Split Cat. No. 10202A-50 availabe from Thorlabs, INC.

[53] 80 μm dia. InGaAs Photodiode in TO-18 pkg. Part No. FD80W availabe from Fermionics Opto-Technology.

[54] Corning SMF-28 CPC6 Single-Mode Optical Fiber availabe from Thorlabs, INC.

[55] B. Gady, D. Schleef, R. Reifenberger, and D.S. Rimai, J. Adhesion **67**, 291 (1998).

[56] Barret Gady, PhD thesis, Purdue University, 1996.

[57] J.P. Cleveland, S. Manne, D. Bocek, and P.K. Hansma, Rev. Sci. Instrum. **64**, 403 (1993).

[58] O. Marti, S. Gould, and P. Hansma, Rev. Sci. Instrum. **59**, 836 (1988).

[59] Charles Kittel, *Introduction to Solid State Physics, 6th edition*, John Wiley and Sons, Toronto, 1986.

[60] H.C. Hamaker, Physica **4**, 1058 (1937).

[61] S. Belaidi, P. Girard, and G. Leveque, J. Appl. Phys. **81**, 1023 (1997).

[62] H. Hao, A. Baró, and J. Sáenz, J. Vac. Sci. Technol. **B 9**, 1323 (1991).

[63] B. Gady, D. Schleef, R. Reifenberger, D.S. Rimai, and L.P. DeMejo, Phys. Rev. B **53**, 8065 (1996).

[64] H. O. Jacobs, P. Leuchtmann, O. J. Homan, and A. Stemmer, J. Appl. Phys. **84**, 1168 (1998).

[65] A. Efimov and S. Cohen, J. Vac. Sci. Technol. **A 18**, 1051 (2000).

[66] B. Walsh, MS thesis, 2000, Purdue University (unpublished).

[67] S. Arnason, A. Rinzler, Q. Hudspeth, and A. Hebard, Appl. Phys. Lett. **75**, 2842 (1999).

[68] M. O'Boyle, T. Hwang, and H. Wickramasinghe, Appl. Phys. Lett. **74**, 2641 (1999).

[69] T. Lee, PhD thesis, 2000, Purdue University (unpublished).

[70] C. D. Thurmond, G. P. Schwartz, G. W. Kammlott, and B. Schwartz, Electrochem. Soc. **127**, 1366 (1980).

[71] W. Storm, D. Wolany, F. Schröder, G. Becker, B. Burkhart, L. Wiedmann, and A. Benninghoven, J. Vac. Sci. **15**, 1442 (1994).

[72] H. Gerischer, J. Vac. Sci. Technol. **15**, 1422 (1978).

[73] T. B. Ng, D. B. Janes, D. McInturff, and J. M. Woodall, Appl. Phys. Lett. **69**, 3551 (1996).

[74] M.R. Melloch, J.M. Woodall, E.S. Harmon, N. Otsuka, F.H. Pollak, D.D. Nolte, R.M. Feenstra, and M.A. Lutz, Annu. Rev. Mater. Sci. **25**, 547 (1995).

[75] R.M. Feenstra, J.M. Woodall, and G.D. Pettit, Phys. Rev. Lett. **71**, 1176 (1993).

[76] T. Holden and F. Pollak, Phys. Rev. B **58**, 7795 (1998).

[77] M.P. Patkar, T.P. Chin, J.M. Woodall, M.S. Lundstrom, and M.R. Melloch, Appl. Phys. Lett. **66**, 1412 (1995).

[78] T. Lee, N. P. Chen, J. Liu, R. P. Andres, D. B. Janes, E. H. Chen, M. R. Melloch, J. M. Woodall, and R. Reifenberger, Appl. Phys. Lett **76**, 212 (2000).

[79] N.-P. Chen, H. J. Ueng, D. B. Janes, J. M. Woodall, and M. R. Melloch, J. Appl. Phys. **88**, 309 (2000).

[80] Q. Xu and J. W. P. Hsu, J. App. Phys. **85**, 2465 (1999).

[81] Q. Xu, J. W. Hsu, J. Carlin, R. Sieg, J. Boeckl, and S. Ringel, Appl. Phys. Lett. **75**, 2111 (1996).

[82] S. Hong, D. B. Janes, D. McInturff, R. Reifenberger, and J. M. Woodall, Appl. Phys. Lett. **68**, 2258 (1996).

[83] LTG:GaAs samples were grown by M. R. Melloch and E. H. Chen (currently at Yale University) in the School of Electrical and Computer Engineering, Purdue University.

[84] LTG:GaAs smaples prepared by Marcus Batistuta from the School of Electrical and Computer Engineering, Purdue University.

[85] V. P. Roychowdhury, D.B. Janes, S. Bandyopadhyay, and X. Wang, IEEE Trans. on Electr. Dev. **43**, 1688 (1996).

[86] T. Lee, J. Liu, D.B. Janes, V.R. Kolagunta, J. Dicke, R.P. Andres, J. Lauterbach, M.R. Melloch, D. McInturff, J.M. Woodall, and R. Reifenberger, Appl. Phys. Lett. **74**, 2869 (1999).

[87] Ralph M. Nyffenegger, Reginald M. Penner, and Rainer Schierle, Appl. Phys. Lett. **71**, 1878 (1997).

[88] D.M. Schaefer, A. Patil, R.P. Andres, and R. Reifenberger, Appl. Phys. Lett. **66**, 1012 (1995).

[89] L. Hansen, A. Kuhle, A. Sorensen, and J. Bohr, Nanotechnology **9**, 337 (1998).

[90] C. Baur, A. Bugacov, B. Koel, A. Madhukar, and N. Montoya, Nanotechnology **9**, 360 (1998).

[91] T. Ramachandran, C. Baur, A. Bugacov, and A. Madhukar, Nanotechnology **9**, 237 (1998).

[92] Cluster smaples prepared by Jia Liu from the School of Chemical Engineering, Purdue University.

[93] P. Lorrain and D. Corson, *Electromagnetic Fields and Waves; Second Edition*, W.H. Freeman and Co., San Francisco, 1970.

[94] J. Liu, T. Lee, D. B.Janes, B. L. Walsh, M. R. Melloch, J. M. Woodall, R. Reifenberger, and R. P. Andres, Appl. Phys. Lett. **77**, 373 (2000).

[95] Jia Liu, PhD thesis, Purdue University, 2000.

[96] Cluster array smaples prepared by Jia Liu from the School of Chemical Engineering, Purdue University.

[97] C. Joachim, J. K. Gimzewski, and A. Aviram, Nature **408**, 541 (2000).

[98] H. G. Craighead, Science **290**, 1532 (2000).

[99] S. R. Quake and A. Scherer, Science **290**, 1536 (2000).

[100] A. Ulman, Chem. Rev. **96**, 1533 (1996).

[101] S. Hong, J. Bielefeld, R.P. Andres, and R. Reifenberger, in *Nanowires*, edited by P. Serena and N. Garcia, pages 351–72, Kluwer Academic, Dodrecht, 1997.

[102] S. Hong, R. Reifenberger, W. Tian, S. Datta, J. Henderson, and C. P. Kubiak, Superlattices and Microstructures **28**, 289 (2000).

[103] David J. Griffiths, *Introduction to Electrodynamics*, Prentice-Hall, INC., New Jersey, 1989.

[104] Information on RAIRS is available at www.uksaf.org/tech/rairs.html.

[105] Information on Ellipsometry is available at www.uskfa.org/tech/ellips.html.

[106] C.A. Alves, E.L. Smith, and M.D. Porter, J. Am. Chem. Soc. **114**, 1222 (1992).

[107] E. Barrena, S. Kopta, D. Ogletree, D. Charych, and M. Salmeron, Phys. Rev. Lett. **82**, 2880 (1999).

[108] E. Barrena, C. Ocal, and M. Salmerson, J. Chem. Phys. **111**, 9797 (1999).

[109] G. Y. Liu, S. Xu, and Y. Qian, Acc. Chem. Res. **33**, 457 (2000).

[110] Nonanethiols samples were prepared by Emilia Lugowska from the Department of Chemistry, Purdue University.

[111] S.D. Evans and A. Ulman, Chem. Phys. Lett. **170**, 462 (1990).

[112] C-10 calixarene was prepared by Steve Tripp and Alex Wei from the Department of Chemistry, Purdue University.

[113] J. Lu, E. Delamarche, L. Eng, R. Bennewitz', E. Meyer, and H. Guntherodt, Langmuir **15**, 8184 (1999).

[114] J. Lu, L. Eng, R. Bennewitz', E. Meyer, H. Guntherodt, E. Delamarche, and L. Scandelln, Surf. Interface Anal. **27**, 368 (1999).

[115] Gold substrates produced by Metallhandel SchröerGmbH, BuchentorstraBe 8 a, D 49536 Lienen, Germany.

[116] Calculations were performed by HyperChem Pro 6^{TM} software. Parameters for the Ab Initio calculations: basis set STO-3G, Fletcher-Reeves geometry optimization.

[117] Future calculations will be preformed by Sypriyo Datta's group in the School of Electrical and Computer Engineering, Purdue University.

[118] TMXYL and PMBM SAMs prepared by Bala Kasibhatla and Clifford Kubiak from the Department of Chemistry and Biochemistry, University of California San Diego, CA.

[119] Benzyl Mercaptan SAMs prepared by Debasish Kuila from School of Electrical and Computer Engineering, Purdue University.

[120] RAIRS characterization performed by Bala Kasibhatla from the Department of Chemistry and Biochemistry, University of California San Diego, CA.

[121] H.A. Biebuyck and G.M. Whitesides, Langmuir **9**, 1766 (1993).

[122] L.A. Bumm, J.J. Arnold, M.T. Cygan, T.D. Dunbar, T.P. Burgin, L. Jones II, D.L. Allara, J.M. Tour, and P.S. Weiss, Science **271**, 1705 (1996).

[123] D.J. Wold and C.D. Frisbie, J. Am. Chem. Soc. **122**, 2970 (2000).

[124] S. Datta, *Electronic Transport in Mesoscopic Systems*, Cambridge University Press, Cambridge, 1995.

[125] S. Datta, W. Tian, S. Hong, R. Reifenberger, J.I. Henderson, and C.P. Kubiak, Phys. Rev. Lett. **79**, 2530 (1997).

[126] M.A. Reed, C. Zhou, C.J. Muller, T.P. Burgin, and J.M. Tour, Science **278**, 252 (1997).

[127] Kasibhatla *et al.* manuscript in preparation.

[128] A. Gericke, J. Kutscher, and H. Hühnerfuss, Langmuir **9**, 2119 (1993).

[129] R. Gerlach, G. Polanski, and H.-G. Rubahn, Appl. Phys. A **65**, 375 (1997).

APPENDICES

APPENDICES

Appendix A: Summing Amplifier

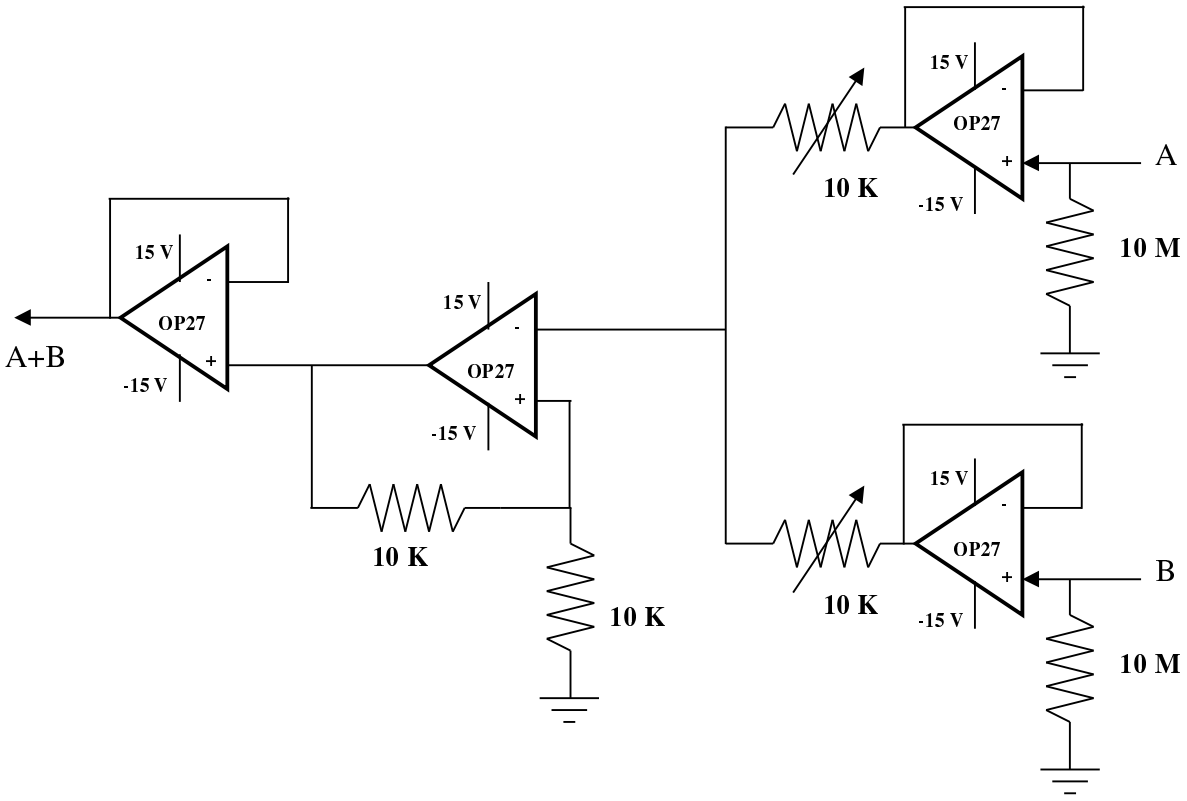

Figure A.1. Circuit schematic of summing amplifier used for EFM measurements.

Appendix B: Piezolever Detection

In recent years, a new type of force detection scheme has emerged. Rather than monitoring the cantilever deflection with an optical beam bounce sensor, this new approach integrates the sensor into the cantilever. This type of cantilever is formed from a thin piezoresistive layer of doped silicon surrounded by intrinsic silicon and oxide layers (see Fig. B.1). [44]

As the cantilever deflects, the resistance of the doped layer changes by $\triangle R$. The change in resistance is detected using a Wheatstone bridge circuit (Fig. B.2). By a first order approximation ($\frac{\triangle R}{R}$ is small), the output signal of Wheatstone bridge is given by

$$V_{out} = G V_{bias} \frac{\triangle R}{R} \quad . \tag{B.1}$$

The output of the circuit is proportional to the fractional change of the cantilever's resistance (which is proportional to the cantilever's deflection).

The primary source of noise in this circuit is due to thermal noise generated from the resistors. This noise has a rms amplitude of

$$V_n = \sqrt{4 k_B T R \triangle f} \quad . \tag{B.2}$$

Here k_B is the Boltzmann constant, R is the resistance, T is the temperature and $\triangle f$ is the bandwidth. Taking into account the rms noise from each resistor and the amplifier, the total rms noise for the entire detector (Wheatstone bridge circuit plus piezolever) is given by

$$V_n = G\sqrt{1/4[V_{n1}^2 + V_{n2}^2 + V_{n3}^2 + V_{n4}^2]} \quad . \tag{B.3}$$

By making the bridge resistors much smaller than piezolever's resistance, the noise due to bridge can be neglected:

$$v_n = G\sqrt{2 k_B T R \triangle f} \quad . \tag{B.4}$$

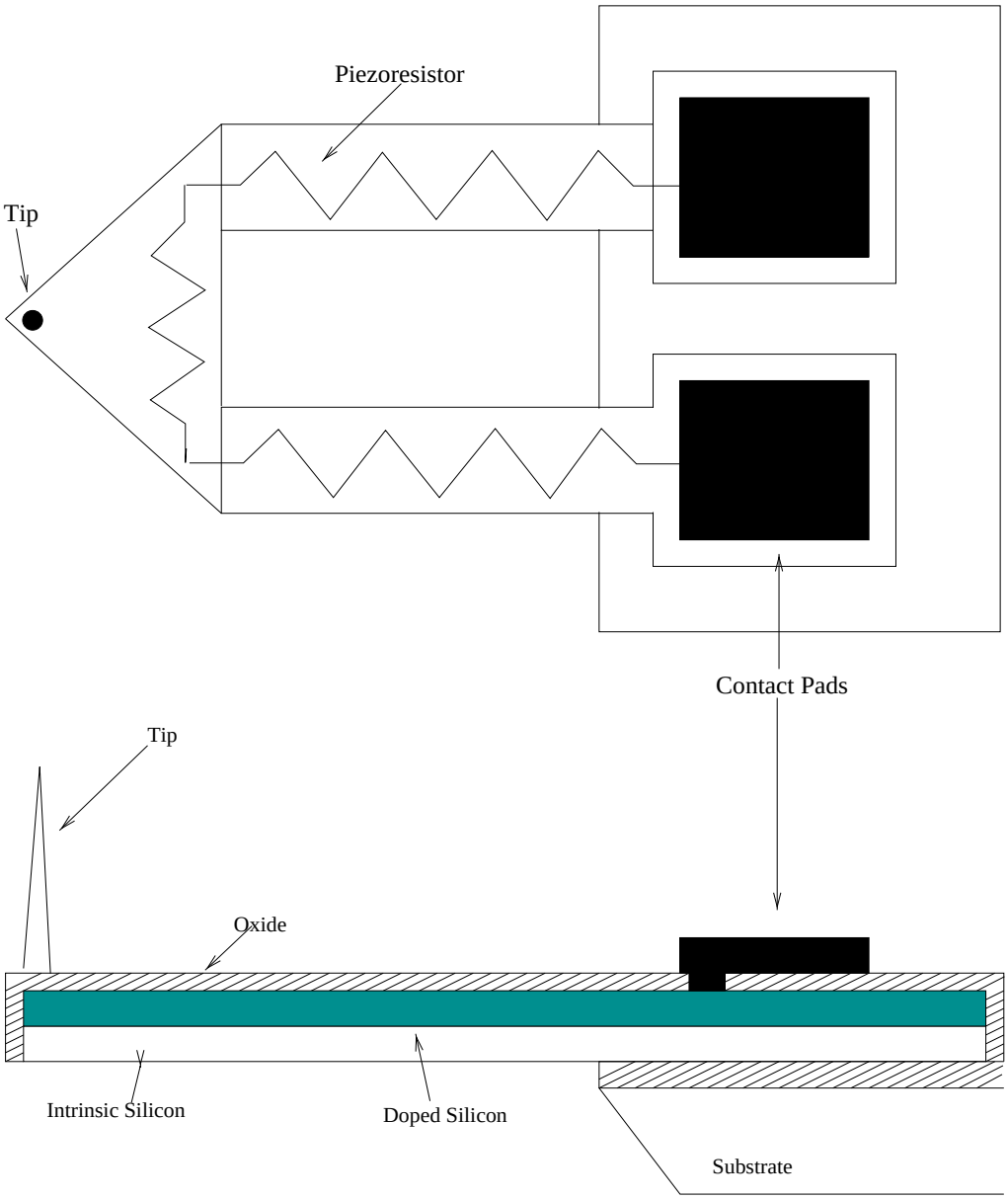

Figure B.1. A schematic diagram of a typical Piezolever construction.

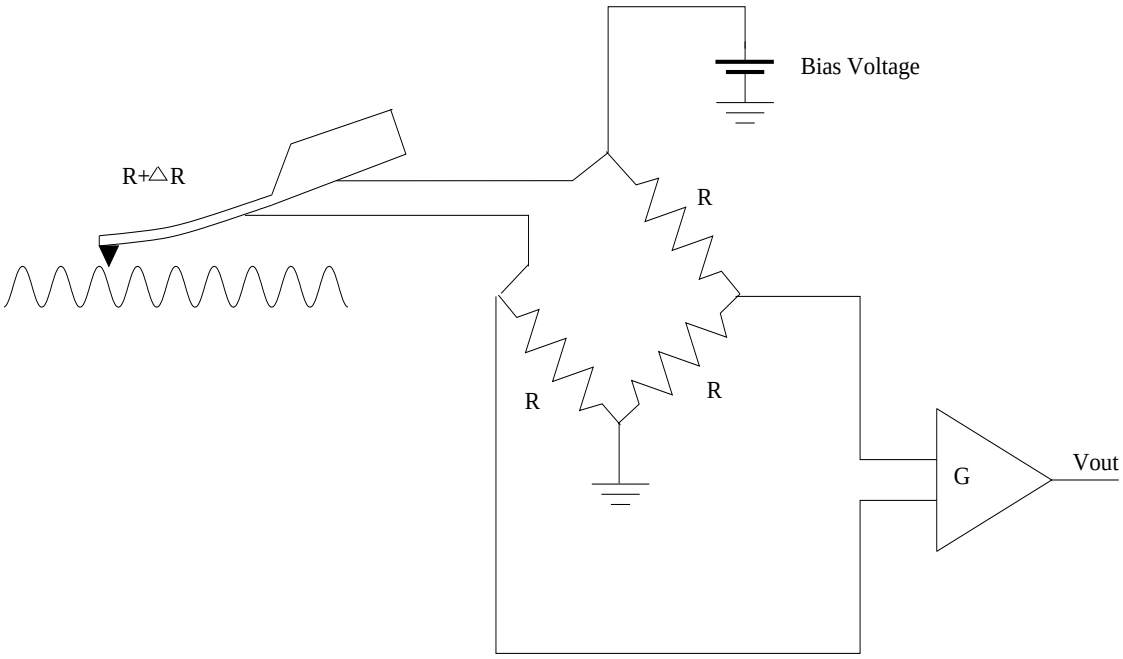

Figure B.2. Wheatstone bridge circuit used to detect small changes in the piezolever's resistance.

The noise of the piezoresistive cantilever determines the minimal detectable deflection. The minimal detectable resistance change is found by equating Eq. B.1 with Eq. B.4 and solving for the sensitivity $\frac{\triangle R}{R}$:

$$(\triangle R/R)_{min} = \frac{4\sqrt{2k_bTR\triangle f}}{V_{bias}} \quad . \tag{B.5}$$

The resistance change ($\frac{\triangle R}{R}$) is determined by the mechanical properties of the cantilever. From this mechanical analysis [44], one can relate the deflection and spring constant to the fractional change in resistance ($\frac{\triangle R}{R}$). Using this relationship, the deflection (z_{min}) is expressed as

$$z_{min} = \frac{1}{\beta}\left[\frac{8t^2w}{3\pi_L k}\right]\frac{\sqrt{2k_bTR\triangle f}}{V_{bias}} \quad . \tag{B.6}$$

Eq. B.6 indicates that as the spring constant increases, the minimal deflection decreases.

Even with the increased sensitivity to thermal drift, piezolevers have achieved atomic resolution on highly oriented polygraphite (HOPG). The images were obtained using cantilevers with spring constants of 100 N/m. [44]

Appendix C: Interferometer Hysteresis Code

C program used to calculate the distance traveled by a piezotube using the fiber optic interferometer monitor. The calculation is based on the model presented in Eq. 3.11.

```
/* ******************************************************
C code used to calculate the distance traveled by a piezotube.
Written by Steve Howell
****************************************************** */
#include <stdio.h>
#include <stdlib.h>
#include <math.h>
#include <string.h>
#define WL 1310      /* wave length of laser */
#define PI 3.14159
#define MAXLEN 600
void main(int argc,char *argv[]){
  int i,points,dummyint,flag1,flag2,flag3,flag4,flag5,flag6,flag7 ;
  char s1[20],s2[20] ;
  float dummy,vtube[MAXLEN],vout[MAXLEN],voutmax,voutmin,amp,offset,
        a[MAXLEN],b[MAXLEN] ;
  float amax,old,n1,n2,new,c[MAXLEN],d[MAXLEN];
  FILE *cfptr ;
  if (argc != 3){
     printf("Usage ./int1 filename points\n") ;
     exit(1) ;
     }
  points=atoi(argv[2]) ;
  if ((cfptr=fopen(argv[1],"r"))==NULL){
      printf("Could not open file !!!!!\n") ;
      exit(1) ;
      }
  else {
        fscanf(cfptr,"%s\n",s1) ;
        fscanf(cfptr,"%f\n",&dummy) ;
        fscanf(cfptr,"%s\n",s2) ;
        for(i=0 ; i<= (points-1) ; i++){
          fscanf(cfptr,"%d %f %f\n",&dummyint,&vtube[i],&vout[i]) ;
          }
   voutmax=0.0 ;
           for(i=0 ; i<=(points-1) ; i++){
       if(vout[i] > voutmax)
                voutmax=vout[i] ;
         }
  voutmin=vout[0] ;
  for(i=0 ; i <= (points-1) ; i++){
             if(vout[i] < voutmin)
        voutmin=vout[i] ;
     }
```

```
  printf("voutmax=%.1f\n",voutmax) ;
  printf("voutmin=%.1f\n",voutmin) ;
  printf("points=%d\n",points) ;
          amp=(voutmax-voutmin)/2 ;  /* finding amp */
          printf("amp=%.1f\n",amp) ;
          offset=(amp+voutmin) ;          /* find offest */
  printf("offset=%.1f\n",offset) ;
  for(i=0 ; i<=(points-1) ; i++){
             c[i]=(vout[i]-offset)/amp ;
             if (c[i]>1)
                c[i]=1 ;
             if (c[i]<-1)
                c[i]=-1 ;
             a[i]=acos(c[i]) ;      /* find distance */
             }
          amax=a[0] ;
          for(i=0 ; i<=(points-1) ; i++){
             if(a[i] > amax)
                 amax=a[i] ;
             }
          /*amax=PI ;*/
          old=((amax-a[0])+(amax-a[1])+(amax-a[2]) +(amax-a[3])+
                              (amax-a[4]))/5 ;

          flag1=1 ;
          flag2=1 ;
          flag3=0 ;
          flag4=0 ;
          flag5=0 ;
          flag6=0 ;
          flag7=0 ;
/* looking for inflection points */
        /* make linear */
          for(i=5; i<=(points-1); i++){
             new=((amax-a[i-4])+(amax-a[i-3])+(amax-a[i-2])+(amax-a[i-1])
                           +(amax-a[i]))/5 ;

             if (new < old && flag1==1){
       b[i]=a[i] ;
       /*printf("in 1\n") ;*/
     }
     if (new > old && flag2==1){
       b[i]=2*PI-a[i] ;
       flag1=0 ;
       flag3=1 ;
       /*printf("in 2\n") ;*/
     }
     if (new < old && flag3==1){
       b[i]=a[i]+2*PI ;
       flag2=0 ;
       flag4=1 ;
       /*printf("%d in 3\n",i) ;*/
     }
     if (new > old && flag4==1){
       b[i]=4*PI-a[i] ;
```

```
        flag3=0 ;
        flag5=1 ;
        /*printf("%d in 4\n",i) ; */
      }
      if (new < old && flag5==1){
        b[i]=a[i]+4*PI ;
        flag4=0 ;
        flag6=1 ;
        /*printf("%d in 5\n",i) ;*/
      }
      if (new > old && flag6==1){
        b[i]=6*PI-a[i] ;
        flag5=0 ;
        flag7=1 ;
        /*printf("%d in 6\n",i) ;*/
      }
      if (new < old && flag7==1){
        b[i]=6*PI+a[i] ;
        /*printf("%d in 7\n",i) ; */
      }
              old=new ;
             }
          for(i=0 ; i <= (points-1); i++){
             d[i]=(b[i]*WL)/(4*PI) ;
             printf("%d %.1f %.5f %.5f %.5f %5f\n",i,vtube[i],vout[i],
                    a[i],b[i],d[i]) ;
             /*printf("%d %.5f %.5f %.5f %.5f %.5f %.5f\n",i,vtube[i],
                    d[i],b[i],a[i],vout[i],c[i]) ;*/
             }
          fclose(cfptr) ;
        }
}
```

Appendix D: Resonance Response GPIB Code

GPIB C code used to control the EG&G 7280 lock-in amplifier when performing resonance response measurements.

MAIN C PROGRAM

```
/* ****************************************
ac7280.c
This program is used to measure the dF/dz as
a function of z.The software runs the EG&G 7280
lock-in amplifier.
The piezotube is controlled by DAC on the 7280.
Connect output of DAC to z gain.
Feed normal force signal into Ch A on 7280.
Connect cantilever's vibrator to 7280 oscillator.
Software written by Stve Howell
**************************************************** */

#include <stdio.h>
#include <string.h>
#include <stdlib.h>
#include <dos.h>
#include <ctype.h>
#include <conio.h>
#include <time.h>
#include <math.h>
#include "elockin6.h"
#include "filecon6.h"
#include "plot.h"
#define MAXPOINTS 512
#define MINPOINTS 50
#define MINFREQ 0.001
#define MAXFREQ 250000.0
#define DELAYTIME 100
#define DISPLAYTIME 1000000
#define TUBECAL -11.0

#define DEBUGM 0    /* set to 1 for trouble shoot */
void main(void)
{

char filename[7] ;
char ans1[1],ans2[1],ans3[1],ans4[1],ans5[1],ans6[1],ans7[1],ans8[1] ;
double startfreq ;
double resolution ;
double finalfreq ;
double freq[MAXPOINTS] ;
double amp[500] ;
double zstep ;
double psgain ;
double z ;
double zvolt ;
double dv ;
double n ;
double ampmax=0.0 ;
double oldfreqatmax=0.0 ;
double freqatmax=0.0,dumby1 ;
double tubedac=0.0 ;
int points,t,com,i,tmax ;
int savedata, shiftflag ;
```

```
int keystroke, average, filecount ;
enable_graph() ;
delay(DISPLAYTIME) ;
printf(" in enable-lockin \n") ;
delay(1000) ;
enable_lockin() ;
do{
  filecount=0 ;
  savedata=0 ;
  keystroke=0 ;
  do{
    /* getting scan parameters */
    clearscreen() ;
    printf("Save the curves output files? (y/n): ") ;
    fflush(stdout) ;
    scanf("%s",ans1);
  }while (ans1[0] != 'y' && ans1[0] !='n' && ans1[0] !='Y' && ans1[0] !='N');
  if ((ans1[0]=='y') || (ans1[0]=='Y')){
    do{
      printf("Enter file name (eight characters max) : ") ;
      fflush(stdout) ;
      scanf("%s", filename) ;
    } while(strlen(filename) > 8);
    savedata=1 ;
    strcat(filename,".frq") ;
  }
  do{
    printf("Enter starting frequency ( in Hz): ") ;
    fflush(stdout) ;
    scanf("%lf",&startfreq) ;
  }while (!(startfreq > MINFREQ && startfreq < MAXFREQ));
  printf("Enter number of data points (50-500): ");
  fflush(stdout) ;
  scanf("%d",&points);
  if (points < MINPOINTS)
    points=MINPOINTS ;
  if (points > MAXPOINTS)
    points=MAXPOINTS ;
  do{
    printf("Enter the resolution (min .001 Hz): ") ;
    fflush(stdout) ;
    scanf("%lf",&resolution) ;
    } while(resolution < .001);
  printf("Enter the number of averages(1-10): ") ;
  fflush(stdout) ;
  scanf("%d",&average) ;
  if (average < 1)
    average=1 ;
  if (average > 10)
    average=10 ;
  shiftflag=0 ;
  printf("Shift the starting frequency (y/n): ") ;
  fflush(stdout) ;
  scanf("%s",ans5) ;
```

```
  if (ans5[0]=='y' || ans5[0]=='Y')
   shiftflag=1 ;
  finalfreq=startfreq+points*resolution ; /* calculate final freq */
  printf("\n\n*************************************\n\n");
  printf("The scan resolution is %.2lf Hz\n",resolution) ;
  printf("The final frequency is %.2lf Hz\n",finalfreq) ;
  if(DEBUGM){
    printf("Average = %d \n", average) ;
    printf("Number of points = %d \n", points) ;
    printf("Shift freq = %s \n", ans5) ;
    }
  printf("\n*************************************\n\n");
  if (finalfreq > MAXFREQ)
    printf("Final frequency is to large !!!! \n");
  else{
    /* starting main loop */
    printf("Do the scan ? (y/n): ") ;
    fflush(stdout);
    scanf("%s",ans4) ;
    if (ans4[0]=='y' || ans4[0]=='Y') {
      filecount=0 ;
      z=0 ;
      zvolt=0 ;
      tubedac= set_ztube(zvolt) ;  /* putting z voltage on piezotube */
      printf("dac1 = %.1lf \n",tubedac) ;
      oldfreqatmax=0.0 ;
      do {
printf("\nEnter dz step size in nanometers: ") ;
fflush(stdout) ;
scanf("%lf",&zstep) ;
if (zstep<0 )
  zstep=0 ;
if (zstep>1000)
  zstep=1000 ;
printf("Enter the power supply gain : ") ;
scanf("%lf",&psgain) ;
if (psgain < 1)
 psgain=1 ;
dv=floor(zstep/((TUBECAL/1000)*psgain)) ;  /* cal tube step */
zstep=(TUBECAL/1000)*psgain*dv ;
if(DEBUGM){
  printf("Tube Calibration = %lf \n", TUBECAL) ;
  printf("Power supply gain = %lf \n",psgain) ;
  printf("zstep = %lf \n", zstep) ;
  printf("Voltge step = %lf \n", dv) ;
}
for(t=0,n=0 ; t<=(points-1); t++,n++)
  freq[t]=startfreq+n*resolution ;    /* cal freqs */
do{
  printf("\n\n**** SCANNING ****\n") ;
  set_freq(startfreq) ;                /* setting freq */
  for(t=0; t<=(points-1) ;t++)
  amp[t]=0.0 ;
```

```
  /* dumby1=0.0 ; */
  for(t=0; t<=(points-1) ;t++){
    set_freq(freq[t]) ;
    delay(1000) ;
    for(i=0,n=0;i<=(average-1);i++,n++){
amp[t]=amp[t]+read_mag2() ;   /* read signal amp */
if(DEBUGM)
  printf("amp[%d,%d] = %lf \n",t,n,amp[t]) ;
}
amp[t]=amp[t]/n ;             /* finding average */
if(DEBUGM)
  printf("averge amp[%d] = %lf \n",t,amp[t]) ;
    }
   if(DEBUGM){
     printf("out of loop\n") ;
     delay(DISPLAYTIME) ;
     }
   clearscreen() ;
   plot(freq,amp,points,"Hz","Amp") ; /* plot data */
   delay(DISPLAYTIME) ;
   keystroke=kbhit() ;
   if (savedata==1){
 save_datal(filename,filecount,freq,amp,points,"Freq(Hz)","Amp",zvolt,tubedac) ;
   printf("\nLoop %d saved\n",filecount) ;
     }
   printf("Z position: %.0lf A\n",z) ;
     printf("dac1 = %.01lf mV\n",tubedac) ;
           /* shift freq range */
   if (shiftflag==1){
     ampmax=0.0 ;
     for(t=0; t<=(points-1) ; t++){
       if (amp[t] > ampmax){
       ampmax=amp[t] ;
       tmax=t ;
       }
      }
    freqatmax=freq[tmax] ;
    printf("\nOld max @=%.0lf\n",oldfreqatmax) ;
    printf("Old init freq=%.0lf\n",startfreq) ;
    if ((filecount > 0) && ((oldfreqatmax-freqatmax) > 0)){
      startfreq=startfreq-fabs(freqatmax-oldfreqatmax) ;
      for (t=0,n=0; t<=(points-1) ; t++,n++)
      freq[t]=startfreq+n*resolution ;
      }
    oldfreqatmax=freqatmax ;
    if(DEBUGM)
     printf("New starting freq = %lf \n", startfreq) ;
   }
   z=z+zstep ;              /* new tube position */
   zvolt=zvolt+dv ;
   tubedac=set_ztube(zvolt) ;
   filecount++ ;
   if (keystroke != 0){
```

```
printf("\n\nPaused!!\n") ;
printf("Continue (y/n): ") ;
fflush(stdout) ;
scanf("%s",ans8) ;
if (ans8[0]=='y' || ans8[0]=='Y')
keystroke=0 ;
      }
        }while(filecount <= 99 && keystroke==0) ;
/* delay(DISPLAYTIME) ; */
clearscreen() ;
printf("Change the z step size (y/n): ") ;
        fflush(stdout) ;
scanf("%s",ans6) ;
      }while(ans6[0]=='y' || ans6[0]=='Y') ;

      /* moving tip towards sample */
      if (zstep != 0) {
 printf("Move the tip (y/n): ") ;
 fflush(stdout) ;
 scanf("%s",ans7) ;
 if (ans7[0]=='y' || ans7[0]=='Y'){
    printf("Moving !!!!\n") ;
    printf("\n\n*****************************\n") ;
    printf("Keys: f=forward, b=backward, q=stop\n") ;
    printf("*****************************\n\n") ;
    do{
 printf("Current z position (angtroms) from starting point is: %.2lf\n",z) ;
 printf("Voltage to the power supply (mV): %.0lf\n",zvolt) ;
fflush(stdout) ;
com=getch() ;
if (com=='q'|| com=='Q')
printf("stopped\n") ;
if (com=='f' || com=='F'){
  z=z+zstep ;
  zvolt=zvolt+dv ;
  printf("Moving forward.\n") ;
  if (zvolt < 10000 ) {
    printf("setting tube \n") ;
    tubedac=set_ztube(zvolt) ;
    printf("dac1 = %.00lf mV\n",tubedac) ;
    }
  else
    printf("Out of range.\n") ;
}
if (com=='b' || com=='B'){
  printf("Moving back.\n") ;
  z=z-zstep ;
  zvolt=zvolt-dv ;
  if (zvolt > -10000){
    printf("setting tube \n") ;
    tubedac=set_ztube(zvolt) ;
    printf("dac1 = %.00lf mV\n",tubedac) ;
    }
  else
    printf("Out of range.\n") ;
```

```
 }
      }while(com != 'q' && com !='Q') ;
 }
}
       }
      }

if(savedata == 1){
fflush(stdout) ;
close_data(filename,zvolt) ;
}
set_ztube(0) ;
set_freq(startfreq) ;
printf("Another scan (y/n=quit): ") ;
fflush(stdout) ;
scanf("%s",ans3) ;
}while(ans3[0]=='y' || ans3[0]=='Y') ;
disable_lockin() ;
disable_graph() ;
exit(0) ;
}
SUPPORT C FILES
#######################################################
/* ************************************************
elockin.c and elockin.h
Control commands for EG&G 7280 lock-in
Written by Steve Howell
************************************************** */

#include <stdio.h>
#include <stdlib.h>
#include <string.h>
#include <dos.h>
#include <ctype.h>
#include <conio.h>
#include <time.h>
#include <math.h>
#include "decl.h"

#define DEBUGL 0

int egg7280 ;
void enable_lockin(void){
  int card ;
  char n1[5] = "GPIB0" ;
  char s[100];
  printf("\nInitializing GPIB card\n") ;
  delay(1000) ;
  card = ibfind("GPIB0") ;
  delay(1000);
  printf("GPIB card = %d\n",card) ;
  delay(1000) ;
  if (card < 0){
  printf("GPIB error: could not open card !!!!!!\n") ;
  ibonl(card,0) ;
  exit(EXIT_FAILURE) ;
```

```
  }
  egg7280=ibfind("EGG7280") ;
  delay(100) ;
  printf("EG&G 7280 lockin = %d\n\n\n",egg7280) ;
  if (egg7280 < 0){
  printf("GPIB error: could not open the lock-in\n") ;
  ibonl(egg7280,0) ;
  exit(EXIT_FAILURE) ;
  }
  ibclr(egg7280) ;
  delay(100) ;
  ibwrt(egg7280,"msk 128",7) ;
  delay(100) ;
  /* ibwrt(egg7280,"tc 9",4) ;
  delay(100) ;
  ibwrt(egg7280,"ie 0",strlen("ie 0")) ;
  delay(100) ;
  ibwrt(egg7280,"vmode 1",7) ;
  delay(100) ;
  ibwrt(egg7280,"automatic 1",11) ;
  delay(100) ;
  ibwrt(egg7280,"lf 0",4) ;
  delay(100) ;
  ibwrt(egg7280,"fet 1",5) ;
  delay(100) ;
  ibwrt(egg7280,"oa. 1.010",9) ;
  delay(100) ;
  ibwrt(egg7280,"of. 1000.0",10) ;
  delay(100) ;
  ibwrt(egg7280,"aqn",3) ;
  delay(100) ; */
}
void disable_lockin(void){
  ibonl(egg7280,0) ;
  printf("disable lockin \n") ;
}

void set_freq(double initfreq){
  char txt1[30],tmp1[30] ;
  ibclr(egg7280) ;
  strset(txt1,'\0') ;
  strcat(txt1,"of. ") ;
  gcvt(initfreq,12,tmp1) ;
  strcat(txt1,tmp1) ;
  ibwrt(egg7280,txt1,strlen(txt1)) ;
  if(DEBUGL){
  printf("setting freq \n") ;
  printf("String to lockin= %s \n", txt1) ;
}
  delay(10) ;
  ibclr(egg7280) ;
}

double set_ztube(double zvolts){
```

```
  char txt1[30],tmp1[30],txt2[30],txt3[30]="100" ;
  double ttt ;
  /* printf("zvolts=%.0lf\n", zvolts) ;   */
  ibclr(egg7280) ;
  delay(50) ;
  strset(txt1,'\0') ;
  strcat(txt1,"dac1 ") ;
  gcvt(zvolts,6,tmp1) ;
  strcat(txt1,tmp1) ;
  ibwrt(egg7280,txt1,strlen(txt1)) ;
  if(DEBUGL) {
  printf("Setting tube voltage= %s \n",txt1) ;
}
  delay(100) ;
  ibclr(egg7280) ;
  ibwrt(egg7280,"dac1 ",strlen("dac1 ")) ;
  /* ibwait(egg7280,TIMO|RQS) ; */
  delay(200) ;
  ibrd(egg7280,txt3,10L) ;
  txt3[ibcnt]='\0' ;
  if (DEBUGL) {
printf("txt3 = %s \n",txt3) ;
}
  return atof(txt3);
  ibclr(egg7280) ;
}

double read_mag1(void){
  char strdat[20]="100" ;
  /*ibclr(egg7280) ; */
  ibwrt(egg7280,"mag1",strlen("mag1")) ;
  /* ibwait(egg7280,TIMO|RQS) ; */
  delay(200) ;
  ibrd(egg7280,strdat,10L) ;
  strdat[ibcnt]='\0' ;
  if(DEBUGL)
  printf("Mag1. =%s\n",strdat) ;
  return atof(strdat) ;
}
double read_mag2(void){
  char strdat[20]="100" ;
  ibclr(7280) ;
  ibwrt(egg7280,"mag2",4) ;
  /*  ibwait(egg7280,TIMO|RQS) ; */
  delay(200) ;
  ibrd(egg7280,strdat,10L) ;
  strdat[ibcnt]='\0' ;
  if(DEBUGL)
  printf("Mag2. =%s\n",strdat) ;
  return atof(strdat) ;
}
double read_adc1(void){
```

```
char strdat[20]="200" ;
        ibclr(egg7280) ;
ibwrt(egg7280,"adc1",4) ;
/* ibwait(egg7280,TIMO|RQS) ; */
delay(1000) ;
ibrd(egg7280,strdat,10L) ;
strdat[ibcnt]='\0' ;
if(DEBUGL)
printf("ADC1 = %s \n", strdat) ;
return atof(strdat) ;
        ibclr(egg7280) ;
}
void setdac(double volts){
  char txt1[30],tmp1[30],txt2[30] ;

  ibclr(egg7280) ;
  delay(50) ;
  strset(txt1,'\0') ;
  strcat(txt1,"dac2 ") ;
  gcvt(volts,6,tmp1) ;
  strcat(txt1,tmp1) ;
  ibwrt(egg7280,txt1,strlen(txt1)) ;
  if(DEBUGL) {
  printf("volts=%.0lf\n", volts) ;
  printf("Setting  voltage= %s \n",txt1) ;
}
  delay(100) ;
  ibclr(egg7280) ;
}
void setamp(double amp){
  char txt1[30],tmp1[30],txt2[30] ;

  ibclr(egg7280) ;
  delay(50) ;
  strset(txt1,'\0') ;
  strcat(txt1,"oa ") ;
  gcvt(amp,6,tmp1) ;
  strcat(txt1,tmp1) ;
  ibwrt(egg7280,txt1,strlen(txt1)) ;
  if(DEBUGL) {
  printf("amp=%.0lf\n", amp) ;
  printf("Setting amp voltage= %s \n",txt1) ;
}
  delay(100) ;
  ibclr(egg7280) ;
}
#########################################################
/* ************************
elockin6.h  header file
************************ */

void enable_lockin(void) ;
void disable_lockin(void) ;
```

```
void set_freq(double) ;
double set_ztube(double) ;
double read_mag1(void) ;
double read_mag2(void) ;
double read_adc1(void) ;
void setdac(double) ;
void setamp(double) ;
################################################
/* ********************************************
plot.c and plot.h
Plot software used in ac7280 code.
The Egavga.bgi file needs to be in same directory as plot.c
Written by Steve Howell.
******************************************** */
#include <stdio.h>
#include <stdlib.h>
#include <math.h>
#include <graphics.h>
#include <conio.h>
#include <dos.h>
#define MAXLEN 600
#define XORIG 160
#define YORIG 350
#define YGRAPHMAX 5
#define XGRAPHMAX 610
#define DEBUGP 0
void enable_graph(void){
  int g_driver=DETECT, g_mode ,error, mode ;
  char modename[80] ;
  initgraph(&g_driver,&g_mode,"") ;
  error= graphresult() ;
  mode=getgraphmode() ;
  cleardevice() ;

  if(DEBUGP){
printf("modename = %s \n",getmodename(mode)) ;
printf("error = %i \n",error) ;
printf("driver =%i \n",g_driver);
printf("mode = %i \n",g_mode) ;
}
}
void plot(double hort[],double vert[],int pts,char xlable[],
char ylable){
double xmin=0,ymin=0,xmax=0,ymax=0,j ;
double x[MAXLEN],y[MAXLEN], xscale, yscale ;
int n, nmax ;
if(DEBUGP)
  for (n=0; n<=2 ; n++)
  printf("in plot\n") ;
if (pts > MAXLEN)
pts=MAXLEN ;
for (n=0; n<=(pts-1) ; n++ ){
  x[n]=hort[n] ;
  y[n]=vert[n] ;
  }
```

```
xmin=x[0] ;
ymin=y[0] ;
for (n=0; n<=(pts-1); n++){
if (x[n] < xmin)
 xmin=x[n] ;
if (y[n] < ymin)
 ymin=y[n] ;
}
for (n=0; n<=(pts-1); n++){
x[n]=x[n]-xmin ;
y[n]=y[n]-ymin ;
}
  for (n=0; n<=(pts-1); n++){
if (x[n] > xmax)
xmax=x[n] ;
if (y[n] > ymax){
ymax=y[n] ;
nmax=n ;
}
}
  xscale= (XGRAPHMAX- XORIG)/xmax ;
  yscale= (YORIG - YGRAPHMAX)/ymax ;

  for (n=0; n<=(pts-1); n++){
x[n]=x[n]*xscale ;
y[n]=y[n]*yscale ;
}
  line(XORIG,YGRAPHMAX,XORIG,YORIG) ;
  line(XORIG,YORIG,XGRAPHMAX,YORIG) ;
  for (n=0; n<=(pts-1); n++)
  putpixel(x[n]+XORIG,YORIG-y[n],15) ;
  for (j=YGRAPHMAX; j<=YORIG; j++)
  putpixel(x[nmax]+XORIG,j,12) ;
  printf("Max @ %.2lf %s\n",hort[nmax],xlable) ;
  /* delay(2000) ; */
}
void clearscreen(void){
 /* cleardevice() ; */
 clrscr() ;
 clearviewport() ;
}
void disable_graph(void) {
closegraph() ;
}
#######################################
/* ***************************
header file for plot.h
**************************** */
void enable_graph(void) ;
void plot(double [],double [],int,char [],char[]) ;
void disable_graph(void) ;
void clearscreen(void) ;
#############################################################
```

```
/* ****************************************
filecon.6 and filecon6.h
data recording software
Written by Steve Howell
**************************************** */
#include <stdio.h>
#include <string.h>
#include <stdlib.h>
#include <math.h>
#include <dos.h>
#include <ctype.h>
#include <conio.h>
#include <time.h>
#include <io.h>
#include <fcntl.h>

void save_data(char name[],char ext[],double filenum,
double f[],double a[],int pts,char s1[],char s2[],double z){
   char tmp[20] ;
   char scan[20] ;
   FILE *cfptr ;
   int i ;
   strset(tmp,'\0') ;
   strset(scan,'\0') ;
   strcat(scan,name) ;
   gcvt(filenum,4,tmp) ;
   if (filenum < 10){
      strcat(scan,"0") ;
      strcat(scan,tmp) ;
      strcat(scan,ext) ;
      }
   else {
      strcat(scan,tmp) ;
      strcat(scan,ext) ;
      }
   printf("Opening %s\n",scan) ;
   if((cfptr=fopen(scan,"w"))==NULL)
       printf("File could not be opened !!!\n") ;
   else{
       fprintf(cfptr,"%d\n",cfptr) ;
       fprintf(cfptr,"Z_position_(Angstrom):\n") ;
       fprintf(cfptr,"%.2lf\n",z) ;
       fprintf(cfptr,"%s,%s,%s\n","Point",s1,s2) ;
       for (i=0 ; i<=(pts-1) ; i++)
  fprintf(cfptr,"%d %.2lf %.4lf\n",i,f[i],a[i]) ;
       fclose(cfptr) ;
       }
}
void save_datal(char name[],int loop,double f[],double a[],
int pts,char s1[],char s2[],double zvolt,double fdac){
   int i ;
   FILE *cfptr ;

   if((cfptr=fopen(name,"a"))==NULL){
        delay(10000) ;
        printf("File could not be open !!!!\n") ;
```

```
        }
   else{
         fprintf(cfptr,"Loop:\n") ;
         fprintf(cfptr,"%d\n",loop) ;
         fprintf(cfptr,"Z_Tube_Volatage_(mV):\n") ;
         fprintf(cfptr,"%.2lf\n",zvolt) ;
 fprintf(cfptr,"Dac1:\n") ;
 fprintf(cfptr,"%.1lf\n",fdac) ;
         fprintf(cfptr,"%s,%s,%s\n","Point",s1,s2) ;
         for (i=0 ; i<=(pts-1) ; i++)
            fprintf(cfptr,"%d %.2lf %.4lf\n",i,f[i],a[i]) ;
         fclose(cfptr) ;
         fcloseall() ;
         }
}
void close_data(char name[],double par){
   FILE *cfptr ;
   /*printf("name=%s\n",name) ; */
   if((cfptr=fopen(name,"a"))==NULL){
       delay(10000) ;
       printf("File could not be open !!!!\n") ;
       }
    else{
       fprintf(cfptr,"loop:\n") ;
       fprintf(cfptr,"999\n") ;
       fprintf(cfptr,"Final_tube_voltage_(mV):\n") ;
       fprintf(cfptr,"%.2lf\n",par) ;
       fclose(cfptr) ;
       }
##########################################################
/* ***********************************
filecon6.h header file
************************************ */
/*void open_file(char [],char []) ; */
void save_data(char [],char[],double ,double [] ,double [],
int,char [],char [],double) ;
void save_datal(char [],int,double [],double [],
int,char [],char [],double,double) ;
void close_data(char [],double) ;
```

Appendix E: Trench Convolution Code

C code used to simulate the electrostatic forces acting on a cantilever beam over a split electrode configuration.

```
/* EMF model of cantilever beam moving over to electrodes */
/* separated by a distance l. */
/* The cantilever is modeled by a simple parallel plate cap. */
/* The field between the electrodes is ignored. */
/* This programs finds the tip voltage needed to minimize */
/* the force on the cantilever. */
/* Written by Steve Howell */
#include <stdio.h>
#include <math.h>
#define SIZE 40000 /* size of electrode config in nm */
main() {
float vtip[SIZE], pos[SIZE], h[SIZE], x, L, l, a, b, A1, A2, v1, v2, w ;
int c , i ;
/* using force equation of parallel plate cap -1/2 Eo Area/z^2 */
c=0 ; /* counting ints */
i=0 ;
L=1500 ; /* length of the electrodes in nn */
l=400 ;  /* separation distance of electrodes */
b=1000 ; /* width of cantilever plate */
a=1000 ; /* length of cantilever plate */
w=a/2 ;  /* Tip located in the mid of cantilever */
  /* cantilever-sample separation distance */
  /* the depth of the trench between two electrodes */
 /* when scanning in trench */
  /* init height above electrode */
v1=1 ;   /* voltage on the first electrode in volts*/
v2=0 ;   /* voltage on the second electrode in volts */
         /* vtip[] is offset voltage on the tip in volts to mini force*/
/* region where the cantilever is over electrode  #1 */
for (x = w ; x < L ; x++){
vtip[c]=v1 ;
pos[c]= x-w ;
c++ ;
}
/* region where the cantilever is over electrode #1 and the trench */
for (x=L ; x <= (L+l) ; x++){
        vtip[c]=v1 ;
        pos[c]= x-w ;
        c++ ;
}
/* region where the cantilever is between electrode #1 and #2 */
for (x=L+l ; x < L+l+a ; x++){
if (x > (L+a))
A1= 0 ;
else A1= a-(l+(x-(l+L))) ;
A2 = (x-(L+l)) ;
vtip[c] = (A1*v1+A2*v2)/(A1+A2) ;
```

```
pos[c]= x-w ;
c++ ;
}
/* region where the cantilever is over electrode #2 */
for (x= L+l+a; x<=(2*L+l+w); x++){
vtip[c] = v2 ;
     pos[c]= x-w ;
c++ ;
}
printf("L %f\n", L) ;
printf("l %f\n", l) ;
printf("a %f\n", a) ;
printf("b %f\n", b) ;
printf("w %f\n", w) ;
printf("\npos[] vtip[]\n") ;
for( i=0 ; i <= c ; i++)
printf("%.3f %.3f\n",pos[i] , vtip[i]) ;
}
```

Appendix F: EFM GPIB Code

GPIB C code used to measure the ω_1 component of the force as a function of tip voltage. Code controls the EG&G 7280 lock-in amplifier.

```
/* ***********************************
GPIB Code used to measure EFM as function of tip voltage.
Files decl.h and mcib.obj must be in same directory.
Connect Vtip to DAC on EG&G 7280.
Connect normal force to ch A on EG&G 7280.
Use modified versions of plot.c and elockin6.c
and efilecon.c that were used for ac7280.c.
Code written by Steve Howell
*********************************** */
#include <stdio.h>
#include <string.h>
#include <stdlib.h>
#include <dos.h>
#include <ctype.h>
#include <conio.h>
#include <math.h>
#include "elockin6.h"
#include "efilecon.h"
#include "eplot.h"
#define MAXPTS 512
#define MINPTS 50
#define FREQ 250000
#define AMP 2000
#define MAXV 1000
#define MINV -1000
#define SAMPLE 1
#define CURVES 1
#define POINTS 150
#define PRINTOUT 1
#define DEADTIME 5000

#define DEBUG 0

void main(void){
char filename[7]="junk",tfilename[7], ftemp[10],oldfilename[7]  ;
char ans1[1], ans2[1],ans3[1] ;
double freq=FREQ ;
double amp=AMP ;
double volts[600], mag[600], smag[600], tmag ;
double dv, vtip ;
double maxv=MAXV, minv=MINV, points, sample=SAMPLE , s ;
double curves=CURVES , c ;
double loop = 0 ;
int t, n, save=0,  p, pts=POINTS  ;

enable_graph() ;
delay(1000) ;
enable_lockin() ;
delay(10000);
do{
  tmag = 0 ;
  save = 0 ;
  clearscreen() ;
  do{
   printf("Change scan parameters? (y/n): ") ;
   scanf("%s",ans1) ;
```

```
   } while(ans1[0] != 'y' && ans1[0] != 'Y' &&
                ans1[0] != 'N' && ans1[0] != 'n') ;
if  (ans1[0]=='y' || ans1[0] =='Y'){
  printf("Current file name: %s \n",filename) ;
  do{
    printf("Enter file name (6 chars max) : ") ;
    scanf("%s", filename) ;
  } while(strlen(filename) > 6) ;
printf("cuurent file number: %.0lf \n", loop) ;
printf("Enter the file number: ");
scanf("%lf",&loop) ;
/* printf("Enter EFM frequency (Hz) : ") ;
scanf("%lf",&freq) ;
if (freq > 250000)
  freq = 250000 ;
printf("Enter EFM amplitude (mV): ") ;
scanf("%lf",&amp) ; */
printf("Enter the maximum voltage (mV): ") ;
scanf("%lf", &maxv) ;
printf("Enter the minimum voltage (mV): ") ;
scanf("%lf", &minv) ;
printf("Enter the number of points: ") ;
scanf("%d", &pts) ;
if (pts > MAXPTS)
  pts = MAXPTS ;
printf("Enter the sample number: ") ;
scanf("%lf", &sample) ;
printf("Enter the number of curves: ") ;
scanf("%lf", &curves) ;
}
for(p=0 ; p<= pts ; p++){
volts[p] =0.0 ;
mag[p] =0.0 ;
}
points = 0 ;
for(p=0;p<=pts;p++)
points++ ;
dv=floor(((maxv-minv)/(points-1))) ;
        clearscreen() ;
if (PRINTOUT){
printf("\n\n\nfilename=%s\n",filename) ;
printf("File number= %.0lf\n", loop) ;
/*printf("freq= %.2lf \n",freq) ;
printf("amp=%.2lf\n",amp) ; */
printf("maxv=%.2lf\n",maxv) ;
printf("minv=%.2lf\n",minv) ;
printf("pts= %d\n",pts);
printf("sample=%.0lf\n",sample) ;
printf("curves=%.0lf\n",curves) ;
printf("dv =%.2lf\n\n\n",dv) ;
}
/* set_freq(freq) ;
```

```
setamp(amp) ; */
vtip = minv ;
setdac(vtip) ;
for (p=0 ; p<=pts ; p++){
volts[p] = vtip ;
vtip = vtip + dv ;
}
for (c=1 ; c<=(curves) ; c++){
vtip = minv ;
for( p =0 ; p <= pts ; p++)
smag[p] = 0.0 ;
for( p= 0 ; p <= pts ; p++){
tmag = 0.0 ;
setdac(vtip) ;
for( s=1 ; s<= (sample) ; s++)
 tmag=tmag+read_mag1() ;
smag[p]=tmag/(sample) ;
vtip = vtip + dv ;
}
for (p=0 ; p<=pts ; p++)
mag[p] = mag[p] + smag[p] ;
delay(DEADTIME) ;
plot(volts,mag,pts,"Volts","EFM") ;
printf("loop: %.0lf \n", c) ;
}
setdac(0) ;
clearscreen() ;
plot(volts,mag,pts,"Volts","EFM") ;
for (p=0 ; p<=pts ; p++)
mag[p] = mag[p]/(curves) ;
        if (DEBUG)
for (p=0 ; p<= pts ; p++)
printf("%d,%.2lf,%.2lf\n", p, volts[p], mag[p]) ;
do{
printf("Save data? (y/n): ") ;
scanf("%s",ans2) ;
} while(ans2[0] != 'y' && ans2[0] != 'Y' &&
                  ans2[0] != 'N' && ans2[0] != 'n') ;
if  ((ans2[0]=='y' || ans2[0] =='Y') && (loop < 99)){
save_data(filename,".efm",loop,volts,mag,pts,
                          "volts","mag",10) ;
loop++ ;
}

printf("\n\nAnother scan? ") ;
scanf("%s",ans3) ;
 } while(ans3[0] == 'y' || ans3[0] == 'Y') ;
disable_graph() ;
disable_lockin() ;
exit(0) ;
}
```

Appendix G: Additional Molecules Probed by EFM

1) Purple Membrane (large patch): 350 ± 50 mV

2) 4-Pyridinethiol (4-PYSH) C_4H_5NS: 30 ± 50 mV

4-PYSH+Teraphenylporphrinatocobalt(CoTPP): 130 ±50 mV

3)

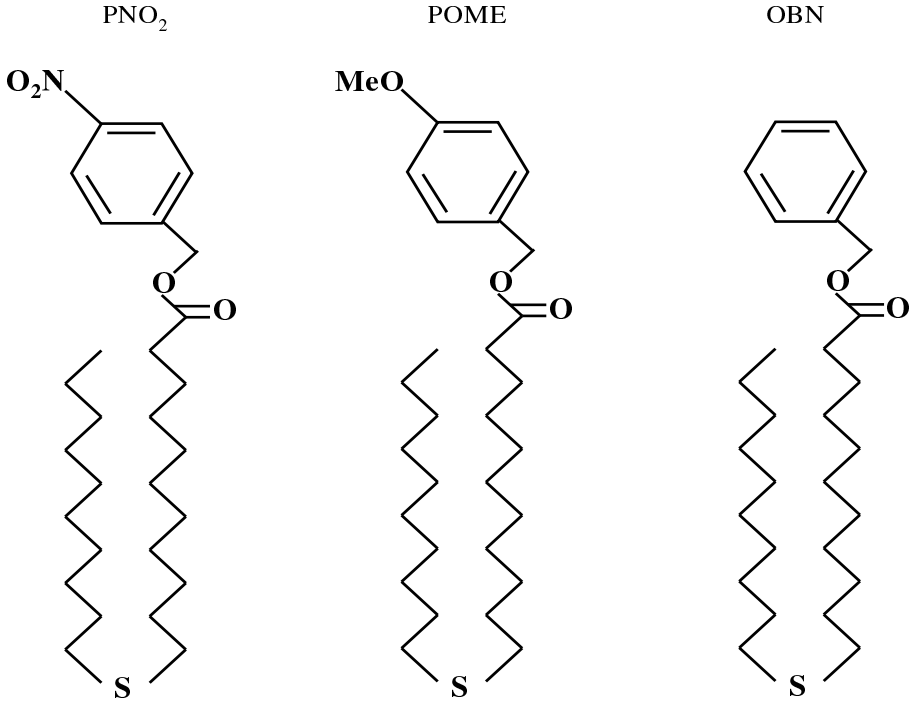

-180 ±50 mV -100 ±50 mV -20 ±50 mV

Figure G.1. Additional studies on different classes of molecules probed with the EFM. All measurements are reported with respect to bare gold. Purple Membrane samples were prepared by Scott Crittenden from the Dept. of Physics, Purdue University, USA. PNO_2, POME and OBN samples were synthesized and prepare by Elwyn Shelley from the Haworth School Of Chemistry, University of Biringham, UK.

VITA

VITA

Stephen Wayne Howell was born on December 3, 1971 in Goshen, Indiana, the son of Bill and Lillian Howell. He was raised in Middlebury, Indiana. During the fall of 1990, he began his freshman year at Indiana University in Bloomington, Indiana. During the spring of 1994, he enlisted in the United States Marine Corps. In the fall of 1994, he joined the Data Communication Platoon, DET COMMCO, HQBN, 4THMARDIV, INDIANAPOLIS, IN. He received a B.S. in Astronomy and Astrophysics from Indiana University in the spring of 1995. In the fall of 1995, he entered the physics program at Purdue University. He completed his enlistment in the Marine Corps as Platoon Sergeant in May of 2000. While at Purdue, he married the love of his life Laura (Richwine) Howell.